

Department of Physics and Astronomy

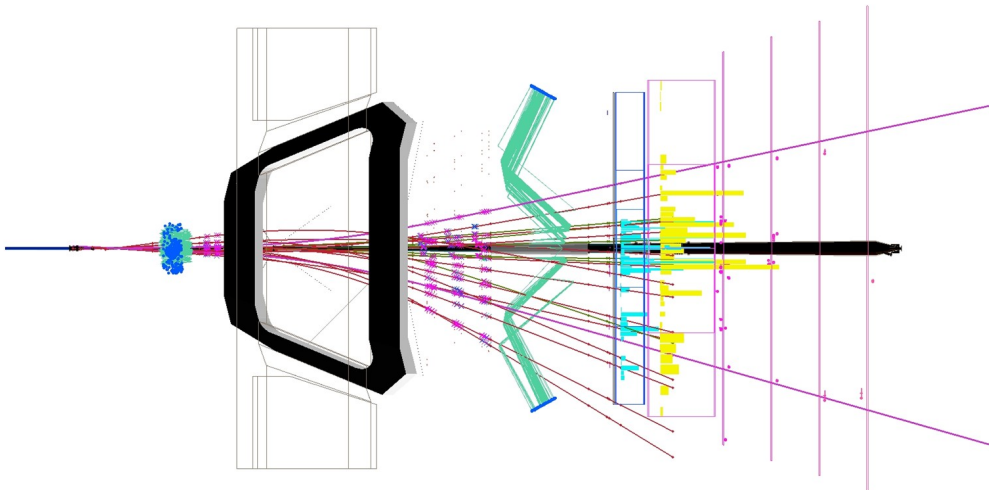
Heidelberg University

Diploma thesis
in Physics

submitted by
Paul Seyfert
born in Frankfurt am Main

November 2010

Measurement of Track Reconstruction Efficiencies at the LHCb Experiment



*This diploma thesis has been carried out by
Paul Seyfert
at the
Physical Institute
under the supervision of
Prof. Dr. Ulrich Uwer*

The title page shows the LHCb event display of event 52915 from run 69236.

*Dedicated to Tina
whose patience throughout
the work on this thesis
has been unending*

Abstract

Since end of 2009 the LHC, the world's largest and highest energy particle accelerator, operates. LHCb, one of the experiments at the LHC, aims to analyse B meson decays. To reconstruct these decays, trajectories of charged particles need to be reconstructed. An important property of the track reconstruction is its efficiency which needs to be known for numerous measurements.

In two implementations of the "tag and probe method" the decays $K_S \rightarrow \pi\pi$ and $J/\psi \rightarrow \mu\mu$ are reconstructed to measure the tracking efficiency. In both implementations one of the decay products is found independent of the T station trackers.

For K_S decays the measured efficiency of $\varepsilon = 95.5 \pm 0.3 \%$ is 0.7 % below the simulated efficiency. The implementation for J/ψ decays has been integrated into the analysis software framework of LHCb to provide results after the next reprocessing of the recorded events.

With K_S decays the phase space up to $p_T \approx 800$ MeV is investigated. In combination with J/ψ decays most of the acceptance of LHCb will be covered.

Kurzfassung

Seit Ende 2009 ist der LHC, der bisher größte und energiereichste Teilchenbeschleuniger in Betrieb. LHCb, eines der Experimente am LHC, hat die Untersuchung von B Meson Zerfällen zum Ziel. Zur Rekonstruktion dieser Zerfälle müssen Spuren geladener Teilchen rekonstruiert werden. Eine wichtige Eigenschaft der Spurrekonstruktion ist deren Effizienz, welche für zahlreiche Messungen bekannt sein muss.

In zwei Implementierungen der „tag and probe“ Methode werden die Zerfälle $K_S \rightarrow \pi\pi$ und $J/\psi \rightarrow \mu\mu$ rekonstruiert um die Spurrekonstruktionseffizienz zu messen. In beiden Varianten wird eines der Zerfallsprodukte unabhängig von den T Station Detektoren rekonstruiert.

Mit den K_S Zerfällen wurde eine Effizienz von $\varepsilon = 95.5 \pm 0.3 \%$ gemessen, was 0.7 % unter der Simulation liegt. Die Implementierung für J/ψ Zerfälle wurde in die Analyse Software von LHCb integriert, so dass Ergebnisse nach dem nächsten Reprozessieren der genommenen Daten zur Verfügung stehen werden.

Mit K_S Zerfällen wird die Spurrekonstruktionseffizienz für Teilchen mit bis zu $p_T \approx 800$ MeV gemessen. In Kombination mit der Messung an J/ψ Zerfällen wird nahezu die gesamte Akzeptanz von LHCb abgedeckt.

Contents

Contents	v
Introduction	vii
1 Theoretical Background	1
1.1 The Standard Model of Particle Physics	1
1.2 Meson Oscillation and CP Violation	4
2 The LHCb Experiment at the LHC	9
2.1 The Large Hadron Collider	9
2.2 Physics Programme of LHCb	10
2.3 General Layout	11
2.4 Tracking Subdetectors	12
2.5 Particle Identification Subdetectors	16
2.6 Trigger System	18
2.7 Computing	19
3 Track Reconstruction at LHCb	21
3.1 Track Reconstruction in General	21
3.2 Track Types and Tracking Algorithms at LHCb	22
4 The Tag and Probe Method	27
4.1 Sketch of the Tag and Probe Method	28
4.2 Tracking Efficiencies from the Simulation	28
4.3 Application of the Tag and Probe Method in LHCb	28
5 Probes for the Tracking System from the Calorimeters	31
5.1 Principle of Reconstructing Velo-Calo Probes	31
5.2 Detailed Explanation	32
5.3 Further Development of Velo-Calo Matching	34
5.4 Velo-Calo Probe Confirmation	40
6 Probes for the Tracking System from the Muon Stations	43
6.1 Track Reconstruction in the Muon Stations	43
6.2 Velo-Muon Matching in Principle	48
6.3 Further Improvements in Velo-Muon Tracking	48

7 Measurement of the Tracking Efficiency in the T Stations with $K_S \rightarrow \pi^+\pi^-$	55
7.1 Selection of K_S Events	55
7.2 Phase Space Coverage	58
7.3 Measured Efficiencies	61
7.4 Background from Wrong Confirmations	72
7.5 Effect of the Background Reduction in Velo-Calo Matching	76
8 Measurement of the Trigger Efficiency of the Muon Track Segment Reconstruction with $J/\psi \rightarrow \mu^+\mu^-$	79
8.1 Definition of the Trigger Efficiency	80
8.2 Event Selection	81
8.3 Trigger Efficiency Determination	81
9 Measurement of the Tracking Efficiency in the T Stations with $J/\psi \rightarrow \mu^+\mu^-$	85
9.1 Current Stripping Status	85
9.2 Selection of J/ψ Events	86
9.3 First Results	86
9.4 Developed Stripping Line	87
9.5 Phase Space Coverage	88
10 Error Discussion	91
10.1 Error Estimation for Certain Processes	91
10.2 Error Estimation in the Tag and Probe Method	92
10.3 Consequences for Velo-Calo Probes	94
11 Conclusion and Outlook	95
A Derivations	99
A.1 Muon Track Fit	99
A.2 Optimising the z Value of Velo-Muon Matching in y	100
B Tables and Figures	103
B.1 Muon Track Reconstruction Efficiencies	103
B.2 Configuration of the Velo-Muon matching algorithm	104
B.3 K_S Selection	107
C Toy Simulation to Validate the Efficiency Estimation and the According Error Estimate	111
C.1 Description of the Toy Study	111
C.2 Results of the Toy Study	112
D Data Sets	115
D.1 Simulated Data	115
D.2 Data	116
Bibliography	119
Index	123

Introduction

Physicists try to establish a theory that comprises the laws that govern our universe. Theories are models inspired by and explaining observations. Models not only make statements about past observations but also predict future observations, they are rejected if they make wrong predictions or improved by new findings.

The Standard Model of particle physics is the state of the art description of the fundamental building blocks of matter and their interactions. However, the standard model is known to have shortcomings. There are observed effects unexplained and predicted particles unobserved. This inconvenience is treated on the one hand by developing new theories and on the other hand by performing sophisticated experiments to probe the unexplored parts of physics.

At the Large Hadron Collider beauty Experiment (LHCb) so-called beautiful mesons (B mesons) are observed to measure CP violation. CP violation – the effect that anti-matter in a mirrored universe behaves different from matter in our universe – is assumed to be one of the conditions to provide the observed surplus of matter in the universe. However the standard model prediction of CP violation is precise but cannot explain the amount of matter in the universe. LHCb aims to measure if effects beyond the description of the standard model (“New Physics”) have an impact on the CP violation in B decays.

To reach this ambitious aim, good knowledge of the detector and of the capabilities of the reconstruction algorithms is needed. For the studies to be performed at LHCb not only accurate determination of track parameters and a high efficiency to find tracks are important but also the precise knowledge of the latter efficiency. The uncertainty of the reconstruction efficiency has been one of the major contributions the first cross section measurement at LHCb.

This thesis deals with a measurement of the efficiency to reconstruct a particle in the tracking system of the experiment. Algorithms to find trajectories of charged particles which are independent of the tracking system have been implemented. These are presented in chapters 5 and 6

The signatures found by these algorithms are then combined with tracks from the standard reconstruction to reconstruct two body decays in chapters 7 and 9. The method of combining full reconstructed tracks with independent signatures is called “tag and probe method”. It is explained in chapter 4.

Developing one of the algorithms a shortcoming of a track segment reconstruction in the high level trigger could be identified. The measurement leading to improvement of the efficiency by five percent is presented in chapter 8.

Theoretical Background

Atomlaser . . . man koppelt das
Bose-Einstein Kondensat dann
ans Gravitationsfeld . . . **Man
lässt es fallen!**

Arno Trautmann

Before turning to the actual experiment and the analysis performed, a brief introduction to particle physics shall be given. Following a common convention, the speed of light c and Planck's constant \hbar are set to 1.

1.1 The Standard Model of Particle Physics

Particle content of the Standard Model

All particles currently known and their interactions are described by the Standard Model of particle physics.

The fundamental particles which make up matter are all fermions, i.e. particles of half-integer spin, while those mediating forces are bosons, particles of integer spin. The bosons of the strong interaction are called gluons, the boson of the electromagnetic interaction is the photon, and Z and W bosons are the weak interaction's mediators. Whenever a particle takes part in an interaction it is said to couple to the corresponding boson.

All fundamental particles and their properties are listed in figure 1.1. Twelve fundamental fermions set up two subsets of six particles each, namely quarks and leptons. The latter are the three charged leptons, electron (e), muon (μ), and tau (τ), and their corresponding chargeless neutrinos (ν_e, ν_μ, ν_τ). In the quark sector there are three quarks (*down type quarks*) of charge $-1/3 e$ while the other three (*up type*) carry charge $2/3 e$. The property of being an up, down, charm, strange, top, or bottom quark is called *flavour*.

Both, quarks and leptons carry a weak charge and both are arranged in doublets as the weak interaction converts them into each other. The names reflect the correspondence. Quarks carry a strong charge additionally to their weak and electromagnetic charge.

Unlike leptons, quarks cannot exist as free particles. They are *confined* to bound states either as quark-antiquark pairs (*mesons*) or as three quark states (*baryons*). The underlying principle is that free particles must be of neutral colour charge. Although

Three Generations
of Matter (Fermions)

	I	II	III	
mass→	2.4 MeV	1.27 GeV	171.2 GeV	0
charge→	$\frac{2}{3}$	$\frac{2}{3}$	$\frac{2}{3}$	0
spin→	$\frac{1}{2}$	$\frac{1}{2}$	$\frac{1}{2}$	1
name→	u up	c charm	t top	γ photon
Quarks	4.8 MeV $-\frac{1}{3}$ $\frac{1}{2}$ d down	104 MeV $-\frac{1}{3}$ $\frac{1}{2}$ s strange	4.2 GeV $-\frac{1}{3}$ $\frac{1}{2}$ b bottom	0 0 1 g gluon
	<2.2 eV 0 $\frac{1}{2}$ ν_e electron neutrino	<0.17 MeV 0 $\frac{1}{2}$ ν_μ muon neutrino	<15.5 MeV 0 $\frac{1}{2}$ ν_τ tau neutrino	91.2 GeV 0 1 Z weak force
	0.511 MeV -1 $\frac{1}{2}$ e electron	105.7 MeV -1 $\frac{1}{2}$ μ muon	1.777 GeV -1 $\frac{1}{2}$ τ tau	80.4 GeV ± 1 1 W weak force
Leptons				Bosons (Forces)

Figure 1.1: Particle content of the Standard Model of particle physics. [Wik10]

this level of considering hadrons¹ is sufficient for the content of this work it must be mentioned that this is highly simplified – the strongly bound systems are far more complicated systems involving several additional quarks, antiquarks and gluons with vanishing flavour, charge and spin².

The CKM Mechanism

There is a number of quantities in physics which are supposed to be conserved in all interactions, energy among them. Other quantities are only conserved for certain interactions like the total flavour of a system. Flavour is conserved in strong or electromagnetic processes but can change in weak processes.

The weak interaction mediates between weak eigenstates which do not coincide with mass eigenstates in the quark sector. The transformation between weak eigenstates and mass eigenstates is parametrised by the unitary Cabibbo-Kobayashi-Maskawa (CKM) matrix. [KM73]

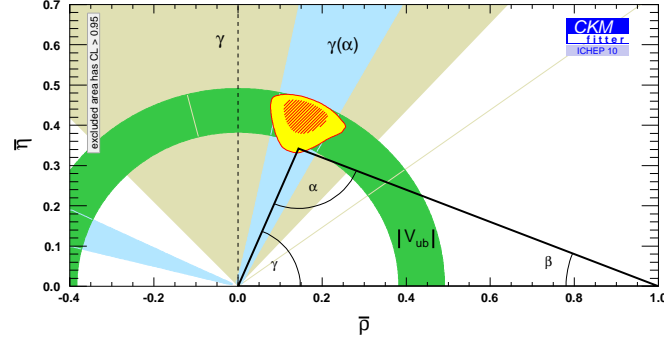
$$\begin{pmatrix} d \\ s \\ b \end{pmatrix}_{\text{weak}} = \begin{pmatrix} V_{ud} & V_{us} & V_{ub} \\ V_{cd} & V_{cs} & V_{cb} \\ V_{td} & V_{ts} & V_{tb} \end{pmatrix} \begin{pmatrix} d \\ s \\ b \end{pmatrix}_{\text{mass}}$$

The CKM matrix only transforms down type quarks as one of the sectors (up type or down type) can be parametrised such that weak eigenstates and mass eigenstates coincide. The number of degrees of freedoms of a unitary 3×3 matrix³ is nine but five

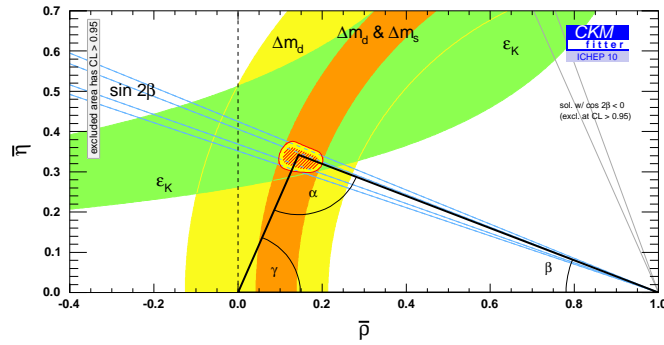
¹Hadron is the generic term for strongly interacting particle.

²This is subject to Hadron Physics and explained in the literature.

³In general a complex 3×3 matrix has eighteen degrees of freedom, the unitarity condition reduces them.



(a) From measurements involving tree level processes.



(b) From measurements involving loops at leading order.

 Figure 1.2: The knowledge from 2010 of the unitarity triangle. [C⁺05]

of them can be absorbed by gauge phases of the quark fields. The remaining physical parameters are three angles and a complex phase which is the only reason for CP violation in the Standard Model.

The unitary condition can be expressed in a number of scalar equations. One of them

$$V_{ud}V_{ub}^* + V_{cd}V_{cb}^* + V_{td}V_{tb}^* = 0$$

is commonly illustrated in the complex plane. The three complex summands form a triangle in the complex plane, normalising it by dividing through $V_{cd}V_{cb}^*$ fixes one point to 1 while another corner is fixed to 0. Only the third corner has to be determined in the experiment as shown in figure 1.2.

There are six of those unitarity triangles, the one from

$$V_{us}V_{ub}^* + V_{cs}V_{cb}^* + V_{ts}V_{tb}^* = 0$$

is called “b-s unitarity triangle” and is examined e.g. in the decay $B_s^0 \rightarrow J/\psi\phi$ at LHCb.

1.2 Meson Oscillation and CP Violation

Freely propagating (i.e. being produced and developing according to their equation of motion) particles are mass eigenstates. Their production however is a matter of strong interaction and their decay is a weak process. In several neutral meson systems, mass eigenstates and flavour eigenstates do not coincide which is an effect of the aforementioned property that weak *quark* eigenstates are different from *quark* mass eigenstates. The time development according to mass eigenstates leads to an oscillation of flavour eigenstates in time.

CP is the combined symmetry transformation which turns particles into their antiparticles (C for charge inversion) and inverts all spatial coordinates (P for parity transformation). If CP eigenstates and mass eigenstates do not coincide either, a CP even state may oscillate into a CP odd state and vice versa. In this case the CP eigenvalue of a system is not conserved over time, CP is said to be violated in mixing.

Both, meson oscillation and CP violation, have been observed and are explained here in the B_s^0 system. B_s^0 system here is the short term for the two state system of B_s^0 and \bar{B}_s^0 , which are bound $\bar{b}s$ and $b\bar{s}$ states respectively. Let B_{sL}^0 be the mass eigenstate with the smaller mass eigenvalue (L for *light*) and B_{sH}^0 the mass eigenstate with the larger eigenvalue respectively (H for *heavy*). The mass eigenstates can then be written as linear combinations of the flavour eigenstates

$$\begin{aligned} |B_{sL}^0\rangle &= p |B_s^0\rangle + q |\bar{B}_s^0\rangle \\ |B_{sH}^0\rangle &= p |B_s^0\rangle - q |\bar{B}_s^0\rangle \end{aligned} \quad (1.1)$$

with the normalisation $|p|^2 + |q|^2 = 1$. The phenomenological Schrödinger equation

$$i \frac{d}{dt} \begin{pmatrix} |B_s^0\rangle \\ |\bar{B}_s^0\rangle \end{pmatrix} = \begin{pmatrix} M_{11} - i/2\Gamma_{11} & M_{12} - i/2\Gamma_{12} \\ M_{21} - i/2\Gamma_{21} & M_{22} - i/2\Gamma_{22} \end{pmatrix} \begin{pmatrix} |B_s^0\rangle \\ |\bar{B}_s^0\rangle \end{pmatrix} \quad (1.2)$$

describes the development in time and can easily be solved for mass eigenstates.

$$\begin{aligned} i \frac{d}{dt} \begin{pmatrix} |B_{sL}^0\rangle \\ |B_{sH}^0\rangle \end{pmatrix} &= \begin{pmatrix} M_L - i/2\Gamma_L & 0 \\ 0 & M_H - i/2\Gamma_H \end{pmatrix} \begin{pmatrix} |B_{sL}^0\rangle \\ |B_{sH}^0\rangle \end{pmatrix} \\ |B_{sL}^0(t)\rangle &= \exp(-iM_L t - 1/2\Gamma_L t) |B_{sL}^0(t=0)\rangle \\ |B_{sH}^0(t)\rangle &= \exp(-iM_H t - 1/2\Gamma_H t) |B_{sH}^0(t=0)\rangle \end{aligned} \quad (1.3)$$

The development in time of flavour eigenstates however is of interest, which is obtained using the inverse change of basis.

$$\begin{aligned} |B_s^0\rangle &= \frac{1}{2p} |B_{sL}^0\rangle + \frac{1}{2p} |B_{sH}^0\rangle \\ |\bar{B}_s^0\rangle &= \frac{1}{2q} |B_{sL}^0\rangle - \frac{1}{2q} |B_{sH}^0\rangle \end{aligned}$$

With equation 1.3 the development of B_s^0 is then given by the following formula. For

clarity, only formulae for B_s^0 are written out.

$$\begin{aligned} |B_s^0(t)\rangle &= \frac{1}{2p} \exp(-iM_L t - 1/2\Gamma_L t) |B_{sL}^0(0)\rangle \\ &+ \frac{1}{2p} \exp(-iM_H t - 1/2\Gamma_H t) |B_{sH}^0(0)\rangle \end{aligned}$$

With equation 1.1 the time propagation of the flavour eigenstates is expressed in terms of the pure flavour eigenstates at $t = 0$.

$$\begin{aligned} |B_s^0(t)\rangle &= +\frac{1}{2p} \exp(-iM_L t - 1/2\Gamma_L t) \left[p |B_s^0(0)\rangle + q |\bar{B}_s^0(0)\rangle \right] \\ &+ \frac{1}{2p} \exp(-iM_H t - 1/2\Gamma_H t) \left[p |B_s^0(0)\rangle - q |\bar{B}_s^0(0)\rangle \right] \\ |B_s^0(t)\rangle &= \left(\frac{1}{2} \exp(-iM_L t - 1/2\Gamma_L t) + \frac{1}{2} \exp(-iM_H t - 1/2\Gamma_H t) \right) |B_s^0(0)\rangle \\ &+ \frac{q}{p} \left(\frac{1}{2} \exp(-iM_L t - 1/2\Gamma_L t) - \frac{1}{2} \exp(-iM_H t - 1/2\Gamma_H t) \right) |\bar{B}_s^0(0)\rangle \end{aligned}$$

The oscillation of a B_s^0 into a \bar{B}_s^0 can then be calculated as the product

$$\begin{aligned} |\langle \bar{B}_s^0(0) | B_s^0(t) \rangle|^2 &= \frac{1}{4} \left| \frac{q}{p} \right|^2 \left[\exp(-\Gamma_L t) + \exp(-\Gamma_H t) \right. \\ &\quad - \exp(-iM_L t - 1/2\Gamma_L t + iM_H t - 1/2\Gamma_H t) \\ &\quad \left. - \exp(+iM_L t - 1/2\Gamma_L t - iM_H t - 1/2\Gamma_H t) \right] \\ &= \frac{1}{4} \left| \frac{q}{p} \right|^2 \left[e^{-\Gamma_L t} + e^{-\Gamma_H t} \right. \\ &\quad \left. - e^{-\frac{\Gamma_L + \Gamma_H}{2} t} \underbrace{\left(e^{iM_H t - iM_L t} + e^{-iM_H t + iM_L t} \right)}_{2 \cos(M_H - M_L)t} \right] \end{aligned}$$

which contains the oscillating term $\cos(M_H - M_L)t$. The reverse process $\bar{B}_s^0 \rightarrow B_s^0$, which is the CP conjugate, has a slightly different structure.

$$\begin{aligned} |\langle B_s^0(0) | \bar{B}_s^0(t) \rangle|^2 &= \frac{1}{4} \left| \frac{p}{q} \right|^2 \left[e^{-\Gamma_L t} + e^{-\Gamma_H t} - 2e^{-\frac{\Gamma_L + \Gamma_H}{2} t} \cos(M_H - M_L)t \right] \\ &= \left| \frac{p}{q} \right|^4 |\langle \bar{B}_s^0(0) | B_s^0(t) \rangle|^2 \end{aligned}$$

CP violation in B mixing can occur if $|q/p| \neq 1$. This ratio can be expressed in terms of the Hamilton operator in equation 1.2 in the flavour representation.

$$\frac{q}{p} = -\frac{2M_{12}^* - i\Gamma_{12}^*}{M_H - M_L + i/2(\Gamma_H - \Gamma_L)}$$

1. THEORETICAL BACKGROUND

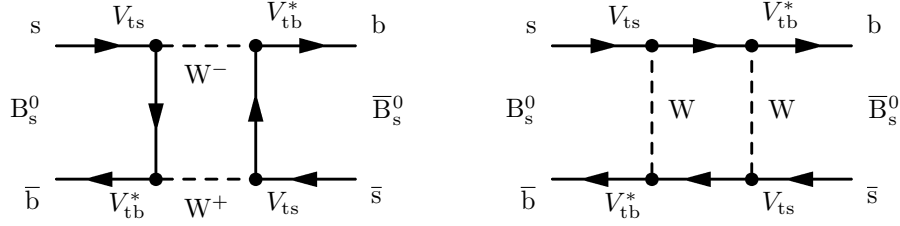


Figure 1.3: Lowest order Feynman diagrams for the transition of a B_s^0 meson into a \bar{B}_s^0 .

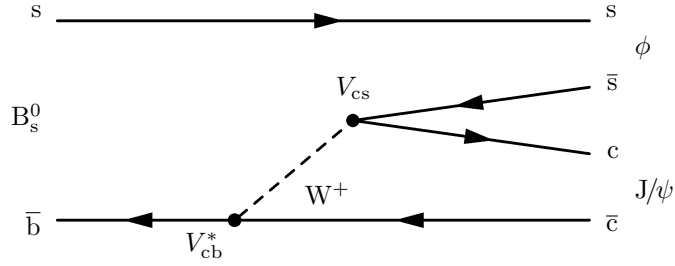


Figure 1.4: The Feynman diagram of the leading order contribution to the decay $B_s^0 \rightarrow J/\psi\phi$.

At lowest order these terms in the Hamilton operator are given by the box diagrams in figure 1.3. Up to a phase convention the ratio is

$$\frac{q}{p} = \exp(-i\Phi_M) = \exp(-2i \arg(V_{ts} V_{tb}^*)).$$

In the decay $B_s^0 \rightarrow J/\psi\phi$ however another phase enters – at lowest order a \bar{b} quark is converted into a \bar{c} quark and a $c\bar{s}$ quark pair is produced as to be seen in figure 1.4. The ratio of the decay amplitudes

$$\frac{A_f}{A_{\bar{f}}} := \frac{A_{B_s^0 \rightarrow J/\psi\phi}}{A_{\bar{B}_s^0 \rightarrow J/\psi\phi}}$$

then contains another phase which is also given by the CKM matrix.

$$\frac{A_f}{A_{\bar{f}}} = \exp(2i\Phi_D) = \arg(V_{cs} V_{cb}^*)$$

The total CP -violating phase $\Phi_S = \Phi_M - 2\Phi_D$ is then minus twice the CKM angle β_s .

$$\begin{aligned} \Phi_S &= 2 \arg(V_{ts} V_{tb}^*) - 2 \arg(V_{cs} V_{cb}^*) \\ &= -2 \arg\left(-\frac{V_{ts} V_{tb}^*}{V_{cs} V_{cb}^*}\right) \\ &=: -2\beta_s \end{aligned}$$

Drawbacks of the Standard Model

Major drawbacks of the Standard Model are that it is neither including gravity nor allowing neutrino masses and that the predicted CP violation cannot explain the surplus of matter over antimatter in the universe. The former phenomenon, gravity, is known for many centuries whereas the oscillation $\nu_\mu \rightarrow \nu_\tau$ was discovered this year⁴. No neutrino mass is known up to now while the observed neutrino oscillation – the effect that neutrinos decay with another flavour than they are produced with – can only be explained by mass eigenstates different from the flavour eigenstates (similar to oscillation in the B sector).

Up to now, no introduction of neutrino masses to the Standard Model is generally accepted because these automatically introduce right handed neutrinos. These are unobserved up to now.

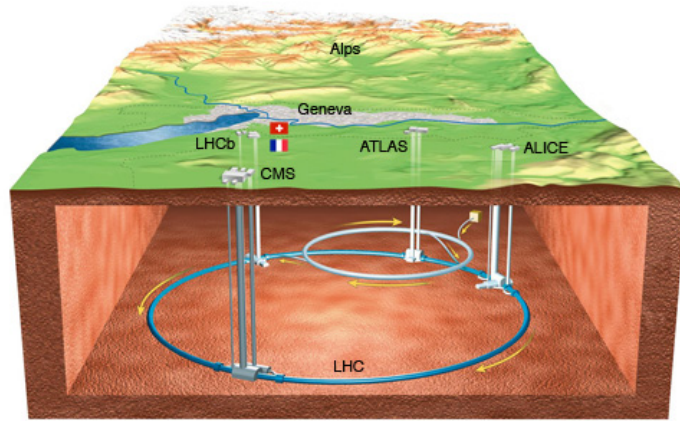
To introduce gravity to the Standard Model, extra dimensions only accessible for mediators of gravity have been proposed. These are as well unobserved.

The third of the above problems is a cosmological one. One assumes that in the beginning of our universe the same amounts of matter and antimatter have been produced. However nowadays this symmetry is broken – there is more matter left in the universe⁵. Sakharov proposed three conditions to be fulfilled to explain the discrepancy (see [Cli06]). One of them is violation of C and CP . Both are implemented in the Standard Model but the magnitude of CP violation from the electroweak sector is too small to explain the present excess of matter. An additional source of CP violation in the lepton sector has been proposed which is unobserved, too.

CP violation and a possible deviation from the Standard Model prediction, as well the influence of new particles to observable processes are investigated at the Large Hadron Collider beauty experiment which shall be introduced in the following chapter.

⁴The first direct observation has been published at 8 June 2010. [A⁺10b]

⁵For obvious reasons it is not the other way around: What is present in the universe has been called “matter” long before antimatter has been thought of. What is remarkable is that the amounts are not equal.



CERN Accelerator Complex

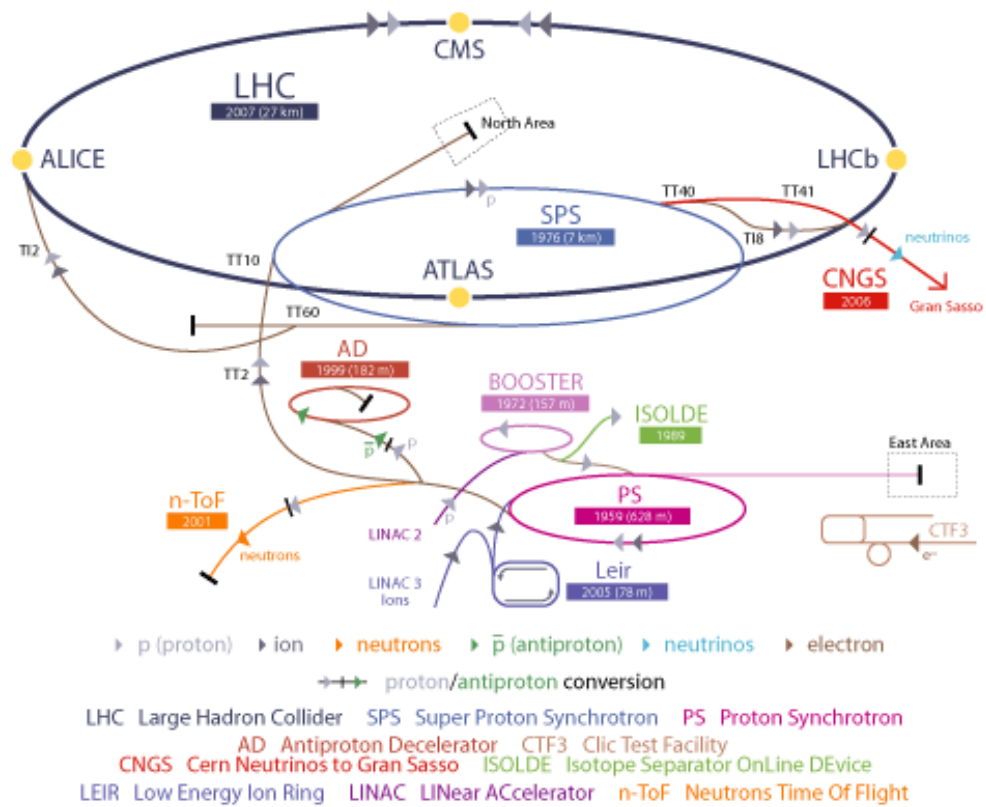


Figure 2.1: The LHC accelerator complex. [Col10a; CER10]

The LHCb Experiment at the LHC

Schönes Wochenende.
Bis morgen.

Iuri Bagaturia (11.06.2010)

The Large Hadron Collider beauty experiment (LHCb) is one of the experiments at the Large Hadron Collider (LHC) in Geneva. It is dedicated to the analysis of B mesons produced at high rates in the collisions of protons.

2.1 The Large Hadron Collider

The LHC is the main element of the world's highest energy particle accelerator complex operated at the European Organisation for Nuclear Research (CERN, Conseil Européen pour la Recherche Nucléaire). Protons as well as lead nuclei can be collided, the former at centre of mass energies from 900 GeV (injection energy) to 14 TeV¹, the latter at 5.5 TeV/nucleon.

Collisions of heavy ions serve to investigate the QCD phase diagram and especially quark-gluon plasma with the ALICE detector (A Large Ion Collider Experiment) while the discovery of the Higgs boson, supersymmetric particles and extra dimensions are goals of the ATLAS (A Toroidal LHC ApparatuS) and CMS (Compact Muon Solenoid) experiments. The measurement of CP -violation in the decay of B and D mesons is performed at LHCb. Particle production almost directly in line with the colliding protons is measured at LHCf (Large Hadron Collider forward), the precise measurement of the total proton-proton cross section as well as the in-depth study of the proton structure are done at TOTEM (TOTal cross section, Elastic scattering and diffraction dissociation Measurement at the LHC) and finally the search for magnetic monopoles, black hole remnants and directly detectable supersymmetric particles is performed with MoEDAL (Monopole and Exotics Detector at the LHC).

The B mesons to be investigated with LHCb are known to be produced rather at large pseudo rapidities as can be seen in figure 2.2. Therefore LHCb is a forward spectrometer. A single arm is enough as both quarks from the $b\bar{b}$ pairs fly into the same forward range rather than in opposite directions.

¹During the first years of operation the energies are limited to $\sqrt{s} = 7$ TeV.

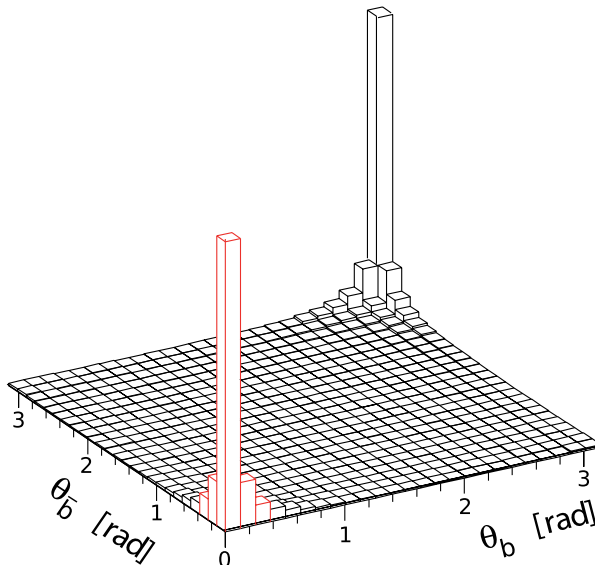


Figure 2.2: Angular correlation between a produced b quark and its antiparticle in simulated pair production. Red bars indicate the acceptance of the LHCb detector. [HVdB03]

2.2 Physics Programme of LHCb

The study of B mesons serves several reasons. One wants to determine some still uncertain parameters of the Standard Model more precisely, discover predicted but yet undiscovered processes, and discover new effects.

The determination of the angle γ of the Unitarity Triangle is dominated by indirect measurements. A direct determination will provide a complementary value and is considered to improve the knowledge of the Unitarity Triangle. Moreover a deviation between direct and the indirect value would indicate new physics. A precision of $1.9\text{-}2.7^\circ$ is expected with an integrated luminosity of 10 fb^{-1} .

The B_s^0 meson is predicted to decay into a pair of muons at a very small branching fraction $\mathcal{B}(B_s^0 \rightarrow \mu^+\mu^-) = (3.35 \pm 0.32) \times 10^{-9}$. Up to now only an upper limit could be measured directly which is still one order of magnitude above the predicted value². The large number of B_s^0 produced at the LHC will enable physicists to improve the limit or even measure the branching fraction. $B_s^0 \rightarrow \mu^+\mu^-$ is of interest as there are supersymmetric models predicting a branching fraction above 10^{-8} .

The CP violating phase in the decay $B_s^0 \rightarrow J/\psi\phi$ is predicted with small theoretical uncertainty to be $-2\beta_s$ from the “b-s unitarity triangle” where $\beta_s = \arg(-V_{ts}V_{tb}^*/V_{cs}V_{cb}^*)$. A measurement at LHCb could differ from the prediction if particles beyond the Standard Model contribute with a new phase to the $B_s^0\text{-}\bar{B}_s^0$ box diagram.

²The DØ collaboration set a limit of 5.1×10^{-8} . [A⁺10a]

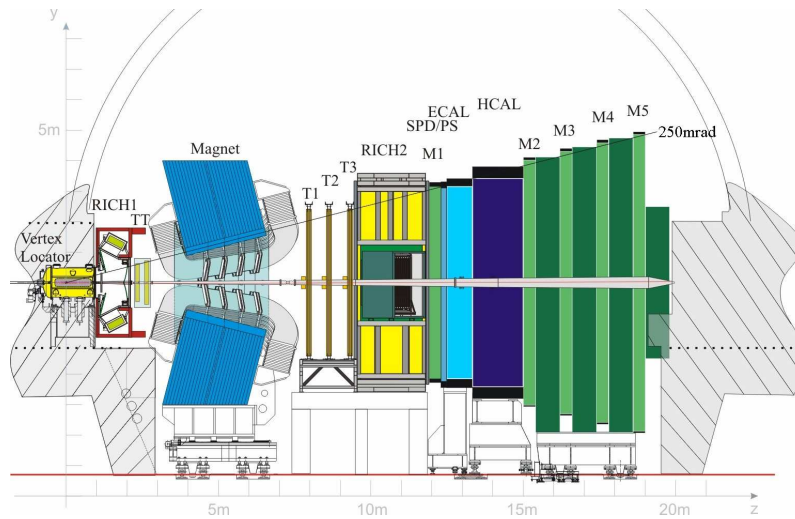


Figure 2.3: The LHCb detector comprising from left to right: the Vertex Locator, RICH1, TT, magnet, T station trackers, RICH2, first muon station M1, SPD, PRS, ECAL, HCAL, and the muon stations M2-M5. [Col08]

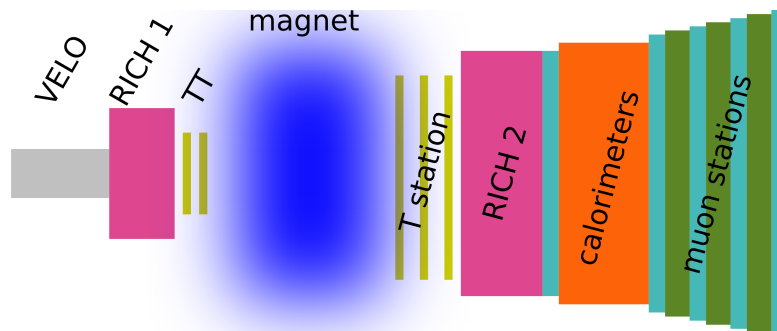


Figure 2.4: Reduced schematic of the LHCb detector seen from the top to illustrate the curvature of tracks in the magnetic field.

2.3 General Layout

In this introduction the subdetectors at LHCb are divided according to their purpose into tracking subdetectors and the particle identification system. Both detect particles directly or indirectly produced in the interaction of two protons once they are charged and do not decay before reaching the subdetectors. The calorimeters also detect neutral particles.

The layout of LHCb is shown in figure 2.3 and 2.4. The tracking system comprises the vertex locator (VELO) and the tracker turicensis (TT) to detect charged particles before entering the magnet while the T station trackers – the inner tracker (IT) and the outer tracker (OT) – detect the particles after passing the magnet. All tracking detectors serve for the reconstruction of particle trajectories (*tracks*).

The magnet is a dipole magnet with a vertical field. The field can be changed to

upward or downward polarity.

Identification of kaons and protons in the whole polar acceptance for low momentum tracks utilises the first ring imaging Cherenkov detector (RICH1) while high momentum particles at small polar angles are identified in RICH2. The calorimeter system comprising a scintillator pad detector (SPD), the preshower detector (PS), the electromagnetic calorimeter (ECAL), and the hadronic calorimeter (HCAL). It serves for the trigger as well as for particle identification and detection of neutral particles. The segmentation into four subcalorimeters allows the measurement of the longitudinal distribution of deposited energy. Muons are the only particles (except neutrinos) passing through the calorimeter and can be detected in the muon stations.

Detectors of both categories are designed to handle the high multiplicity at small polar angles. This is mainly done through finer granularity in case of the T station trackers, the calorimeters, and the muon stations. In case of the RICH2 it is done by increasing the distance to the interaction point with respect to RICH1, thus the distance between tracks is increased.

When speaking about positions and directions a reference frame is needed. In accelerator experiments it is common to choose the beam axis as z axis and the point where the interaction is supposed to take place as origin ($x = y = z = 0$). To have a right handed cartesian coordinate system, there is one choice left: the x axis is chosen to be in the horizontal plane such that the y axis points upwards. Slopes of tracks, i.e. dx/dz and dy/dz for the x - z plane and the y - z plane respectively are abbreviated with t_x and t_y .

Following general conventions, the azimuthal angle φ is zero on the positive x axis – going to the left, seen from the interaction point looking into the detector.

Due to the simple transformation under Lorentz boosts, the pseudo rapidity η is favoured over the polar angle ϑ . It is defined as

$$\eta = -\ln \left[\tan \left(\frac{\vartheta}{2} \right) \right].$$

2.4 Tracking Subdetectors

VELO

The dedication of LHCb to B physics also leads to other design aspects than the chosen rapidity range. The proposed studies also require a good resolution of the proper time between the production and the decay of a B meson. With the B mass m_B it can be computed using the flight distance d and the momentum p via

$$\Delta\tau = \frac{d \cdot m_B}{p}.$$

The latter is obtained from the track reconstruction, while the former requires a good spatial resolution of the position of the primary vertex as well as the position of the B decay vertex. The reconstruction of those vertices is done by extrapolating tracks in the VELO to a point where they meet. The uncertainty of such an extrapolation is governed by the uncertainty on the slopes of the initial tracks and by the distance of extrapolation. Whereas good track parameter resolution is a standard task to silicon detector development the reduction of the extrapolation distance lead to a unique design. The initial problem in the design of the VELO was to install it as close as possible to the colliding proton beams while neither beam may ever hit the detector.

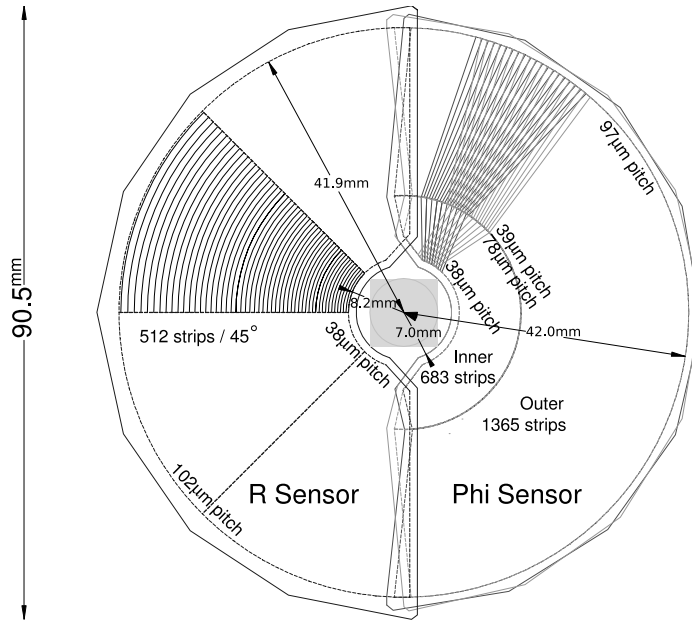


Figure 2.5: Schematic view of the VELO's r and φ sensors. [Col08]

At this point the limitations are not due to mechanics of the detector. Beam optics is not able to maintain a beam position within the dimensions needed for the desired vertex resolution over the whole acceleration range.

The remedy to these beam position uncertainties is a movable detector. The VELO consists of two halves each equipped with 23 silicon wafers which can be moved out of the nominal interaction region. After each acceleration, whenever the beam is considered to be stable, the VELO is moved to nominal position leaving a hole of 2×7 mm in diameter for the beam.

Once stable, charged particles are produced, they fly through the silicon wafers leaving a signal in each strip passed. The strips on the wafers are organised either radially measuring the azimuthal angle of a traversing particle (ϕ sensors) or at constant radii in eight polar sections and thus measuring the distance from the beam axis (r sensors). Each wafer has r sensors on one side and ϕ sensors on the other side – except for the two pile-up wafers having only r sensors. Combining measurements from both sensor types provides the desired three dimensional measurement. See figure 2.5 or [Col08] for further reference.

The hit resolution of the VELO is between 10 and 30 μm depending on the sensor's pitch at the hit. The azimuthal coverage of 182° creates overlap of the two detector halves to avoid a gap and to allow relative alignment.

Combining the momentum resolution of the spectrometer with the spacial resolution of the VELO the proper time resolution of B systems is supposed to be better than 40 fs.

Tracker Turicensis

The determination of the momentum of a charged particle requires measurements of the particle position on both sides of the magnetic field. Decay products of long lived

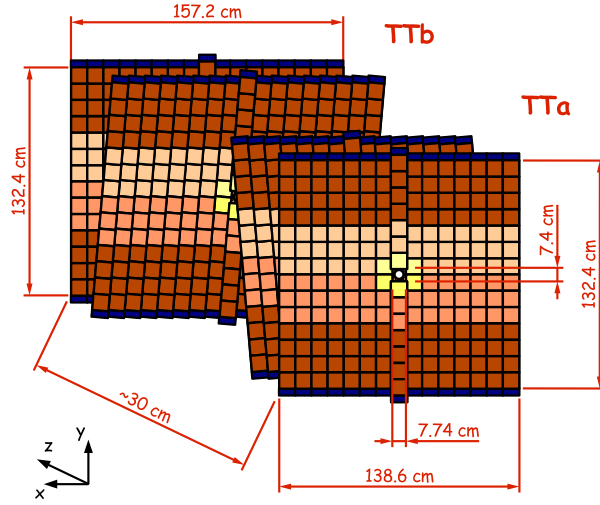


Figure 2.6: Schematic view of the TT. [Sta10]

particles – such as the K_S – are rarely detectable in the VELO as the lifetime of a K_S is long enough that a large fraction decays after leaving the VELO. Therefore the Tracker Turicensis³ (TT), a silicon detector, is installed between RICH1 and the magnet, 232 cm from the nominal interaction point.

The TT consists of four layers called x , u , v , and x . The x layers contain strips parallel to the y axis – hence provide a measurement in x direction. u and v layers are rotated by the stereo angle 5° and -5° respectively. The layers are arranged in pairs separated by 27 cm.

The hit resolution of $50 \mu\text{m}$ suffices to provide momentum measurements dominated by multiple scattering. The length of the readout strips is chosen such that at expected multiplicities⁴ only a few percent of the strips are occupied.

The TT is located in the fringe field of the dipole magnet and therefore also provides a momentum estimate for low momentum particles being bent out of the acceptance of the following tracking stations.

Inner Tracker

In the T stations the region close to the beam pipe exhibits higher occupancy than the outer regions. Here a silicon strip detector similar to the TT is installed. Around the beam pipe four boxes are installed, the top and bottom box above and below the beam pipe respectively, and the A-side and C-side box left and right of the beam pipe (seen from the VELO).

The boxes overlap with each other and with the outer tracker to allow relative alignment and prevent gaps in the detector. The same strip pitch as in the TT is again sufficient to keep the occupancy below a few per cent at the expected particle density $1.5 \times 10^{-2} \text{ cm}^{-2}$.

³The TT is inconsistently also called Trigger Tracker [Col08].

⁴In the innermost region of the TT the expected density of charged particles is $5 \times 10^{-2} \text{ cm}^{-2}$ while in the outermost region it is two orders of magnitude smaller.

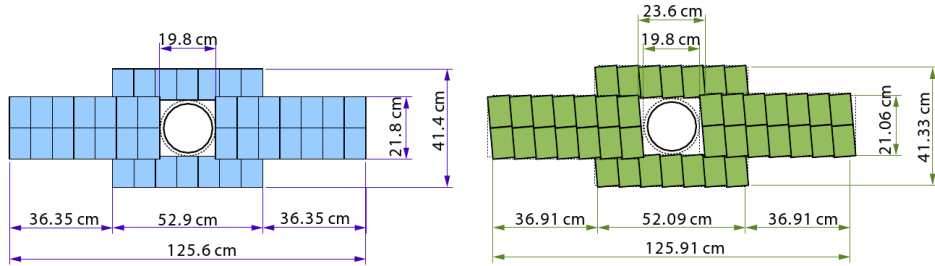


Figure 2.7: Schematic view of the IT. An x layer on the left side and a u layer on the right side. [Sta10]

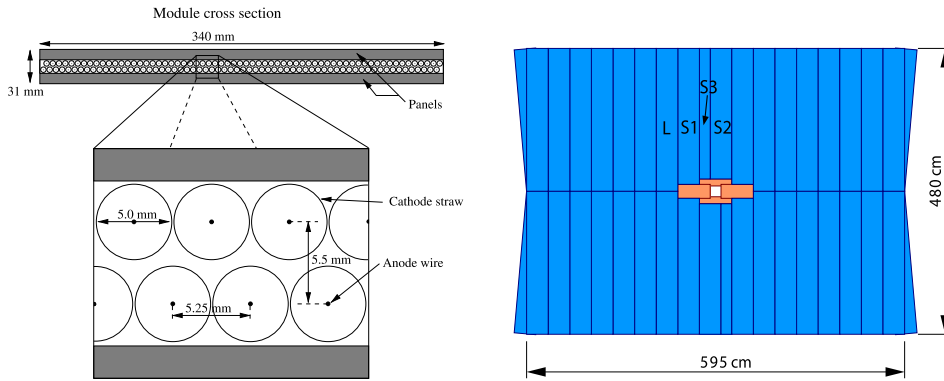


Figure 2.8: Schematic view of the outer tracker. On the left a cross section of a module revealing the double layer structure, on the right a front view illustrating the arrangement of the modules. [Sta10]

Again four layers, x , u , v , and x are used to provide measurements in x direction and additional y information from the layers tilted by 5° . In contrast to the TT there is no gap between the first and the second pair.

Outer Tracker

In the outer range of the T station trackers the outer tracker is situated to detect charged particles. It is a straw-tube detector which is organised in four double layers, two of them tilted by 5° . The double layer layout is shown in figure 2.8. The inner diameter of each straw is 4.9 mm and the detector provides a hit resolution of 200 μm if the electron drift time is considered. The hit resolution is again good enough to measure momenta up to the limit which is given by scattering in the detector material.

Up to a distance of 2 mm to the anode wire the hit efficiency has been measured to be above 97 %.

The inner boundary of the outer tracker is chosen such that the occupancy is below 10 % – the finer granularity of the inner tracker ensures a lower occupancy at the same particle density.

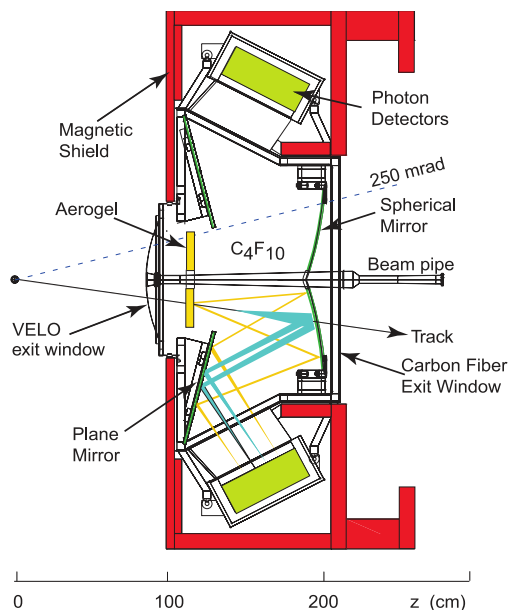


Figure 2.9: Schematic of RICH1 which contains two radiators being read out with the same photon detectors. The latter are located outside of the acceptance which allows the installation of the required shielding against radiation. [Col08]

2.5 Particle Identification Subdetectors

After tracks have been reconstructed they are combined with the signals from the particle identification system to identify the corresponding particles – i.e. determine the kind of particle the track belongs to.

RICH1 and RICH2

All particles in the acceptance of the detector pass through RICH1. It combines two radiator materials of different refractive index. Cherenkov photons, emitted by charged particles, are then focused with focusing mirrors and detected by hybrid photon detectors. RICH1 is installed in front of the magnet to identify even those particles which are bent out of the detector acceptance in the magnetic field.

To identify high momentum particles, another radiator is used in RICH2 with a smaller refractive index. RICH2 is situated behind the last tracking detector, in front of the calorimeters. Although the whole space from the beam axis to the outer ends of the LHCb acceptance is occupied only particles close to the beam axis, up to a polar angle of 100 mrad (vertical) and 120 mrad (horizontal), pass the radiator such that Cherenkov photons reach the HPDs.

Calorimeters

Both, scintillator pad detector (SPD) and preshower detector (PS) consist of rectangular scintillating pads sandwiching a 15 mm thick lead plate. They have been introduced to allow rejecting most of the background events in the electron trigger. To distinguish

the electrons from charged pions a longitudinal segmentation is required while neutral pions and photons are rejected requiring a signal in the PS before the shower is induced. The SPD is segmented into three areas of different granularity. PS and ECAL have the same layout projectively.

Both electromagnetic showers and hadronic showers may pass the borders between calorimeter cells. Instead of considering each cell with a signal as an individual particle, *clusters* are reconstructed. Such a cluster is the combination of adjacent cells with a signal. Adding the measured energies in the cells gives the total energy deposited in the cluster and weighting each cell position with the energy deposited in it provides a best estimation of the shower centre.

The ECAL consists of 66 layers of 2 mm lead and 4 mm scintillator. It corresponds to 25 electromagnetic radiation lengths. Therefore it can be assumed to absorb all photons and electrons entering it. The energy resolution has been measured to be better than⁵

$$\frac{\sigma_E}{E} \leq \frac{9.5\%}{\sqrt{E/\text{GeV}}} \oplus 0.8\%.$$

The HCAL is only segmented into two sections with larger cells corresponding to larger shower radii in a hadronic shower. The absorber material in the HCAL is iron which fills up the 1.2 m long subdetector besides the scintillator material. The energetic resolution for hadrons is much worse than for photons and electrons and has been measured to be $\sigma_E/E \leq 69\%/\sqrt{E/\text{GeV}} \oplus 9\%$.

Muon Stations

Particle identification using the calorimeters and both RICH detectors can separate electrons from hadrons and distinguish pions, kaons, and protons from each other. The remaining stable particle which needs to be identified for the physics program at LHCb, is the muon. Being too heavy to produce electromagnetic showers and not strongly interacting neither, muons are the only particles passing the calorimeters. Signals in the muon stations, downstream of the calorimeters, therefore identify muons.

Four of the five muon stations, M2 to M5, are situated behind the calorimeters while the first station is in front of the calorimeters as to be seen in figure 2.10. This first station is situated there to provide measurements before the muons' trajectories undergo multiple scattering in the calorimeter material. This improves the momentum resolution in the L0 trigger.

All stations are segmented in four regions (numbered from 0 to 3), the innermost region with the finest granularity. The layout of all stations is projective; with respect to M1 the stations M2 and M3 have twice the number of rows while M4 and M5 have half the number of rows.

In the reconstruction, tracks are extrapolated into the muon stations. Considering multiple scattering the number of hits in the muon stations M2 to M5 compatible with the track are counted. For tracks between 3 GeV and 6 GeV hits in M2 and M3 are required to decide in favour of a muon hypothesis, below 10 GeV a further hit in M4 or M5 is required and tracks above 10 GeV need a hit in each station to be identified as muons. Tracks with a momentum below 3 GeV are not considered to be identifiable as muons.

With this procedure it is possible that tracks close to each other are identified as muons using the same hits in the muon stations. For events with high multiplicity this

⁵ \oplus indicates quadratic addition, i.e. $a \oplus b = \sqrt{a^2 + b^2}$.

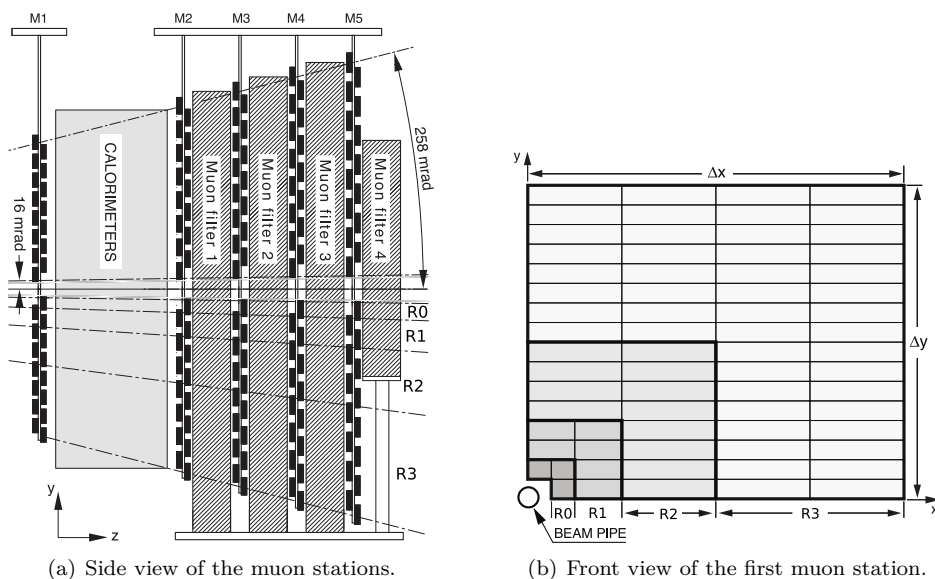


Figure 2.10: Schematic view of muon stations. The four regions of different granularity are indicated. [Col08]

leads to a high rate of misidentifications and it is investigated if assigning hits to only one track can improve this. [Alb10]

2.6 Trigger System

The trigger system at LHCb is divided into three stages, the level 0 trigger (L0), the first high level trigger (HLT1) and the second high level trigger (HLT2). Bunches in the LHC collide at 40 MHz and as a fourth of the bunch crossings contains an interaction which is *visible*⁶ to the detector, the L0 has 100 ns to decide if a bunch crossing is worth to be analysed by the high level trigger.

L0 is implemented in custom made electronics while the high level trigger is a software system operated at a CPU farm.

The high level trigger is designed to process one million events per second, which defines the maximum rate of events accepted by the L0 stage. The subdetectors which are easy and thereby fast to evaluate are the VELO's pile-up system, the calorimeters and the muon stations.

In the calorimeter the electron, photon, π^0 , and charged hadron with the largest transverse momentum are selected by assigning to each 2×2 cell array a particle hypothesis based on the measurements in the four subcalorimeters.

In the muon stations the two muons with the highest and second highest transverse momentum are selected. Similar to the track reconstruction presented in section 6.1 muon tracks are seeded from hits in M3 searching for hits along a straight line in the other four stations. The search windows in y are opened in M4 and M5 to take multiple scattering into account and in x in all stations to take the curvature in the magnetic

⁶Visible means that at least two charged particles coming from the interaction are reconstructible as longtracks.

field into account (see figure 6.1). The hits in M1 and M2 are used to calculate the transverse momentum as illustrated in figure 6.3.

The pile up system uses the two pile up sensors in the VELO to reconstruct tracks. Every combination of hits will lead to a track because there is always a line going through two points. These tracks are then extrapolated to the z axis. Correct reconstructed tracks from the same vertex will meet in a single point, whereas wrong combinations meet the z axis anywhere. If several vertices are found this way, a pile-up event – an event with more than one primary interaction – is identified.

In the high level trigger, reconstruction software is seeded with the positive decisions from the L0 trigger and tracks for the hadronic or muon candidates are reconstructed. The algorithms in use differ from those in the standard reconstruction in time consumption and precision. The aim in the first stage, HLT1, is to reduce the background rate about a factor 30 and the total output rate to 30 kHz.

In the second stage, HLT2, the complete event is reconstructed, again with algorithms optimised for fast computation. Whereas in HLT1 a limited number of tracks is reconstructed in a region of interest, HLT2 operates as close as possible to the standard reconstruction. The track fit, which is a main source of CPU consumption in the reconstruction, is simplified using less detailed material descriptions.

To analyse the influence of the trigger on a certain analysis, the events under investigation need to be classified if they have been stored and thereby entered the analysis due to a trigger decision which is independent of the analysis or dependent. In the former case the event is called TIS (trigger independent of signal). The latter case is called TOS (trigger on signal). A combination, several positive trigger decisions of which some are independent from the analysis and some are not, is called TISTOS.

2.7 Computing

The physics working groups of LHCb should not analyse all recorded events but only those which are of interest for the corresponding analysis. The recorded events are therefore provided in preselected *stripping streams*. As events can be of interest for several analyses, an event can be stored in several stripping streams.

For the creation of the stripping streams a full reconstruction is applied to all events which are afterwards analysed according to defined *stripping lines*. These stripping lines are definitions of criteria, an event has to fulfil to be considered as interesting for an individual analysis. All events selected by stripping lines of similar structure (i.e. lines with correlated decisions) then enter the same stripping stream.

The analyses performed in the stripping use standard particle selections, which require for most stable charged particles to be reconstructed as a longtrack. Only for the mentioned fields of interest (low momentum particles or decays behind the VELO) other track types are considered.

Stripping lines for analyses which do not need to consider the whole integrated luminosity are *prescaled*.

Track Reconstruction at LHCb

Ich will mir ja nächstes Semester
String Theorie anhören. Man
muss ja wissen, worüber man
lästert.

Jasper Franke

As stated in the previous chapter, charged stable particles are reconstructed as tracks in the tracking detectors. Dealing with the track reconstruction of LHCb in this work, in this chapter the tracking algorithms at LHCb are introduced.

3.1 Track Reconstruction in General

Each signal of a charged particle in a detector is called a *hit*. During the reconstruction hits are combined to find trajectories of particles which traversed the detector. To distinguish between the trajectories of real particles and the results of the reconstruction, the latter are called *tracks*. Tracks which are not trajectories of a particle but artefacts of the reconstruction are called *ghosts*.

Trajectories of charged particles are curved in a magnetic field and thus their tracks are curved as well. The curvature is determined by the magnetic field strength and the particle momentum which allows to calculate the particle momentum from the track curvature.

The process of finding hits from the same particle to reconstruct tracks is called *track finding*. Determining the parameters of the trajectory – x , y and the corresponding slopes t_x and t_y at a given z position, the momentum p and the charge q – is called *track fitting*.

Tracks are commonly reconstructed by starting the search for hits with a track segment from previous reconstruction steps or with hits in a certain detector layer. These starting points are called *seeds*. In combination with an assumed vertex position of particle production and a reasonable momentum assumption a seed determines a particle trajectory accurately enough to find further hits from the particle.

A sophisticated method to obtain optimal parameters for a track is the *Kalman filter fit*. It is a method of iteratively adding hits to a fitted track and improving the parameters in each step. This is done by first predicting the position of the particle in the plane of the next hit. The predicted position is then combined with the hit to get a position estimate which is more accurate than either the prediction or the hit.

The information about the new position estimate is afterwards used to obtain a best position estimate at every other hit as well. This method takes magnetic fields and material interaction into account as long as both are modelled.

Different models of the material distribution in the detector can be used. Using simple models, the Kalman fit is fast to compute while the parameter estimate is better when detailed models are used. If all available information is used, i.e. the most detailed model, the fit is called a *full Kalman fit* whereas the fit with a simple model is also called *fast Kalman fit*.

Fast Kalman fits are used in the high level trigger at LHCb.

Efficiencies in Tracking

There are different kinds of efficiencies which quantify the tracking performance. The first is the hit efficiency of a tracking detector. This is the probability of a detector to detect a traversing charged particle.

The hit efficiency is a detector property and obviously influences the probability of the reconstruction to find a track for a charged particle. The latter probability is the *track finding efficiency*, this efficiency will be analysed in this thesis.

The track finding efficiency (or short: *tracking efficiency*) is important to know and uncertainty on the tracking efficiency can enter the systematic errors of measurements. Especially every absolute measurement of a cross section takes the probability to reconstruct all decay products into account and therefore relies on a precise knowledge of the tracking efficiency.

If the trajectory of a particle is reconstructed twice, i.e. two tracks of one particle are reconstructed, these are called *clones*. Routines recognising ghosts are called *clone killer*.

3.2 Track Types and Tracking Algorithms at LHCb

In the process of track reconstruction tracks of different types are found representing different types of trajectories but also corresponding to different algorithms and stages in the reconstruction. A schematic classification of tracks at LHCb is given in figure 3.1. In general longtracks are the favourite choice to use in a physics analysis as they provide the best momentum resolution whereas other tracks also have to be used in certain cases.

The tracking algorithms are designed for nominal detector performance and ideal alignment. The latter means that the position of every detector module is accurately known which is not the case in the first months of operation. Therefore an “early data tuning” has been introduced which imposes less hard requirements to the reconstructed tracks in terms of a minimum number of hits. The early data tuning has been used for all results and analyses in this work. Independent of potential alignment issues it turned out that the hit requirements for all track types were too strict with the settings which were developed in simulations. [HM10]

Several algorithms exploit the principle that the magnetic dipole field can be approximated by a single bending plane, i.e. that trajectories are straight lines with a kink at the bending plane.

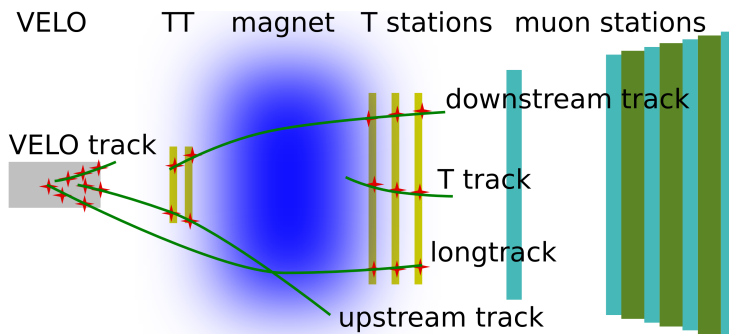


Figure 3.1: The different track types in the reconstruction. Hits in different subdetectors are indicated. Longtracks may as well go through the TT and use hits there but these are not required.

Velo Track Reconstruction

The reconstruction of tracks in the VELO is split up into two steps. In the first step only the r sensors are used to reconstruct tracks in a r - z plane for each of the polar segments. The residual magnetic field in the VELO is negligibly small which allows to search only for collinear hits. In the second step these r - z tracks are combined with the information from the ϕ sensors to get the position of the tracks in three-dimensional space. For computing reasons only a simplified track fit is done once the Velo tracks are found. The Velo tracks are then used to find longtracks, sophisticated fits are postponed to the longtrack reconstruction. Velo tracks which are not used for any longtrack are fitted at the end of the track reconstruction with a full Kalman fit.

T Track Reconstruction

In contrast to the Velo track reconstruction, the assumption that particle trajectories are straight is wrong in the T stations located in the magnet's fringe field. In the first stage of the reconstruction of track segments in the T stations, only the x layers of the inner tracker and outer tracker are used. In the x - z plane¹ – where the magnetic field causes a curvature – parabolas are searched. To not allow any combination of hits in the three stations, the parameters of the parabolas are constrained such that the track extrapolation through the magnet roughly reaches the interaction region.

The found track segments in the x - z plane have one degree of freedom left if it is assumed that the particles come from the interaction region and that the magnetic field causes no curvature in the y - z plane. The slope t_y is then determined by combining the track segments from the x - z plane with hits in the u and v layers. There can always be only a few u and v hits compatible with the track, because knowing the x position of a particle transition through a layer and knowing which straw/strip has been hit determines the y position of the transition.

The number of hits in the u and v layers is, in other words, a function of the assumed track slope t_y . For the slope with the maximum number of hits, the compatible u and v layer hits are assigned to the track and a track fit is performed. [Sch; CS08]

¹The straws and strips in the T station trackers provide almost only a measurement in the x - z plane. Whether a hit is in the IT or in the OT gives limits for the y position.

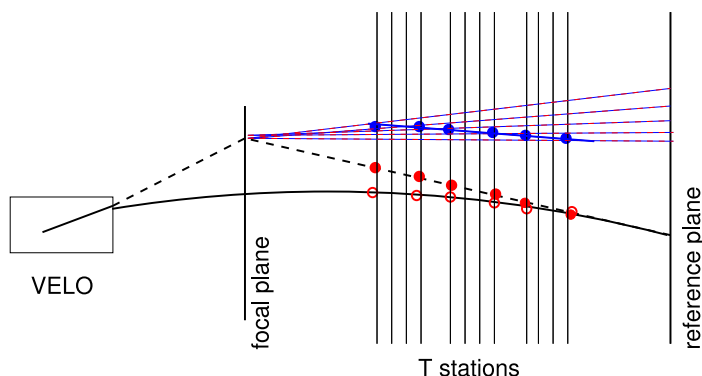


Figure 3.2: Schematic view of the cluster search in the forward tracking algorithm. In the Hough transformation the actual cluster positions (rings) are shifted. The transformed positions (filled circles) are then projected from the Velo track extrapolation in the bending plane to the reference plane. [HM08]

Longtrack Reconstruction

Longtracks are by definition tracks having hits in the VELO and the T stations. Technically they are built from Velo tracks and therefore depend on the Velo track reconstruction. There are two ways to get the additional hits in the T stations. Either the Velo tracks are matched to T tracks or Velo tracks are used to seed the search for further *hits* in the T stations.

The two algorithms are called *track matching* and *forward tracking* respectively. The matching algorithm is similar to the one described in chapter 6 – T tracks and Velo tracks are extrapolated to the magnet’s bending plane and the distance between the extrapolated positions in the x - z plane is calculated for each pair in units of χ^2 , hence the significance of the distance is calculated. The distance in y is determined at the first T station. [Cal07]

In the forward tracking algorithm Velo tracks are as well extrapolated linearly to the bending plane. Afterwards a Hough transformation² is applied to the hits in the T stations such that hits from the particle, which was reconstructed as the initial Velo track, are shifted onto a straight line which intersects the bending plane at the same position as the Velo track extrapolation (see figure 3.2). [HM08]

To improve the track fit and thereby the momentum resolution, hits in the TT can be added to a longtrack. Further details are given in [dC10b].

Downstream Track Reconstruction

Downstream tracks, in contrast to longtracks, do not require hits in the VELO but are reconstructed from TT hits and T tracks instead. The main purpose is to reconstruct particles which are produced in decays of neutral particles which decay after leaving the VELO inside of RICH1.

The strategy of the downstream reconstruction is to extrapolate T tracks to the magnet’s bending plane and pick up hits in the TT around a straight line towards

²Highly simplified a Hough transformation transforms complex shapes into simple shapes according to a model.

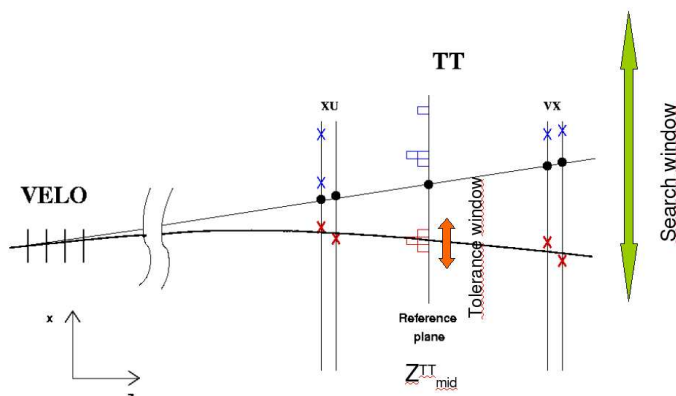


Figure 3.3: Schematic of the upstream track reconstruction. [CKW07]

the nominal interaction point. The search window is chosen such that particles from long-lived particles' decays can be reconstructed as described in [Sta10, section 3.1.3].

The downstream tracking algorithm as well reconstructs particles originating in the VELO. Downstream tracks can therefore be used to reconstruct particles which have not been found by the longtrack reconstruction due to inefficiencies in the VELO or in either longtrack algorithm. That reconstruction has been used by [Wan10a] to measure the tracking efficiency in the VELO.

Upstream Track Reconstruction

The upstream track reconstruction is similar to the downstream track reconstruction. It is implemented to reconstruct particle trajectories using the VELO and the TT which allows the reconstruction of low momentum particles which are bent out of the detector acceptance in the magnetic field.

Velo tracks are extrapolated linearly to the TT in which hits are searched for in a search window. The straight line assumption is equivalent to an infinite momentum and therefore the size of the search window determines the minimum momentum of reconstructible tracks.

The deviation of hits from the straight line are then projected to the TT's central plane where a coincidence of hits from all four layers is assumed to be a sign for hits from the particle which has been reconstructed as the initial Velo track. In figure 3.3 such a coincidence of projections is illustrated by the red boxes. The blue hits are not projected to such a coincidence in the central plane.

Muon Track Reconstruction

The standard track reconstruction does not comprise a track reconstruction in the muon stations. However muon track segments will appear later in this work. The terminology here is treacherous: Names of tracks are given according to the subdetector in use and not according to the kind of particle which is reconstructed. Muon track segments will therefore be tracks in the muon stations (fortunately muons are the only particles which reach the muon stations) while "tracks of muons" refer to any type of track which reconstructs a muon. Given that standard tracks are not reconstructed in

3. TRACK RECONSTRUCTION AT LHCb

the muon stations a “track of a muon” will *not* be reconstructed from hits in the muon stations but a particle hypothesis is assigned to the track as described in section 2.5.

The Tag and Probe Method

Schönes Wochenende.
Nicht bis morgen.

Ulrich Uwer (18.06.2010)

The efficiency to reconstruct the trajectory of a charged particle in a subdetector \mathcal{S} is estimated by the fraction of successfully reconstructed particles among all charged particles passing through \mathcal{S} .

$$\varepsilon = \frac{\text{\#particles reconstructed in } \mathcal{S}}{\text{\#charged particles passing through } \mathcal{S}}$$

To calculate this ratio, knowledge of particles which passed through \mathcal{S} is needed. A sample of those particles can be obtained by using independent subdetectors to reconstruct charged particles. The latter signatures are called *probes*. If a probe is also reconstructed in \mathcal{S} it is said to be *confirmed* which is illustrated in figure 4.1. Among the probes there can be ghosts. For G ghosts in A probes and corresponding g ghosts in C confirmed probes, considering all probes will therefore lead to a wrong result.

$$\frac{C}{A} \neq \frac{C - g}{A - G} = \varepsilon$$

As it cannot be said for any probe if it is a ghost, an advanced method is needed to measure the efficiency correctly.

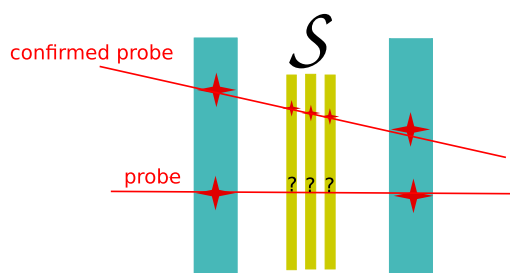


Figure 4.1: Illustration of the principle to probe a subdetector. For each probe it is tested if the probe has been detected in the subdetector which is tested. If a probe is detected in the subdetector, the probe is said to be *confirmed*.

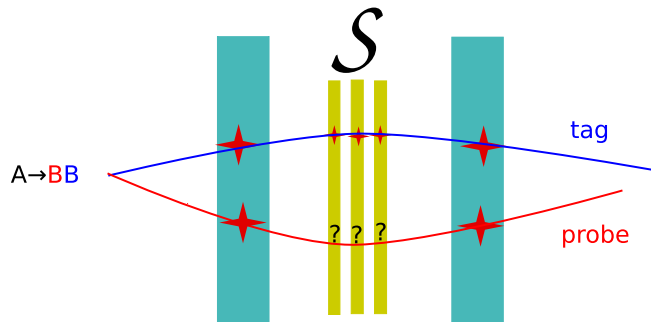


Figure 4.2: Sketch of the tag and probe method. A full reconstructed decay product (blue) from a two body decay is used to tag the signature (red) which is used to probe the subdetector \mathcal{S} .

4.1 Sketch of the Tag and Probe Method

The tag and probe method is a method to measure the efficiency without a bias arising from ghost probes.

Probes are *tagged* if a two body decay can be reconstructed using the probe and a full reconstructed track as illustrated in figure 4.2. From the according invariant mass spectrum of all reconstructed decays the number of correct reconstructed decays can be estimated which does not comprise ghosts.

Restricting to confirmed probes, the number of probes from correct reconstructed decays which are also found in \mathcal{S} is accessible. This allows the calculation of the efficiency.

$$\varepsilon = \frac{\#\text{confirmed probes from correct reconstructed decays}}{\#\text{probes from correct reconstructed decays}}$$

The two body decays which are used in the tag and probe method need to be easy to identify because not the entire detector can be used for their reconstruction (the probe does must be independent of \mathcal{S}).

4.2 Tracking Efficiencies from the Simulation

The efficiency to reconstruct tracks can as well be determined in the simulation where it is certain which of the simulated particles has been reconstructed and which of the tracks are ghosts. Such a determination is generally more precise than a measurement involving the tag and probe method.

The tag and probe method is applied to data from LHCb as well as to the according simulations to validate that the track reconstruction efficiency is simulated correctly. The difference between the value from the simulation and the measured value is then treated as a systematic uncertainty on all efficiencies obtained from the simulation.

4.3 Application of the Tag and Probe Method in LHCb

The performance of the T trackers is investigated in this thesis using the tag and probe method. For the decay $K_S \rightarrow \pi^+\pi^-$ probes found in the VELO and in the calorimeters

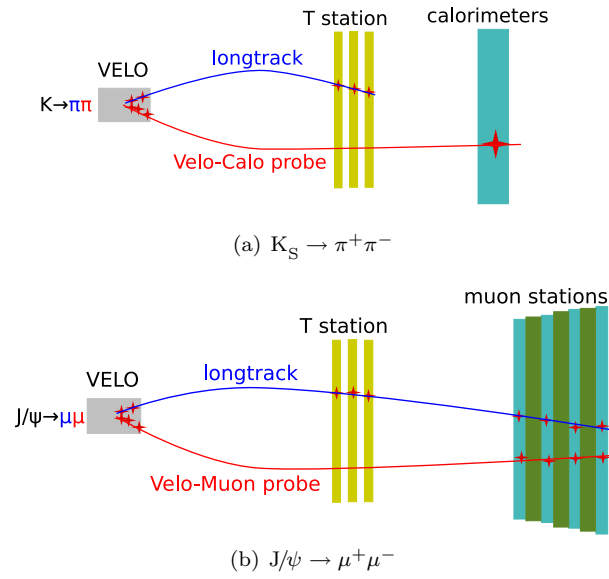


Figure 4.3: Two body decays used to measure the tracking efficiency of the T station trackers.

are used (see figure 4.3(a)) and for the decay $J/\psi \rightarrow \mu^+ \mu^-$ probes are taken from the VELO and the muon stations (see figure 4.3(b)).

Probes for the Tracking System from the Calorimeters

Ich muss vor dem 11.6. fertig werden. Da fängt die WM an.

Sascha Stahl

To measure the tracking efficiency with the tag and probe method, probes are reconstructed from the clusters in the calorimeters which are independent from the T station trackers.

5.1 Principle of Reconstructing Velo-Calorimeter Probes

Charged pions are absorbed in the calorimeters and reconstructed as clusters. The clusters provide information about the position where the pion entered the calorimeter and the deposited energy. With a mass hypothesis and an assumed origin of the pion in the VELO the pion trajectory is roughly determined up to a charge ambiguity.

Velo tracks representing the same particle which is detected as a calorimeter cluster are found by extrapolating them linearly to calorimeter. In the y - z plane the extrapolated Velo tracks has to meet the cluster because trajectories are straight lines in that plane. In the x - z plane however trajectories are curved and the x_{kick} , illustrated in figure 5.1, depends on the momentum and the charge.

$$x_{\text{kick}} = x_{\text{extrapolated Velo track}} - x_{\text{calorimeter cluster}} \propto q/p$$

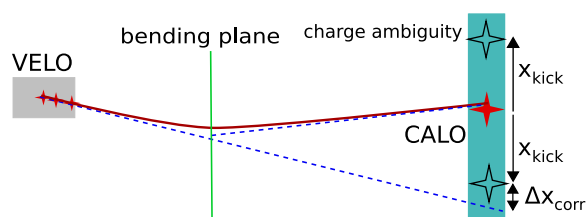


Figure 5.1: Principle of Velo-Calorimeter matching in the x - z plane. The position of the calorimeter cluster is shifted by the x -kick which is determined using the energy measurement in the calorimeter. For correct treatment of the charge ambiguity the kick is applied in both directions and the direction with the smaller Δx_{corr} assumed to be correct.

5.2 Detailed Explanation

The matching of calorimeter clusters to Velo tracks is already used in the first high level trigger. The following computation how good signatures in the VELO and the calorimeters are compatible to each other has been implemented by [Zwa06].

χ^2 Computation

How good a Velo track and a calorimeter cluster match is quantified by

$$\chi^2 = \left(\frac{\Delta y}{\sigma(\Delta y)} \right)^2 + \left(\frac{\Delta x_{\text{corr}}}{\sigma(\Delta x_{\text{corr}})} \right)^2.$$

Here Δy is the difference between the y position of the Velo track extrapolation and the y position of the calorimeter cluster and Δx_{corr} is the difference between the x position of the Velo track extrapolation and the x position of the calorimeter cluster *after* taking x_{kick} into account as indicated in figure 5.1.

The calculation is done as follows. The variables x , y , z and the energy E refer to the calorimeter cluster while t_x and t_y are the slopes of the Velo track. Hence no z information from the Velo is used – Velo tracks are supposed to originate in $(0, 0, 0)$.

$$\Delta y = \frac{y}{z} - t_y$$

$$\Delta x_{\text{corr}} = \min_{q \in \{\pm 1\}} \left(\frac{x - qx_{\text{kick}}}{z} - t_x \right)$$

x_{kick} is determined by the energy deposited in the calorimeters.

$$x_{\text{kick}} = C_{\text{kick}} \frac{z - z_{\text{magnet}}}{E}$$

Hereby it is assumed that the magnetic field can be described as a single bending plane at $z = z_{\text{magnet}} = 5\,250$ mm. C_{kick} is a measure for the curvature due to the magnetic field and has been determined in simulations ($C_{\text{kick}} = 1.263$ GeV).

For the y contribution to χ^2 only the spatial resolution of the calorimeters is taken into account, the Velo track slope can be assumed to be perfect.

$$\sigma(\Delta y) = \frac{1}{z} \cdot \frac{4 \times \text{cell size}}{\sqrt{12}}$$

The determination of Δx_{corr} has two independent contributions.

$$\sigma(\Delta x_{\text{corr}}) = \frac{1}{z} \sqrt{\sigma_x^2 + \sigma_{x_{\text{kick}}}^2}$$

The former is again the spatial resolution of the calorimeter.

$$\sigma_x = \frac{4 \times \text{cell size}}{\sqrt{12}}$$

Table 5.1: Velo-Calo matching efficiencies for different χ^2 cuts, different decay channels and different beam energies. All numbers are determined in simulated events.

(a) Collisions at 900 GeV.

χ^2	ε	ε (π from K_S)	ghost fraction
5	$96.9 \pm 0.1\%$	$96.0 \pm 0.2\%$	92.2%
2	$93.8 \pm 0.1\%$	$92.4 \pm 0.3\%$	88.8%
1	$90.2 \pm 0.1\%$	$87.9 \pm 0.4\%$	85.5%
0.75	$88.2 \pm 0.1\%$	$85.6 \pm 0.4\%$	83.8%

(b) Collisions at 7 TeV.

χ^2	ε	ε (π from K_S)	ghost fraction
5	$97.6 \pm 0.2\%$	$96.0 \pm 0.3\%$	96.9%
2	$95.1 \pm 0.2\%$	$92.2 \pm 0.5\%$	95.6%
1	$91.9 \pm 0.3\%$	$87.1 \pm 0.6\%$	94.2%
0.75	$89.8 \pm 0.3\%$	$83.8 \pm 0.7\%$	93.6%

(c) Collisions at 10 TeV.

χ^2	ε	ε (π from K_S)	ghost fraction
5	$97.78 \pm 0.05\%$	$96.5 \pm 0.1\%$	97.1%
2	$95.49 \pm 0.07\%$	$92.8 \pm 0.2\%$	95.8%
1	$92.39 \pm 0.09\%$	$88.1 \pm 0.2\%$	94.5%
0.75	$90.33 \pm 0.10\%$	$85.2 \pm 0.2\%$	93.9%

The latter is uncertainty on the determination of x_{kick} from the energetic resolution.

$$\begin{aligned}
 \sigma_{x_{\text{kick}}} &= x_{\text{kick}} \frac{\sigma_E}{E} \\
 \frac{\sigma_E}{E} &= 60\% \oplus \frac{70\%}{\sqrt{E/\text{GeV}}} \\
 &:= \sqrt{0.6^2 + \frac{0.7^2}{E/\text{GeV}}}
 \end{aligned}$$

Table 5.1 shows the efficiency of matching Velo tracks to calorimeter clusters as a function of the maximum allowed χ^2 value. If $\chi^2 < 1$ the match is supposed to be correct. Due to the low resolution of the calorimeters still most of the probes are ghosts.

Charge and Momentum Estimation

Combining the slope of the Velo track with the position of the calorimeter cluster a momentum estimate, which is more precise than the energy measurement in the calorimeter, can be made. This time the z position of the first hit in the VELO is considered.

$$x_{\text{kick}} = x_{\text{Velo}} + t_{x \text{ Velo}}(z_{\text{Calo}} - z_{\text{Velo}}) - x_{\text{Calo}}$$

$$\frac{1}{p} = \left| \frac{x_{\text{kick}}}{C_{\text{mom}}} \right|$$

C_{mom} here is different from the above C_{kick} :

$$C_{\text{kick}} = 1.263 \text{ GeV}$$

$$C_{\text{mom}} = 9.950 \text{ m/GeV}$$

Given that in the latter case of the momentum estimation more information is used, the constants are calibrated independent from each other. For technical reasons C_{kick} was determined maximising the matching efficiency in the simulation while C_{mom} could be adjusted using data with respect to the longtrack momentum estimate for confirmed Velo-Calorimeter probes.

The charge of the probe is

$$q = \begin{cases} 1 & \text{if } x_{\text{kick}} > 0 \\ -1 & \text{if } x_{\text{kick}} < 0 \end{cases}$$

for upward field polarity and vice versa for the opposite field polarity.

Whether the simple model of a bending plane can be used has been investigated in simulated data by studying correlations between the Velo track parameters, the cluster position and the momentum pull $(p_{\text{simulation}} - p_{\text{estimate}})/p_{\text{simulation}}$. Those correlations are observable but small enough to be neglected for the study (see figure 5.2).

5.3 Further Development of Velo-Calorimeter Matching

The treatment of the charge ambiguity illustrated in figure 5.1 can be omitted because for a given pair of a Velo track and a calorimeter cluster the curvature in the magnetic field is already determined. The shift x_{kick} is therefore only applied into the direction which will minimise χ^2 as shown in figure 5.3.

Velo-Calorimeter matching in the trigger is performed before longtracks are reconstructed. The present study however is performed after the longtrack reconstruction. Velo tracks therefore have been fitted using hits in the T stations if they are used for the reconstruction of longtracks (see section 3.2).

No bias from these different fits is allowed because the reconstruction of longtracks is to be probed with Velo-Calorimeter probes. Hence all Velo tracks are refitted with a full Kalman filter fit before the reconstruction of Velo-Calorimeter probes.

The algorithm in the trigger is optimised to match high momentum tracks which originate in an interaction close to the nominal interaction point. As the z position of the first hit in the Velo is not taken into account in the computation of χ^2 it has to be tested whether the average χ^2 is shifted towards larger values for large z values of the first hit of the Velo track.

Figure 5.4 shows the average χ^2 as a function of the first Velo hit for correct matched Velo-Calorimeter probes in simulated events. No significant shift towards larger χ^2 values can

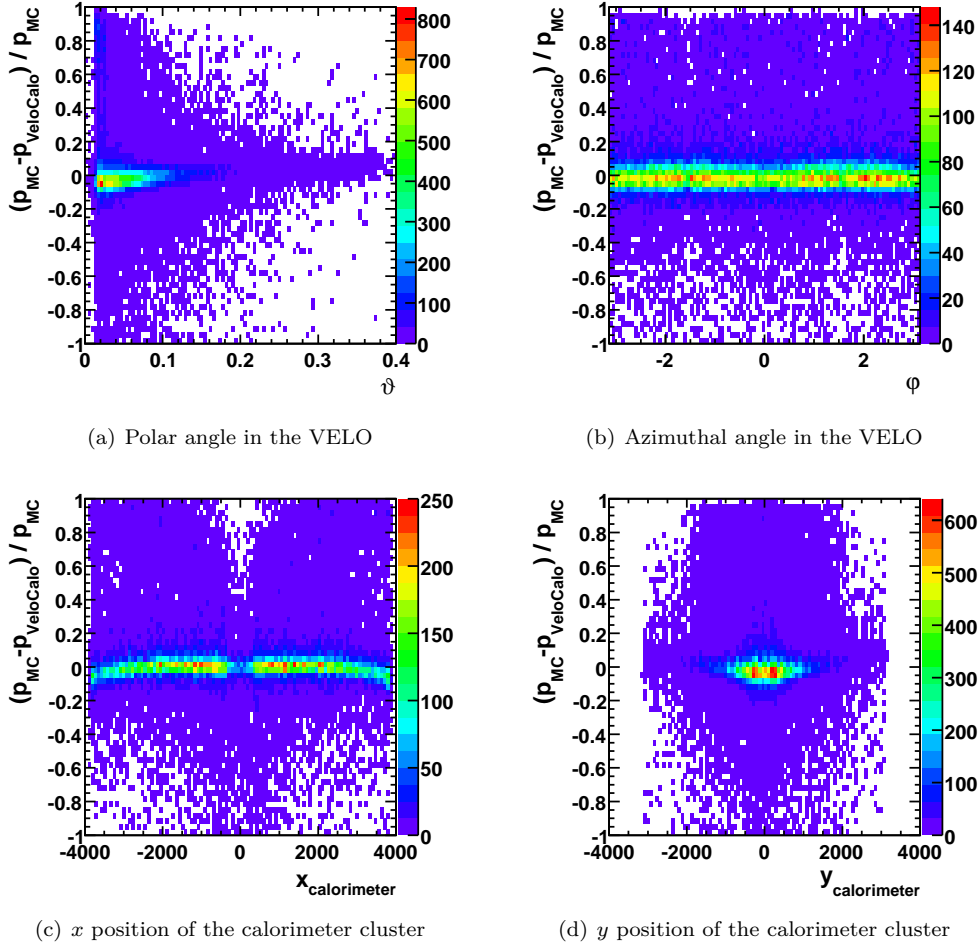


Figure 5.2: Momentum pull as a function of different parameters.

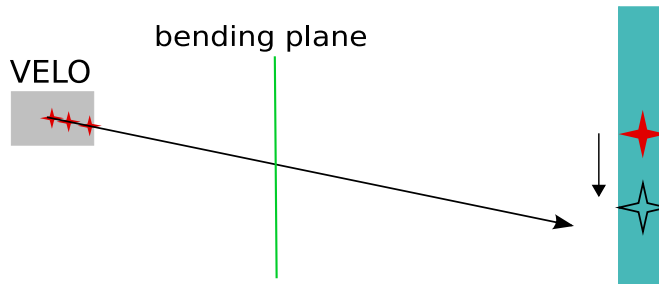


Figure 5.3: For a given pair of a Velo track and a calorimeter cluster, the direction of x_{kick} is already determined.

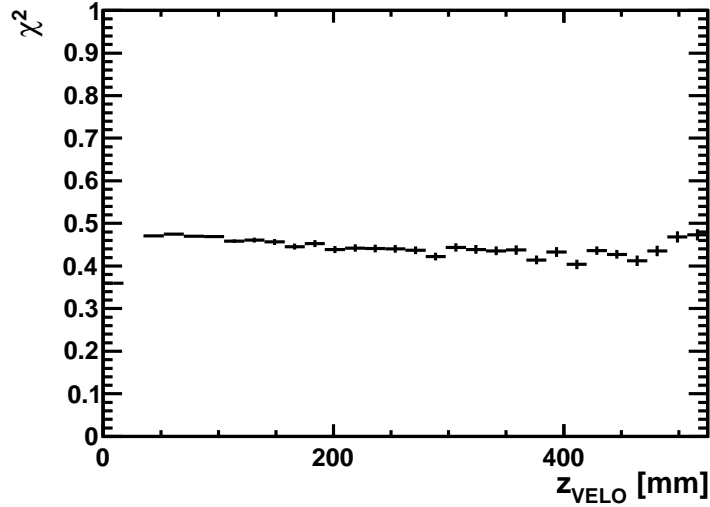


Figure 5.4: The average matching χ^2 for correct combinations of Velo tracks with calorimeter clusters as a function of the z position of the first Velo hit in the region of interest. The underlying events were simulated.

be observed. Moreover χ^2 for correct combinations is in average well below 1, the value up to which Velo-Calo probes are taken into consideration as correct matches.

The distribution of χ^2 for correct matches is shown in figure 5.5 as a function of the inverse momentum. The inverse momentum is chosen because x_{kick} is proportional to it and a wrong calibration of C_{kick} is expected to be visible as a shift towards larger χ^2 for large inverse momenta. Again, no such shift can be observed.

Calorimeter clusters are reconstructed for all particles absorbed in the calorimeters. Charged pions are in the particle identification for longtracks identified by a signal in the SPD, which rejects neutral particles, and by requiring deposited energy in the HCAL, which rejects electrons.

In section 10.3 it is shown that restricting Velo-Calo probes to probes from clusters with a signal in the SPD and the HCAL does not improve the tracking efficiency study.

Momentum Resolution

The momentum resolution of Velo-Calo probes is shown in figure 5.6 with respect to the simulated momentum. The mean squared error on the estimate is below $(7.35\%)^2$. The downstream track reconstruction for comparison has a momentum resolution of less than 1%. [Sta10]

For confirmed Velo-Calo probes the momentum of the Velo-Calo probe can be compared to the momentum of the confirming track. Thereby the magnetic field, i.e. C_{mom} , can be calibrated on data. The corresponding plot is shown in figure 5.7 for simulated data and for measured data. A large fraction of wrong momentum estimates is visible which is due to the fact that ghost probes can be confirmed.

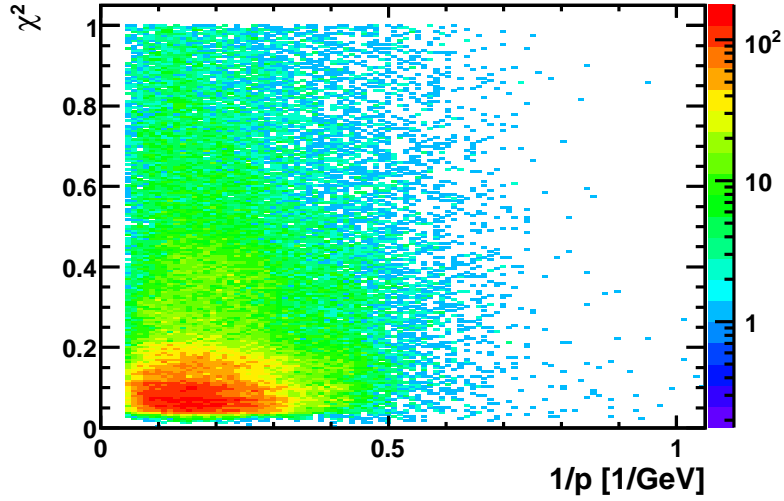


Figure 5.5: Matching χ^2 for correct combinations of Velo tracks with calorimeter clusters as a function of the inverse momentum. The cut at $\chi^2 = 1$ is already applied. The underlying events were simulated.

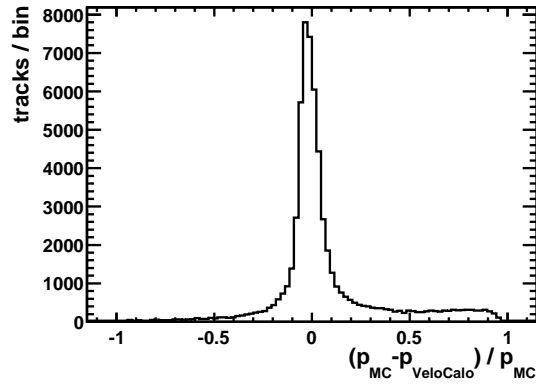


Figure 5.6: Comparison of the momentum determined by Velo-Calo tracking to the simulated value. The histogram shows $(p_{\text{reference}} - p_{\text{VeloCalo}})/p_{\text{reference}}$. The mean is $-1.36 \pm 0.03 \%$, the RMS is 7.22% .

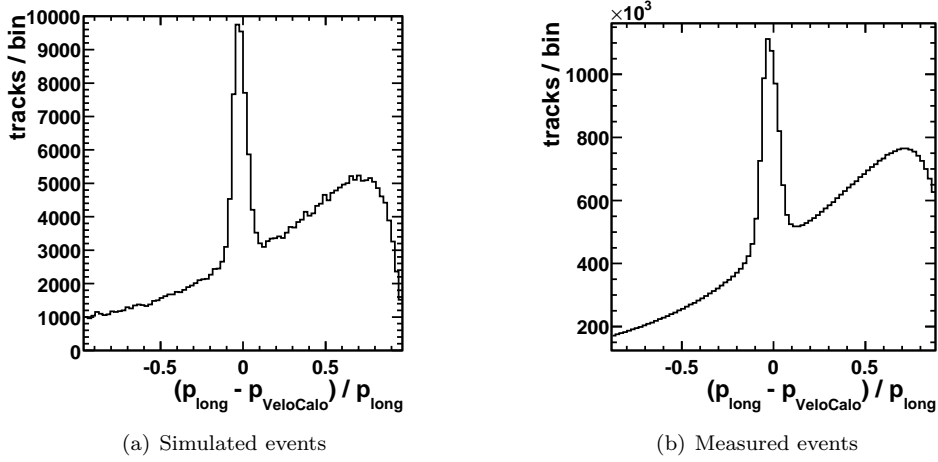


Figure 5.7: Comparison of the momentum determined by Velo-Calo tracking to the momentum estimate of the longtrack reconstruction. The histograms show $(p_{\text{reference}} - p_{\text{VeloCalo}})/p_{\text{reference}}$. The background is from Velo-Calo ghosts which are confirmed. The Velo-Calo momentum estimate in this case is meaningless. The Velo-Calo momentum estimate is smaller than the longtrack momentum, the relative difference is between 0 and 1 and between $-\infty$ and 0 in the opposite case. Thus the background from small Velo-Calo momenta is concentrated below 1.

The momentum resolution compared to the longtrack reconstruction reveals an offset of $-2.02 \pm 0.04 \%$ with an RMS of 4.41 % in simulated events and $-2.01 \pm 0.01 \%$ with an RMS of 5.26 % in measured data.

Further Background Reduction

The selection of $\chi^2 < 1$ tracks still allows that a Velo track has been used for several Velo-Calo probes and that a calorimeter cluster has been used for several Velo-Calo probes. This ensures that the correct matches are among the probes

It is a common way to reduce the number of ghosts by taking only the “best” probe from a set of possible candidates using the same seed. The best probe is the one with the least χ^2 . A wrong combination may still have a smaller χ^2 than the correct combination.

Which of the two effects – reducing the number of ghosts and decreasing the probability to keep correct combinations – dominates the background reduction is tested on data in section 7.5. From the following five configurations the third one is used.

1. Taking all Velo-Calo probes (no background reduction).
2. For each Velo track, using only the calorimeter cluster which matches best.
3. For each calorimeter cluster, using only the Velo track which matches best.

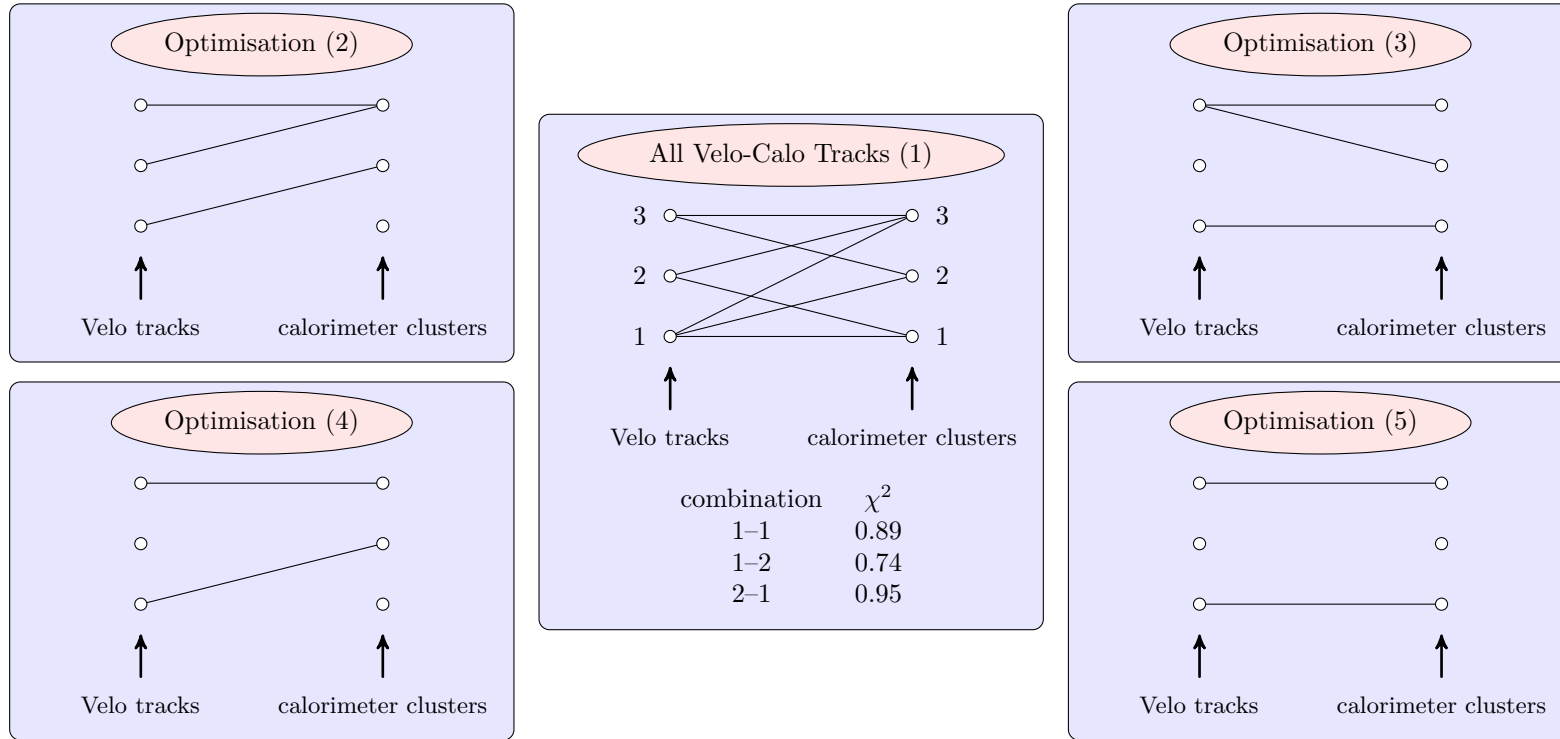


Figure 5.8: Schematic of the optimisation schemes. Each circle represents a Velo track or calorimeter cluster. A line connecting them represents the Velo-Calorimeter probe using both. For three combinations χ^2 values are given to illustrate that requiring each Velo track and each calorimeter cluster to be used only once does not determine the result – optimisations 4 and 5 differ.

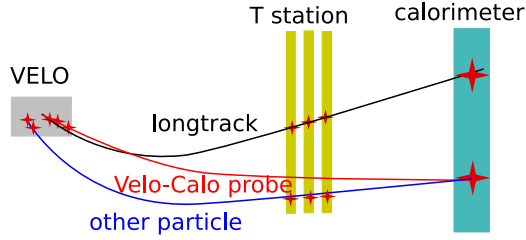


Figure 5.9: A wrong reconstructed Velo-Calo track (red) being confirmed by a correct reconstructed longtrack (black).

4. For each Velo track, using only the calorimeter cluster which matches best. Afterwards, test if a cluster is used several times and keep from those Velo-Calo track the best one.
5. For each calorimeter cluster, using only the Velo track which matches best. Afterwards test if a Velo track is used several times and keep from those Velo-Calo track the best one.

The configurations are also illustrated in figure 5.8.

The effect on the later measurement of these configurations and the reason for preferring the third option are explained in section 7.5.

5.4 Velo-Calo Probe Confirmation

For the measurement of the tracking efficiency for each probe is decided whether it has been found by the standard track reconstruction in the T stations. Given that Velo-Calo probes and longtracks are reconstructed from Velo tracks a Velo-Calo probe is confirmed if a longtrack is found which is built from the same Velo track. As illustrated in figure 5.9 the longtrack in black confirming the Velo-Calo probe does not necessarily need to be a track similar to the Velo-Calo probe. The effect of such wrong confirmations on the measurement is shown in section 7.4.

For the analysis of the downstream tracking efficiency or the efficiency of the T track reconstruction such a confirmation based on common segments cannot work as neither T tracks nor downstream tracks have any hit in common with a Velo-Calo probe.

As shown by [Sto10], such a confirmation can be done extrapolating the probes to a fixed plane at the end of the T stations. If there is a standard track within a search window around the Velo-Calo extrapolation with compatible slopes, the Velo-Calo probe is confirmed (see figure 5.10).

Studies on simulated data have shown that a search window size of 10 cm in x and y , and 3 mm/m in t_x and t_y confirm 97 % of Velo-Calo reconstructed pions which are also reconstructed in the T stations while 0.5 % of the confirmations are confirmations of pions which are not reconstructed in the T stations.

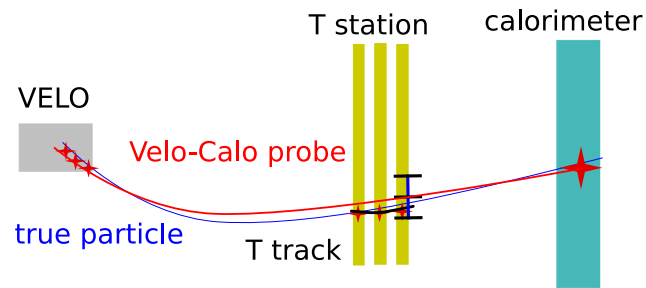


Figure 5.10: Velo-Calo probes for the measurement of the T track reconstruction efficiency are confirmed if a T track (bold black) is in the T stations within a search window around the predicted trajectory of the Velo-Calo probe. For better visualisation, the deviation of the reconstructed trajectories and the true trajectory (thin blue) is exaggerated. Not indicated is that the T track parameters t_x and t_y also have to be in agreement with the Velo-Calo probe parameters. The confirmation with downstream tracks is done analogously.

Probes for the Tracking System from the Muon Stations

Also eigentlich ist mir egal, ob
jetzt J/ψ suppression oder
enhancement. In jedem Fall sieht
man was in der Signatur.

Jan de Cuveland

An alternative approach to the reconstruction of Velo-Calo probes is matching Velo tracks to muon track segments. Before turning to the matching of Velo tracks to muon track segments in section 6.2 the reconstruction of muon track segments is discussed in the first section.

6.1 Track Reconstruction in the Muon Stations

The standard track reconstruction at LHCb (see section 3.2) does not comprise a track reconstruction in the muon stations. Nevertheless in the HLT1 muon track segments are reconstructed to seed the search for tracks from muons. Moreover, to monitor the hit efficiency of the muon stations a track reconstruction in the muon stations has been implemented for the online monitoring. The algorithm used in the trigger is called `HltMuonRec` and the one used in the monitoring `MuonCombRec`. By default both algorithms start the search for muon tracks in the last station, i.e. M5, and use hits in that station as seeds. In each step the search is continued in the adjacent station towards the interaction region. As in the first step no information on the slope of the track to reconstruct is available the assumption of a straight line to the interaction region is used to extrapolate the hit to M4 (figure 6.2(a)). In the y - z plane, where the curvature due to the magnetic field is negligible, this assumption is convenient while in the x - z plane this only holds for infinite momenta.

Around the extrapolated position hits are searched for in a search window. As illustrated in figure 6.1 the size of the search window in x direction imposes a lower limit on the momentum of reconstructible muons. The search window is chosen such that the deviation from the straight line due to the curvature is smaller than the search window for momenta in the range of interest. If there is more than one hit in the search window a best one is determined by calculating the distance h between the predicted position and the position of the hit (figure 6.2(c)). The hit with the smallest distance h is taken which makes the reconstruction favour high momentum tracks.

Once hits in different stations are found, a straight line between the hits in adjacent stations is used to predict the position of hits in the next station (figure 6.2(b)).

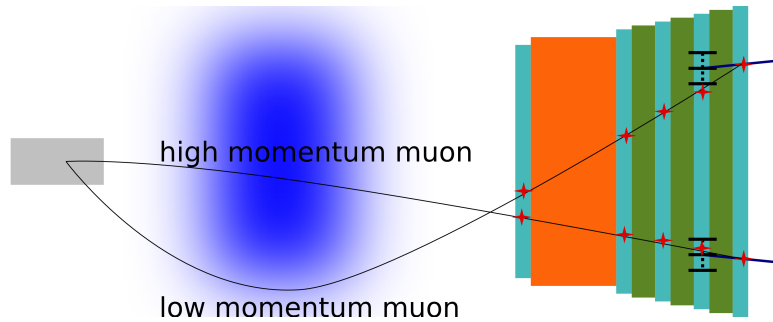


Figure 6.1: While a small search window is sufficient for a high momentum particle, the low momentum particle will not be reconstructed with the indicated search window. The thin black lines are the real trajectories of the muons, the bold dark blue lines indicate the straight line towards the interaction region which defines the search window in M4.

The search for hits is repeated until M1 (in case of `MuonCombRec`) or M2 (in case of `HltMuonRec`) respectively is reached.

If no hit for a track is found in a station the reconstruction of the track is not continued. To be reconstructed, a particle needs to be detected in each of the stations which is used for the reconstruction. `MuonCombRec` offers the possibility to skip a selected station as well as the option not to start at M5. Independent of the selected seed station the search is only performed towards the interaction region – starting in M3 results in not using M4 and M5. In the case where a station is selected to be skipped, the extrapolation is extended to the next station which is to be used. This makes the reconstruction independent from the skipped station – missing hits neither cause truncation nor can hits in that station improve the reconstruction.

`MuonCombRec` provides the possibility to recognise clusters or crosstalk. If there are hits in cells adjacent to the best hit these are also added to the track.

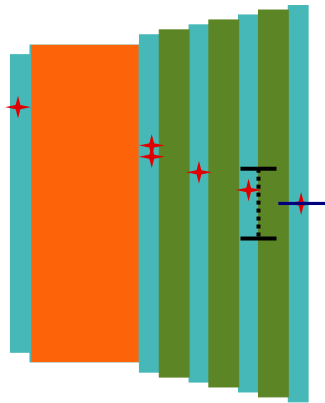
Figure 6.2 shows the case of `MuonCombRec` neither using the possibility to skip a station nor adding crosstalk to the track.

The main contribution to the reconstruction of clones are those cases where hits in M5 are close to each other but not treated as crosstalk. Both hits will serve as a seed for a track and the algorithms are likely to pick up the same hits in the other stations for both seeds. Both algorithms have methods of clone killing to encounter that problem considering the usage of the same hits in the muon stations M2 and M3 as a clone attribute. Of clone tracks the track candidate of which the hit in M5 is closer to a straight line extrapolation through the hits in M2 and M3 is kept.

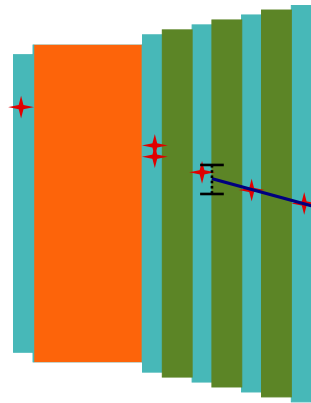
Muon Track Segments for Efficiency Studies

The calorimeter clusters used in the previous chapter only provide the position of a particle in the calorimeter and its energy. From muon track segments not only the position of a muon in the muon stations but the full 4-momentum and the charge can be obtained as follows.

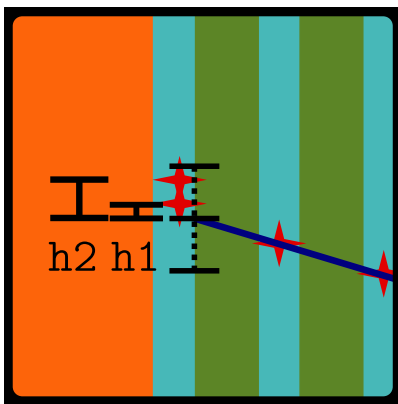
Using the assumption that the muons which were reconstructed as muon track segments were produced in or close to the primary vertex, the x position and the slope in the x - z plane already determine the curvature in the magnetic field and thereby the



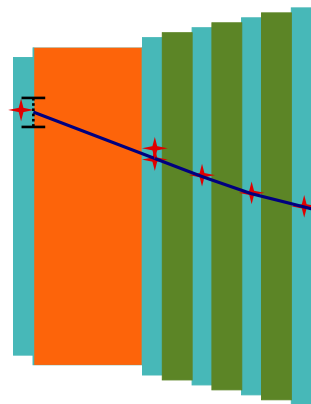
(a) In the first step no information on the slope is available, and a straight line towards the interaction region is assumed to define the search window.



(b) From the second step on the slope between the last two hits is used to predict the hit position in the next station.

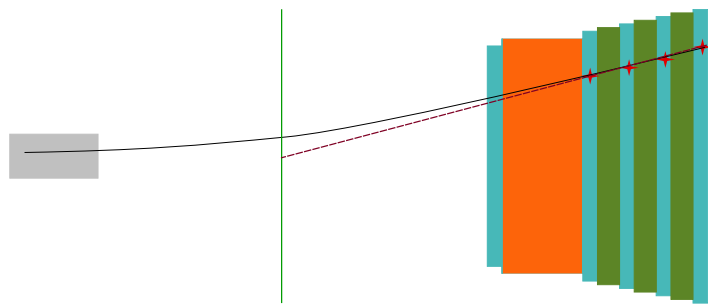


(c) If several hits are in the field of interest the one in better agreement with the extrapolation, i.e. the smaller distance h is taken.

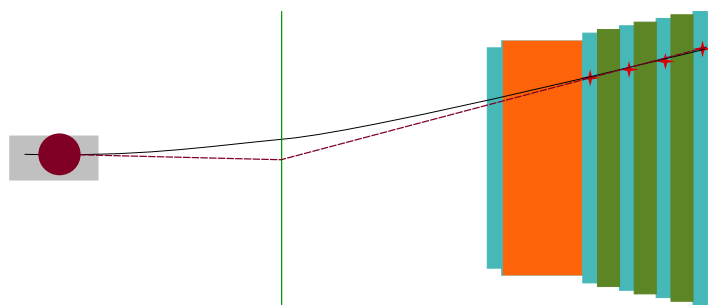


(d) The track reconstruction is completed once the last station is reached.

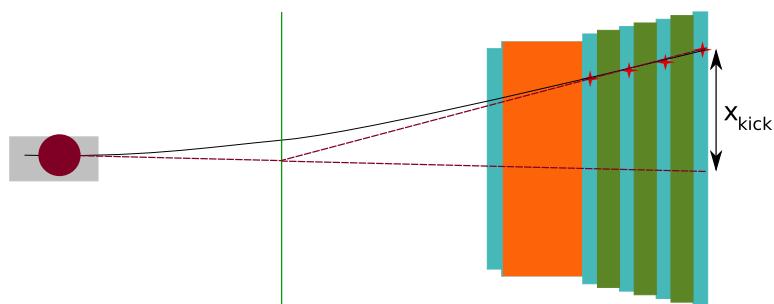
Figure 6.2: Steps of the track reconstruction algorithms in the muon stations. Hits in M5 serve as seeds. Once a hit is found, the search window in the next station is defined.



(a) The model of a bending plane determines half of the muon trajectory.



(b) Assuming the muon to originate from the interaction region the second half is determined.



(c) The kink, i.e. x_{kick} , then is a measure for the momentum.

Figure 6.3: Momentum estimation from hits only in the muon stations.

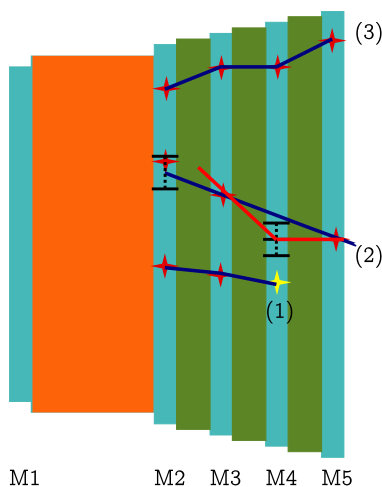


Figure 6.4: Track segments reconstructed with the tuned algorithm. Only the yellow hit is used for seeding in M4, because it is not used for any M5 seeded track segment. For track (2) the extrapolation to M2 is done using the hits in M3 and M5, as indicated by the dark blue line, instead of the prediction indicated by the red line which uses the position which was predicted for the search in M4.

momentum (see figure 6.3). With the momentum and position information, muon track segments could probe the efficiency of the entire tracking system, i.e. the efficiency to reconstruct a longtrack and not only the VELO or T station contribution. This powerful approach suffers from the low resolution of the muon chambers and multiple scattering in the calorimeters and in the muon absorbers. Therefore momenta cannot be determined precisely and the extrapolation to a decay vertex does not provide any information on the vertex quality. It has been shown that muon track segments alone cannot be used in a tag and probe method ([dC10d; dC10c]).

Improvements

Both tracking algorithms have the strict requirement that a hit is needed in each station which is used in the reconstruction of the track segment. From table 8.1 an improvement of the efficiency of at least 2 % is expected by replacing this restriction with a more flexible requirement and by demanding hits in a minimum number of stations. I.e. a station may only be skipped if no hit is within the search window.

To optimise the muon track segment reconstruction, changes have been applied to `HltMuonRec`. The seeding of muon tracks remains mainly unchanged: In a first part of the muon track reconstruction all hits in M5 seed a track – in figure 6.4 for tracks (2) and (3). Hence tracks with hits in all stations as well as tracks with missing hits in the stations M2, M3, and M4 can be found. A track without a hit in M5 cannot be found that way. These are found using those hits in M4 as seeds which have not been used to reconstruct a track segment seeded from M5 – track (1) in figure 6.4.

In the intermediate steps hits are searched for in a search window in each station around the expected position in that station. If a hit is found, the hit position is used as a starting point for the extrapolation to the next station, as before. Otherwise the

initial expected position serves as a starting point, thereby the previous extrapolation is extended (not indicated in the figure). The minimum number of hits in the four muon stations M2-M5 is chosen to be three. Hence only one extended extrapolation per track is allowed for M5 seeded tracks and no extended extrapolation is allowed for M4 seeded tracks.

As indicated for track (2) in figure 6.4 the extrapolation is always done using the slope between the last two hits and not with respect to an intermediate expected position in a station without a hit.

Table 8.1 also shows the efficiency of the improved algorithm.

6.2 Velo-Muon Matching in Principle

The principle of matching Velo tracks to muon segments has already been developed by [Ste08]. More recent simulated events, from 2009 and 2010 in contrast to simulations from 2006, have been used for further development of the algorithm. Moreover the algorithm has been reimplemented and thereby integrated to the LHCb software framework¹. Details of the procedure have been examined and improved to make the matching more efficient, increase the accessible phase space and automatise the calibration.

For each of the reconstructed tracks in the muon stations the Velo track from the same particle is searched to make Velo-Muon probes. Again the assumption of a bending plane is used to find the best Velo track. Both Velo tracks and muon track segments are extrapolated linearly to the magnetic plane and the distance d_x in x direction is determined. Due to the negligible curvature in the y - z plane the distance d_y in y direction can be calculated at any z position which was done using the hit in the second muon station.

A Velo track was then supposed to be better than another one if both d_x and d_y were smaller. Requiring two criteria to be fulfilled makes the decision depending on the order in which the Velo tracks are considered. As a remedy a combined distance has been introduced (see below).

The momentum of Velo-Muon probes is estimated using the same x -kick method as in the Velo-Calo tracking but in a second step a Kalman fit has been introduced to further improve the measurement because the track quality estimate and momentum estimate thereby use the full information of the measured magnetic field instead of the simplified model of a bending plane. Moreover the material interaction is more accurately taken into account than in a simple χ^2 fit².

Muon track segments were in the original version of Velo-Muon matching reconstructed by `HltMuonRec` which is changed to the improved `HltMuonRec`.

6.3 Further Improvements in Velo-Muon Tracking

The two most obvious methods to fit the hits in the muon stations for the extrapolation are a straight line through the two hits closest to the interaction region on the one hand and a minimum χ^2 fit of all the hits on the other hand. The latter provides a

¹The integration is especially important as the program has to be run in the production of stripping streams.

²For Velo-Calo probes this is not possible due to the coarse resolution of the calorimeter. The calorimeter cluster will be treated as an outlier in the Kalman fit and thus ignored for the momentum determination.

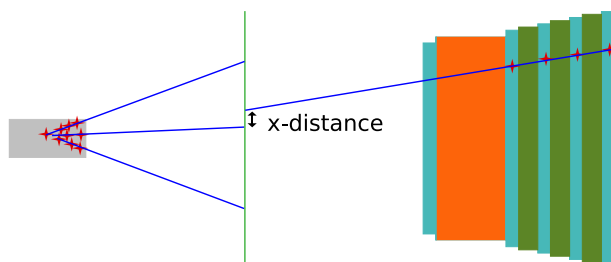


Figure 6.5: Muon tracks and Velo tracks are extrapolated linearly to the bending plane of the LHCb magnet.

longer lever arm to measure the slope but does not treat the material interaction in the muon absorbers correctly. The hits in M2 and M3 are less influenced by multiple scattering. Hence the former method treats material interaction more adequate. The χ^2 fit is modified to give a higher weight to the stations less affected by the multiple scattering by modifying the error estimates of the hits before they enter the calculation. The error estimates are obtained from the cell sizes via $\sigma_x = a_x/\sqrt{12}$ where a_x is the size in x direction. The scaling factors s therefore not only depend on the station (the amount of traversed material depends on the station) but also on the region of the muon station (the granularity depends on the region).

A straight line is fitted to the hits which goes through the nominal interaction point in the y - z plane.

$$\begin{aligned}x(z) &= b + t_x z \\y(z) &= t_y z\end{aligned}$$

The χ^2 , which is minimised in the fit, includes the scaling factors as follows:

$$\begin{aligned}\chi^2 &= \sum_{\text{hits}} \frac{(x(z) - x_{\text{hit}})^2}{\sigma_{x,\text{hit}}^2} + \frac{(y(z) - y_{\text{hit}})^2}{\sigma_{y,\text{hit}}^2} \\&\rightarrow \sum_{\text{hits}} \frac{(x(z) - x_{\text{hit}})^2}{(s_{(\text{reg},\text{sta})} \cdot \sigma_{x,\text{hit}})^2} + \frac{(y(z) - y_{\text{hit}})^2}{(s_{(\text{reg},\text{sta})} \cdot \sigma_{y,\text{hit}})^2}\end{aligned}$$

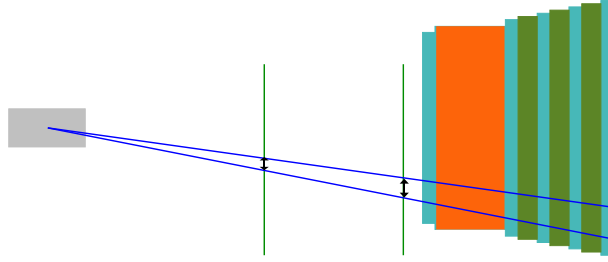
For four stations there are 16 factors $s_{(\text{reg},\text{sta})}$ but only 12 of them have to be determined because a common factor will only affect the absolute value of χ^2 but not the weights of the different hits. The factors have been determined using a simulation of $J/\psi \rightarrow \mu^+ \mu^-$ decays in the LHCb detector. For each set of parameters the percentage of correct matched Velo-Muon probes among all Velo-Muon probes has been evaluated and the set maximising it is given in table 6.1. Figures showing the dependency of the matching efficiency on the scaling factors can be found in appendix B.2.

Given that only 12 of the 16 degrees of freedom have a physical meaning, only the ratios $s_{\text{reg},\text{sta } 2}/s_{\text{reg},\text{sta } 3}$, $s_{\text{reg},\text{sta } 3}/s_{\text{reg},\text{sta } 4}$, and $s_{\text{reg},\text{sta } 4}/s_{\text{reg},\text{sta } 5}$ are calibrated for optimal Velo-Muon matching.

For fixed ratios the remaining overall scaling factors are determined by optimising the Velo-Muon matching efficiency for muon track segments from `MuonCombRec`. Since the ratios are fixed, the matching efficiency for muon track segments from `HltMuonRec` cannot decrease in this calibration for `MuonCombRec` – it only introduces compatibility to the muon track segments from the monitoring algorithm.

Table 6.1: Scaling parameters for the correction of multiple scattering in the muon absorbers.

parameter	station 2	station 3	station 4	station 5
$s_{\text{reg } 0}$	1.00	1.67	4.17	4.17
$s_{\text{reg } 1}$	1.19	3.80	8.33	4.76
$s_{\text{reg } 2}$	1.00	5.33	13.3	13.3
$s_{\text{reg } 3}$	1.04	3.13	4.17	3.13


 Figure 6.6: Increasing the distance of the plane in which the y distance between two tracks is determined. The distance between tracks in the y - z plane scales with the z position where the distance is determined.

As stated above, the original selection of the best Velo track can lead to ambiguous results. The ambiguity is removed by using a combined distance d which has to be minimised:

$$d = \sqrt{f \cdot d_x^2 + (1 - f) \cdot d_y^2}$$

The factor f is hereby used in such a way that both extremes, $d = d_x$ and $d = d_y$, can be set with $f = 0$ and $f = 1$ respectively.

The factor f corrects for different length scales in the combined x and y distance which are due to the different z positions of the x and y distance determination. That the scaling has to be adjusted arises from the intercept theorem as shown in figure 6.6. The factor f also takes into account that in the x extrapolation the low resolution muon track segment is extrapolated over a long distance, while in the y extrapolation the high resolution of the VELO is exploited for a long extrapolation towards the muon stations. Optimising f will therefore also give a higher weight to the y contribution than to the x contribution.

The determination of f must be done simultaneous with the optimisation of the z position of the y distance determination. In A.2 is analytically demonstrated that the uncertainty on d_y is minimised by calculating it at a z position between the VELO and the muon stations. The optimal position depends on the resolution of both subdetectors. The track segment with the better resolution has to be extrapolated over a larger distance than the track segment with the lower resolution, i.e. d_y has to be determined closer to the muon stations than to the VELO.

The corresponding dependency of the matching efficiency on both z positions and the scaling factor f is given in figure 6.7.

The final settings are to measure the distance in x at $z = 5800$ mm, the distance in y is measured at $z = 15000$ mm with $f = 0.06$. This does not mean, that the x measurement has hardly any influence on the calculated distance because the factor

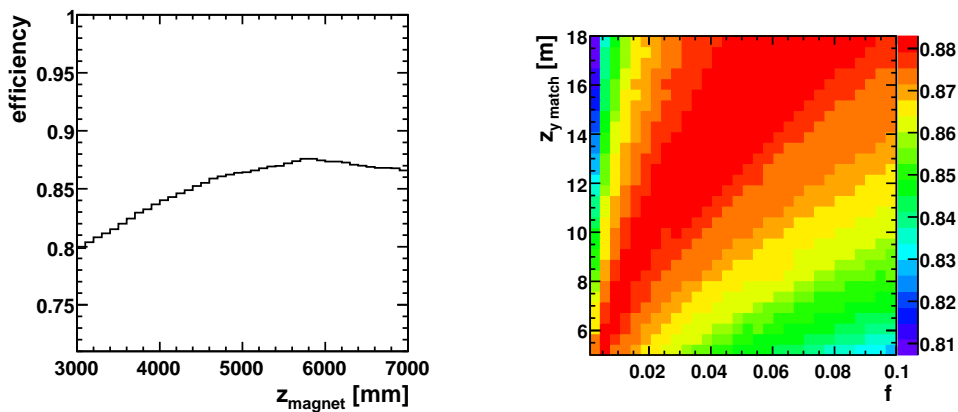
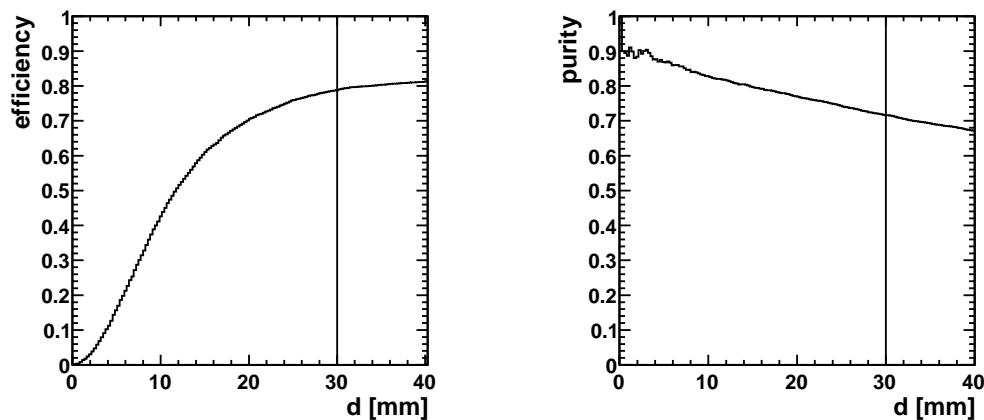


Figure 6.7: Dependency of the matching efficiency on the z position of the x distance calculation, z_{magnet} , left and on the z position of the y distance calculation and the scaling factor, f , right. In the latter case the efficiency is indicated by the colour.



(a) The fraction of Velo-Muon matches with a distance smaller than d among all muons reconstructed as Velo track and reconstructed as muon track.

(b) The fraction of correct matches among all matches with a distance smaller than d (i.e. the purity of the sample).

Figure 6.8: Performance of Velo-Muon matching as a function of the maximum distance d . For muon tracks in the innermost region of the muon stations. In figure B.3 the efficiency and the purity in the other regions of the muon stations are shown.

Table 6.2: Maximum distances used in the Velo-Muon matching and the corresponding efficiencies and purities. Determined on simulated events containing a $J/\psi \rightarrow \mu\mu$ decay with both muons in the detector acceptance.

region	maximum distance	efficiency	purity
0	30 mm	$78.8 \pm 0.6 \%$	$71.6 \pm 0.6 \%$
1	60 mm	$83.4 \pm 0.3 \%$	$72.3 \pm 0.3 \%$
2	110 mm	$79.1 \pm 0.3 \%$	$63.5 \pm 0.3 \%$
3	200 mm	$79.4 \pm 0.4 \%$	$72.6 \pm 0.4 \%$

enters in the quadratic addition. The different scales for x and y therefore differ by a factor $\sqrt{0.06} \approx 1/4$.

The fraction of ghosts among the Velo-Muon probes is reduced by rejecting those where d is too large. The efficiency for Velo-Muon matching

$$\varepsilon = \frac{\#\text{muon which are reconstructed as Velo-Muon probe}}{\#\text{muon which are reconstructible as Velo-Muon probe}}$$

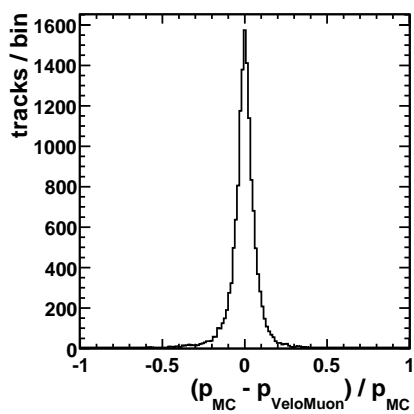
and the purity, defined as

$$\rho = \frac{\#\text{correct matched Velo-Muon probes}}{\#\text{Velo-Muon probes}},$$

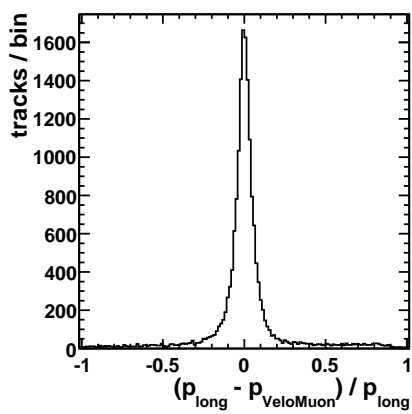
are functions of the maximum d as shown in figure 6.8. *Reconstructible as Velo-Muon probe* means that the muon has to be reconstructed as a Velo track and as a muon track segment. For each region of the muon stations a different d cut is chosen to take the different multiplicities and resolutions into account. The efficiency and purity for the different regions of the muon stations and the maximum d values are given in table 6.2.

Momentum Resolution

The momentum resolution shown in figure 6.9 for simulated events shows a good momentum resolution if one considers that there is no measurement behind the magnet which is not influenced by multiple scattering in the calorimeters. Compared to the resolution quoted by [Ste08] the usage of a full Kalman fit does not improve the momentum resolution.



(a) Velo-Muon momentum resolution compared to the simulated momentum.



(b) Velo-Muon momentum resolution compared to the longtrack reconstruction.

Figure 6.9: Resolution of Velo-Muon tracks for simulated events. Compared to the simulated momentum the mean of the relative difference is 0.015 ± 0.050 % and the RMS is 6.5 %. Compared to the longtrack reconstruction the mean is 0.031 ± 0.048 % and the RMS is 6.0 %.

Measurement of the Tracking Efficiency in the T Stations with $K_S \rightarrow \pi^+\pi^-$

So, und jetzt haben wir gelernt:
Bälle rollen bergab und Spindeln
rollen bergauf.

Karlheinz Meier

Pions which are found as Velo-Calo probes are used to determine the efficiency of the LHCb track reconstruction in the T stations. They are used in the tag and probe method to reconstruct the decay $K_S \rightarrow \pi^+\pi^-$ as shown in figure 7.1.

7.1 Selection of K_S Events

The K_S resonance has a short lifetime of 0.895×10^{-10} s. A separation of production vertex and decay vertex of the K_S is one of the main criteria to distinguish K_S decays from the background.

The selection criteria chosen for the tag and probe tracking efficiency measurement using Velo-Calo reconstructed K_S daughters are given in table 7.1. The individual quantities are explained in the following paragraphs.

$\chi^2/\text{ndof}(\text{longtrack})$ The track quality, χ^2/ndof , is the main tool to distinguish ghosts from “real” tracks.

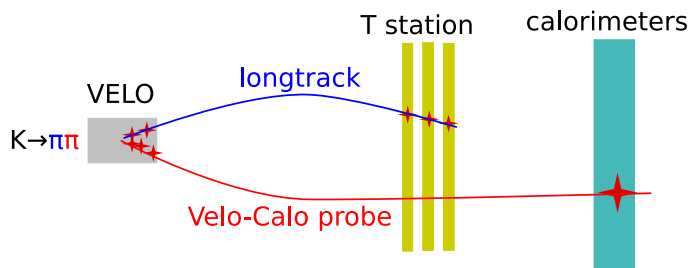


Figure 7.1: A K_S decay to be reconstructed for the efficiency measurement. For each decay it is tested if the probe is confirmed.

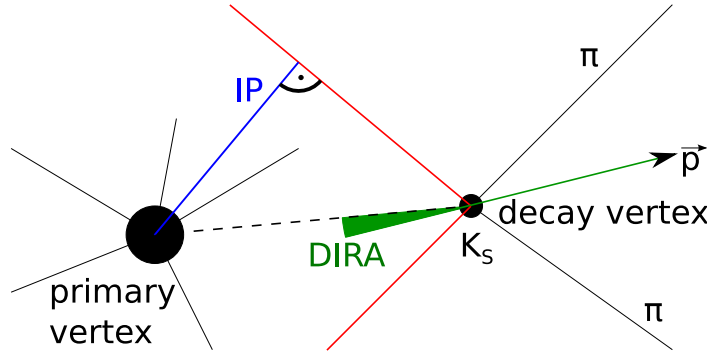


Figure 7.2: Illustration of direction angle and impact parameter in case of a K_S decay. Other particles produced in the primary interaction are indicated. The extrapolation of a pion tracks beyond the decay vertex are shown in red, the straight line from the decay vertex to the primary vertex is dashed, the direction angle and the K_S momentum are green, and the pions impact parameter blue.

Table 7.1: Selection criteria for K_S decays.

variable	value
χ^2/ndof (longtrack)	< 5
distance of closest approach	< 1 mm
$\cos(\text{direction angle})$	> 0.99995
χ^2/ndof (K_S decay vertex)	< 5
z (K_S decay vertex)	> 150 mm
π impact parameter (w.r.t. primary vertex)	> 1.5 mm

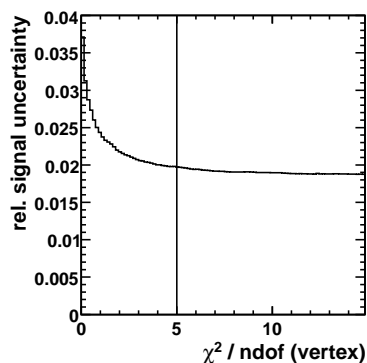
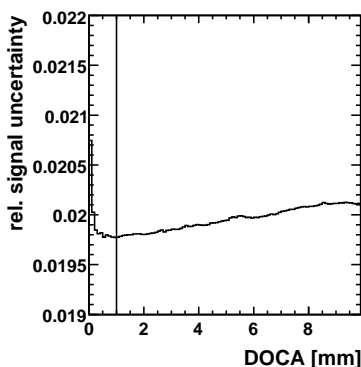
The current recommendation of the LHCb tracking group is to use tracks with $\chi^2/\text{ndof} < 5$.

Distance of closest approach (DOCA) Velo tracks are straight lines which do not need to intersect in three dimensional space. The minimum distance between two tracks is called the distance of closest approach. For particles coming from the same vertex, tracks would ideally meet in the vertex and have a vanishing DOCA. The DOCA is highly correlated to the vertex χ^2/ndof but faster to compute, the general recommendation therefore is to only compute χ^2/ndof if the distance of closest approach is small.

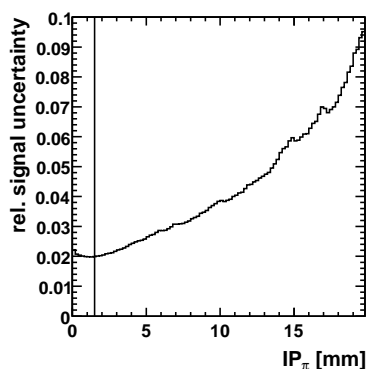
Direction angle (DIRA) Knowing both, the position of the decay vertex and the momentum of the K_S the trajectory of the K_S , can be reconstructed. The angle between that trajectory and a straight line between the primary vertex and the decay vertex is called *direction angle*.

Most K_S are produced at the primary vertex and fly straight till they decay. Ideally the cosine of the DIRA is therefore 1.

In principle also the impact parameter of the reconstructed K_S with respect to the primary vertex could be used but the DIRA resolution is independent of the flight


 (a) Variation of the maximum $\chi^2/\text{ndof}(\text{vertex})$.


(b) Variation of the maximum DOCA.



(c) Variation of the minimum pion impact parameter.

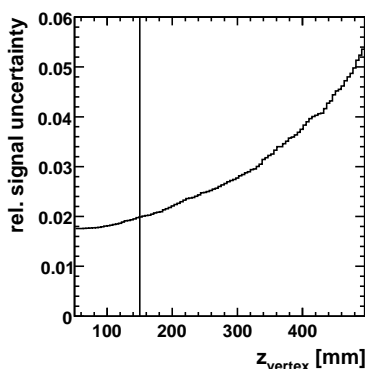

 (d) Variation of the minimum z position of the K_S decay vertex.

Figure 7.3: Relative signal uncertainty for the different cuts. In each figure one cut is changed (abscissa) while the others are set to the values from table 7.1.

distance while the impact parameter resolution scales with the flight distance.

$\chi^2/\text{ndof}(\text{vertex})$ Whether the pion tracks meet in a common vertex is expressed in the goodness of the vertex fit. A large χ^2/ndof indicates that the pions were not produced in the same interaction.

$z(\text{vertex})$ The z coordinate of the position of the K_S decay vertex in the LHCb coordinate system is chosen such that most of the primary interactions and therefore possible track combinations are excluded from the analysis.

Impact parameter Whereas the K_S is required to have a trajectory coming from the primary vertex, the K_S decay products are required not to come from there. In contrast to the K_S those pions can be extrapolated back using only VELO information.

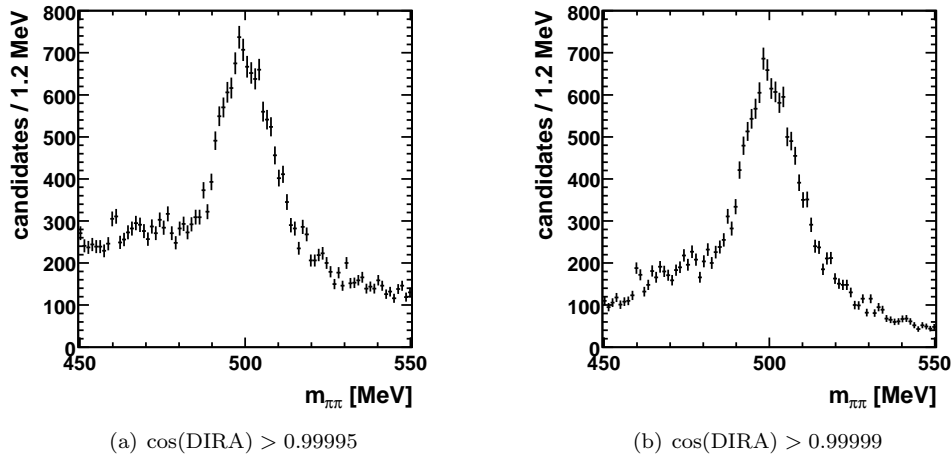


Figure 7.4: Invariant mass spectrum for different cuts on the direction angle. The background spectrum has a maximum under the K_S peak for the hard cut. A fit of the number of K_S decays cannot be trusted in the latter case.

A minimum impact parameter of the pions with respect to the primary vertex ensures that these are decay products from a long lived particle.

The cuts were optimised on data with respect to the relative signal uncertainty $\sigma(N_{K_S})/N_{K_S}$. The dependence of the signal uncertainty on the cut variables is shown in figure 7.3. The cut on the direction angle is shown in figure B.4. The dependency of the relative signal uncertainty on the direction angle cut cannot be used for the optimisation of the selection because a harder cut on the direction angle influences the background spectrum such that the background has a peak at the K_S mass which can be seen in figure 7.4.

For further illustrate the effect of the cuts, in figure 7.5 the number of successfully reconstructed K_S with a certain direction angle are shown for simulated data. The number of wrong reconstructed K_S decays (i.e. background to the analysis) is also shown and the chosen cut is indicated.

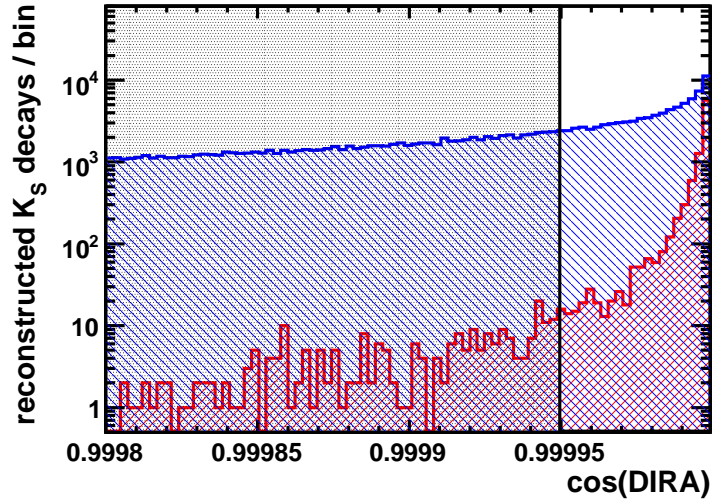
For the other cut variables, the corresponding figures for simulated data are in appendix B.3.

7.2 Phase Space Coverage

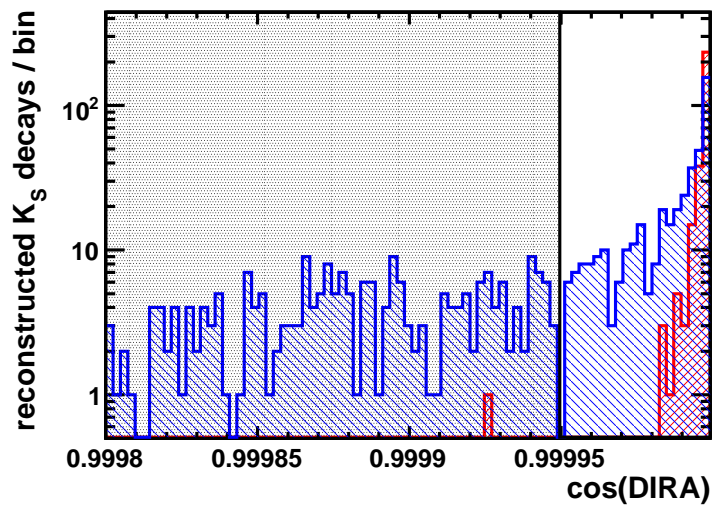
Any results obtained with the tag and probe method will quantify the tracking performance in the phase space covered by Velo-Calo probes from K_S decays. It is therefore important that the covered phase space is large and that it is known which part of the phase space is covered by the method.

For simulated events the distribution of Velo-Calo probes from K_S decays is illustrated in figure 7.6.

The different acceptances are due the fact that the VELO cannot be completely closed at the low energy. This reduces the maximum pseudo rapidity to 4, larger values still occur if the decaying K_S is produced at small pseudo rapidity and then decays

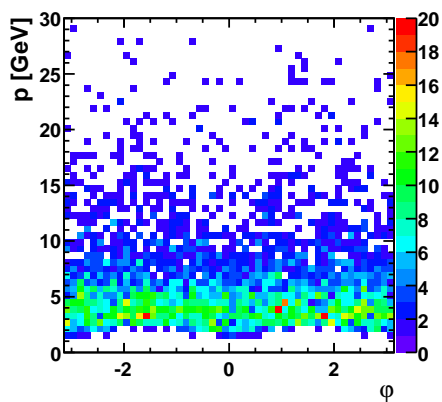


(a) DIRA cut without other cuts.

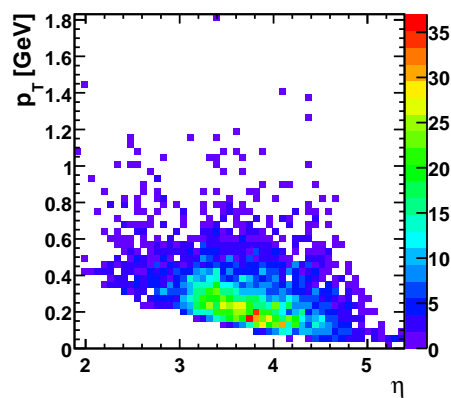


(b) DIRA cut with all other cuts applied (n minus 1).

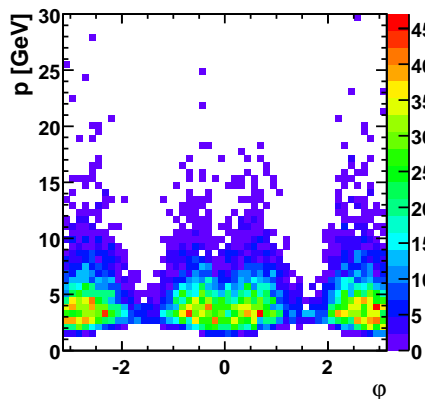
Figure 7.5: Number of correct reconstructed K_S decays (red) and background contribution as a function of $\cos(\text{DIRA})$.



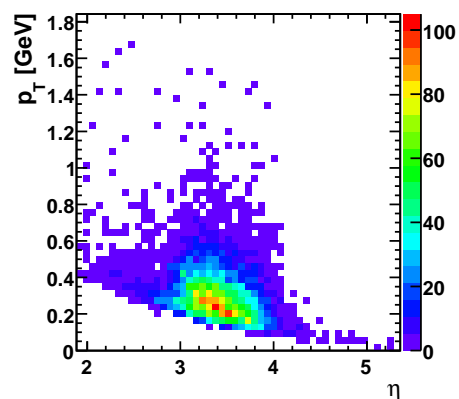
(a) Coverage in momentum and azimuthal angle in the VELO with a closed VELO.



(b) Coverage in transverse momentum and pseudo-rapidity with a closed VELO.



(c) Coverage in momentum and azimuthal angle in the VELO with an opened VELO.



(d) Coverage in transverse momentum and pseudo-rapidity with an opened VELO.

Figure 7.6: The phase space covered by correct reconstructed Velo-Calorimetry probes from K_S decays in simulated events. 7.6(a) and 7.6(b) for $\sqrt{s} = 7$ TeV, 7.6(c) and 7.6(d) for $\sqrt{s} = 900$ GeV. At $\sqrt{s} = 900$ GeV the VELO is opened by 30 mm.

inside one of the VELO halves. The gaps in the VELO can also be seen in the φ distribution.

The phase space coverage in data is shown in figure 7.7. As it cannot be said for a single probe in data if it is correctly reconstructed, the number of reconstructed K_S decays with a Velo-Calorimetry probe in a certain phase space region is determined from the corresponding invariant mass histogram in each bin of figure 7.7.

Given that every data point in figure 7.7 requires the fit of a mass histogram, which needs sufficient statistics and which needs to be checked individually, a coarser resolution than in figure 7.6 has been chosen. The measurement does not reveal any range in the phase space which is simulated to be accessible but is not covered in data.

With Velo-Calorimetry probes the reconstruction of charged particles can be measured in

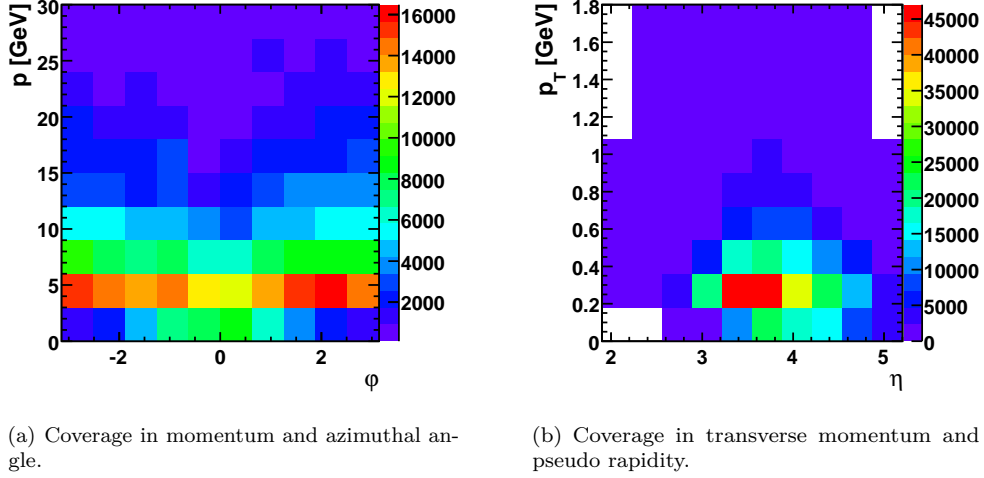


Figure 7.7: Phase space coverage of Velo-Calo reconstructed K_S daughters. The colour indicates the number of K_S with the Velo-Calo reconstructed pion in the corresponding phase space region. White indicates that the number of reconstructed K_S is within 1σ compatible with 0.

the whole φ range, if the VELO is closed. In η as well the whole detector acceptance is covered while probes with transverse momenta > 0.6 GeV or momenta > 15 GeV are rare.

7.3 Measured Efficiencies

Estimation of the K_S yield

The invariant mass spectra of the selected K_S candidates with and without requiring the Velo-Calo probe to be confirmed are used to determine the tracking efficiency in the T stations. For both cases the number of K_S decays in the signal peak is determined by fitting the following model to the spectra.

The fit function comprising a double Gaussian describing the signal

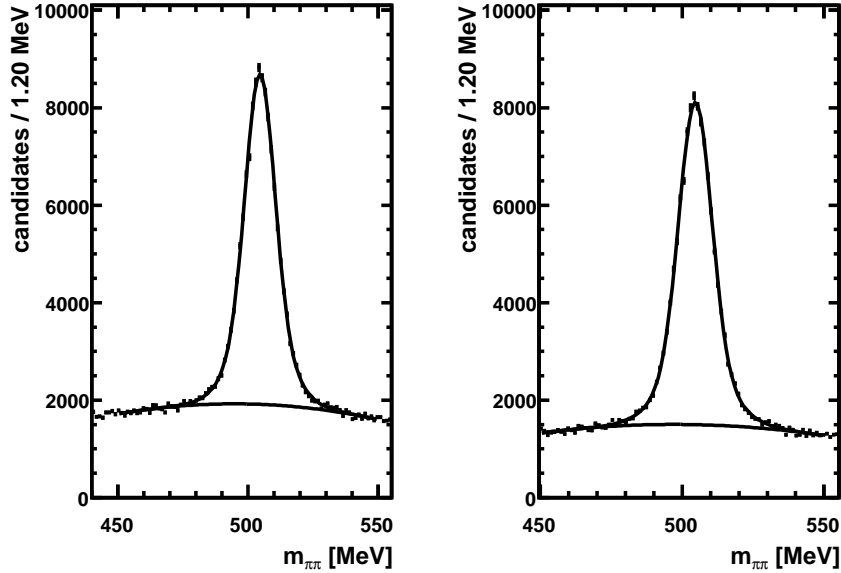
$$p_s(m_{\pi\pi}) = N_{K_S} \cdot \left(\frac{1-f_b}{\sigma\sqrt{2\pi}} \cdot \exp\left(-\frac{1}{2} \frac{(m_{\pi\pi} - m_{K_S})^2}{\sigma^2}\right) + \frac{f_b}{w\sigma\sqrt{2\pi}} \cdot \exp\left(-\frac{1}{2} \frac{(m_{\pi\pi} - m_{K_S})^2}{w^2\sigma^2}\right) \right)$$

and a second order polynomial for the background

$$p_b(m_{\pi\pi}) = a + bm_{\pi\pi} + cm_{\pi\pi}^2$$

where $m_{\pi\pi}$ is the measured invariant mass and m_{K_S} the fit parameter for the K_S mass (possibly different from the value in [Nak10]).

The parameter of interest is N_{K_S} which is determined for both types, invariant mass spectra of a probe track and a longtrack on the one hand and invariant mass spectra of



(a) Invariant mass histograms and fits.

(b) Fit result for all probes.

parameter	value
N_{K_S}	494830 ± 650
m_{K_S}	504.6 ± 0.0 MeV
σ	5.63 ± 0.09 MeV
f_b	0.31 ± 0.2
w	2.0 ± 0.7
a	-17190 ± 1680
b	77.5 ± 6.8 MeV ⁻¹
c	-0.0788 ± 0.0068 MeV ⁻²

(c) Fit result for confirmed probes.

parameter	value
N_{K_S}	493290 ± 610
m_{K_S}	504.6 ± 0.0 MeV
σ	5.62 ± 0.08 MeV
f_b	0.32 ± 0.2
w	2.0 ± 0.1
a	-14530 ± 1530
b	64.8 ± 6.2 MeV ⁻¹
c	-0.0653 ± 0.0062 MeV ⁻²

Figure 7.8: For illustration of the method. The invariant mass spectra are fitted to estimate the number of reconstructed K_S decays. The spectrum on the left shows the distribution of Velo-Calo probes combined with longtracks, while one the right side the Velo-Calo probes are required to be confirmed. The size of the data points includes statistical error bars. The ratio of the signal K_S decays is the tracking efficiency.

Table 7.2: Measured tracking efficiencies for collisions at $\sqrt{s} = 900$ GeV in 2009 for the longtrack reconstruction.

algorithm	$\epsilon(\text{data})$	$\epsilon(\text{simulation})$	$\epsilon(\text{mod. simulation})$
forward tracks	$93.4 \pm 2.4 \%$	$95.3 \pm 1.0 \%$	$94.1 \pm 1.1 \%$
match tracks	$86.1 \pm 2.6 \%$	$92.1 \pm 1.2 \%$	$88.8 \pm 1.3 \%$
all longtracks	$93.5 \pm 2.1 \%$	$96.4 \pm 1.0 \%$	$95.7 \pm 1.0 \%$

a *confirmed* probe track and a longtrack on the other hand. The error estimate from the fit routine is used for the error estimation of the calculated efficiency. The errors given in the following tables and figures are calculated as explained in section 10.2 and are not proportional to $1/\sqrt{N_{K_S}}$.

Collisions at $\sqrt{s} = 900$ GeV

In 2009 most of the LHC collisions were produced at a centre of mass energy of 900 GeV – which is the energy at which protons collide without acceleration after the injection from the SPS (see figure 2.1).

As stated in section 3.1 the tracking efficiency directly enters in measurements of cross sections. For the determination of the K_S production cross section [HMHK⁺10] it has been determined using simulated K_S decays but for the uncertainty estimation the measurement in this work has been used. The tag and probe method has been applied to both data and simulation and the difference is treated as an uncertainty on the simulated value.

In addition to the official simulation data provided by the LHCb simulation group a modified one has been used and the same two data sets will be used in this study.

The modified simulation was introduced because it was found that tracks reconstructed in the simulation used in average more hits than in data.

Before the track finding was performed on the simulated data set, hits in the detector were randomly removed such that after the reconstruction, the number of hits per track had the same distribution in the simulation as on data.¹

The results from table 7.2 show that the track matching algorithm is more sensitive to the removal of hits. Moreover, after the modification the simulation is in agreement with the measured result. The remaining difference was considered as systematic uncertainty.

Moreover, table 7.2 shows the known fact, that using both algorithms, track matching and forward tracking, increases the efficiency to reconstruct a longtrack only slightly with respect to using only the forward tracking algorithm.

Collisions at $\sqrt{s} = 7$ TeV

The large integrated luminosity collected at $\sqrt{s} = 7$ TeV allows to measure the tracking efficiency not only as a single number but also as a function of different kinematic quantities of the particle.

¹On data these hits are missing on the tracks for several reasons. The most obvious reason might be a wrong simulated hit efficiency of the detector. Another, more important reason is misalignment due to which hits are not found by the pattern recognition. Removing the hits completely from the detector in the simulation therefore has the same effect for the track reconstruction.

Investigated are:

- momentum p
- transverse momentum p_T
- pseudo rapidity η
- azimuthal angle φ .

Figures 7.9 through 7.12 show the efficiency of the longtrack reconstruction as a function of these four variables. Figure (a) in each figure shows the efficiency of the combined longtrack reconstruction (from track matching and forward tracking) for all particles. For negative charged particles figure (b) shows the combined longtrack reconstruction efficiency while in figure (c) only positive charged particles are considered. The contribution of the individual algorithms, forward tracking and track matching, is shown in figures (d) and (e) respectively.

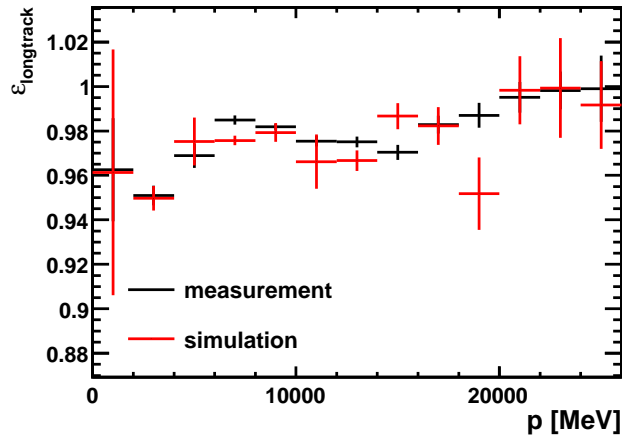
Momentum Dependence Figure 7.9 shows the tracking efficiency contribution from the T stations as a function of the particle momentum. Very low momentum particles hardly reach the T stations due to the magnetic field which leads to large statistical errors on the first momentum bin. Tracks are generally easier to reconstruct if their curvature is small. This effect can be seen in the range up to 8 GeV in all figures, for track matching even up to 20 GeV. The discrepancy between data and simulation is larger for track matching than for forward tracking. The combined tracking efficiency is hardly affected.

Transverse Momentum Dependence Figure 7.10 shows the tracking efficiency as a function of the transverse particle momentum. Data points up to $p_T \lesssim 800$ MeV can be trusted, the range beyond is shown for illustration of results from too small data sets. The simulated sample corresponds to a smaller integrated luminosity (3 nb^{-1}) than the actual data sample (14 nb^{-1}). Therefore in the range beyond 1 GeV the method provides no result for the simulation where the fits are still stable for data.

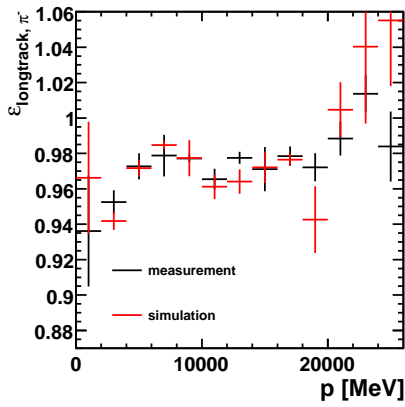
The dependency of the tracking efficiency on the transverse momentum is in good agreement between data and simulation in the range of valid results. The limit of 800 MeV can either be increased by increasing the data sets or by using a different two body decay.

Pseudo Rapidity Dependence In contrast to the momentum, there is no obvious reason why the tracking efficiency should depend on the pseudo rapidity. Figure 7.11 ensures that the tracking efficiency is constant over a large range. Below 2.5 only a small number of K_S decay products could be reconstructed, the deviation from a constant efficiency in that range is no indication for a problem in that range. For pseudo rapidities larger than 4.5, the efficiency is significantly smaller than below 4.5. This effect can be explained by the detector geometry. In the middle of the T stations where the beam pipe is situated, particles cannot be detected..

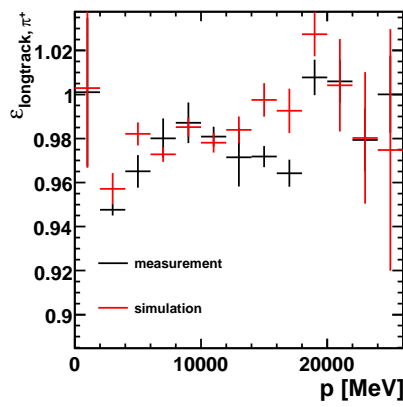
Azimuthal Angle Dependence The effect of the beam pipe can be seen in figure 7.12. For negative charged particles the tracking efficiency is small at $\varphi \approx 0$ and for positive charged particles the same effect can be seen at $\varphi \approx \pm\pi$. These are particles of which trajectories are curved towards the beam pipe in the magnetic field. They



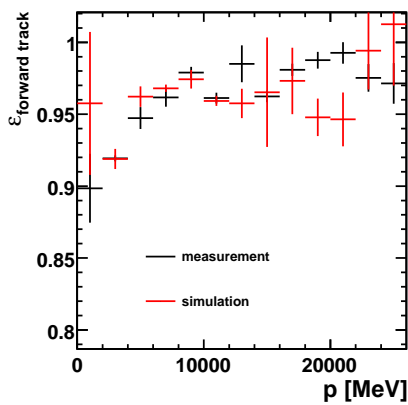
(a) Efficiency for both charges.



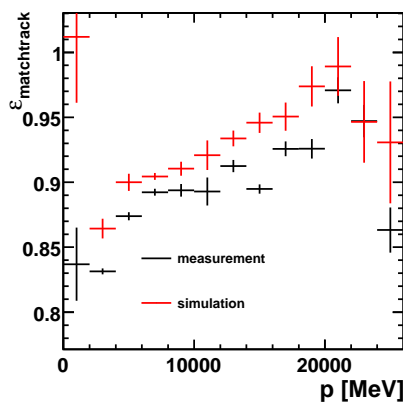
(b) Efficiency for negative charged pions.



(c) Efficiency for positive charged pions.



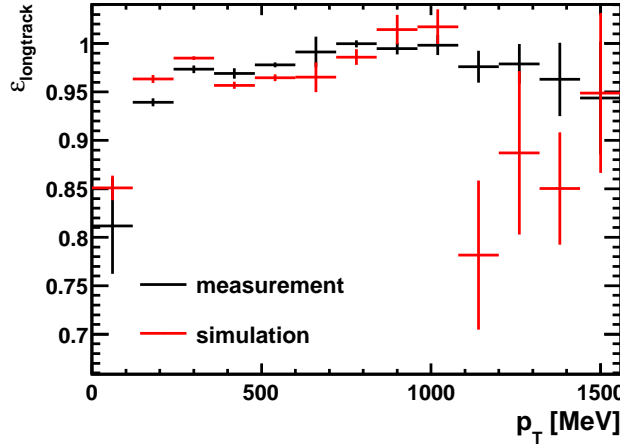
(d) Efficiency for forward tracking.



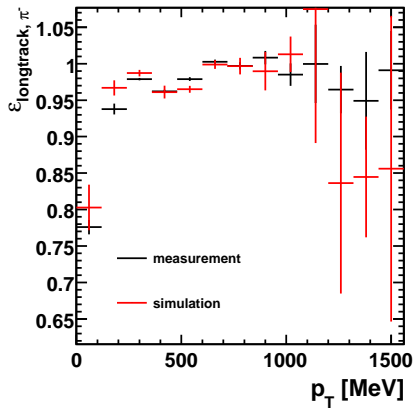
(e) Efficiency for track matching.

Figure 7.9: Tracking efficiencies of longtracks as a function of the momentum p .

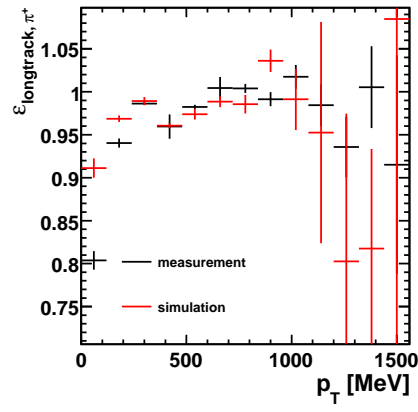
7. MEASUREMENT OF THE TRACKING EFFICIENCY IN THE T STATIONS WITH $K_S \rightarrow \pi^+\pi^-$



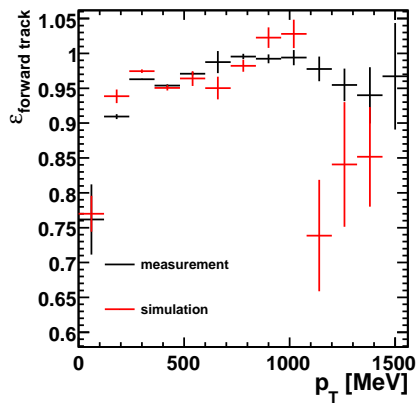
(a) Efficiency for both charges.



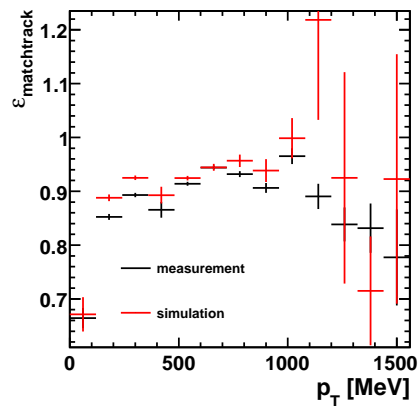
(b) Efficiency for negative charged pions.



(c) Efficiency for positive charged pions.

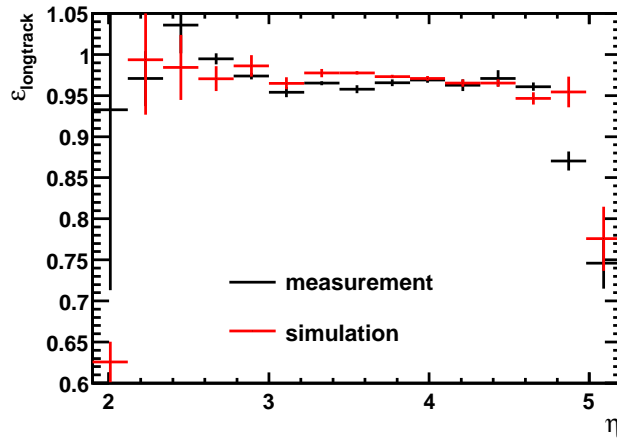


(d) Efficiency for forward tracking.

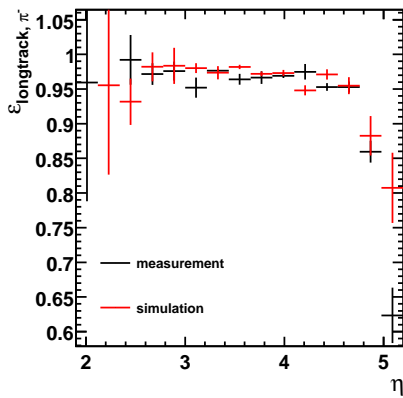


(e) Efficiency for track matching.

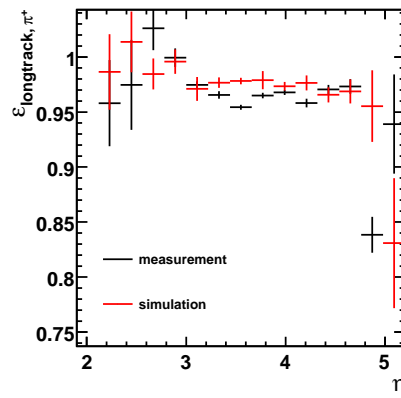
Figure 7.10: Tracking efficiencies of longtracks as a function of the transverse momentum p_T . Beyond 1 GeV statistics is small which led to divergent fits.



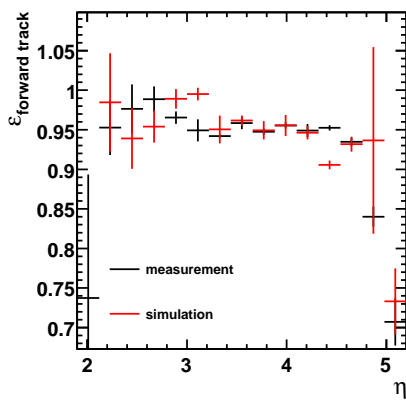
(a) Efficiency for both charges.



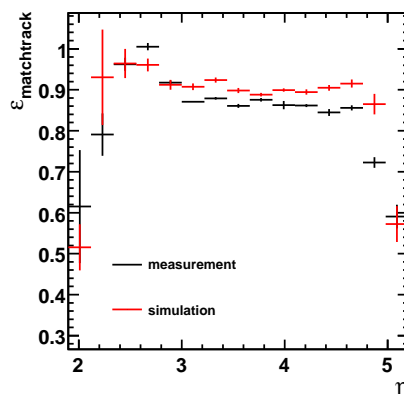
(b) Efficiency for negative charged pions.



(c) Efficiency for positive charged pions.



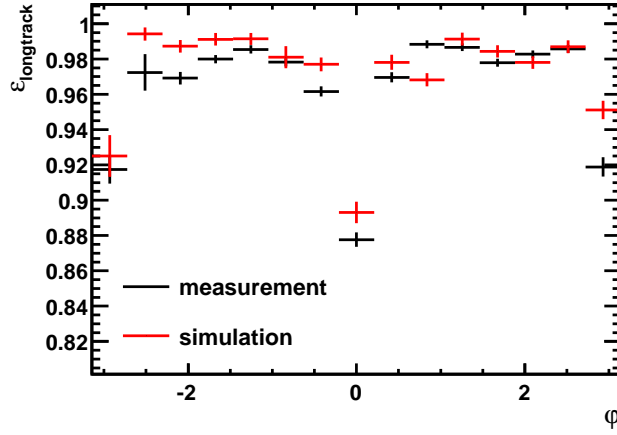
(d) Efficiency for forward tracking.



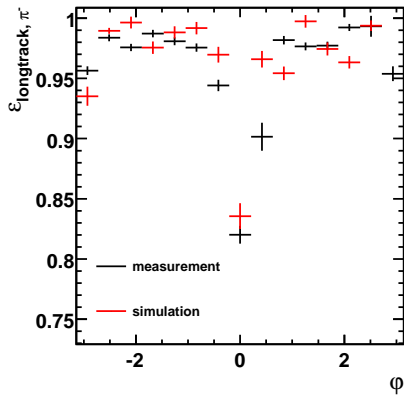
(e) Efficiency for track matching.

Figure 7.11: Tracking efficiencies of longtracks as a function of the pseudo-rapidity η .

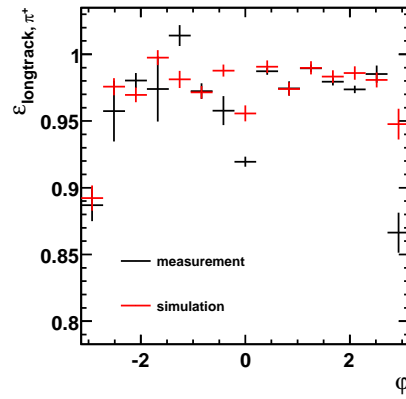
7. MEASUREMENT OF THE TRACKING EFFICIENCY IN THE T STATIONS WITH $K_S \rightarrow \pi^+\pi^-$



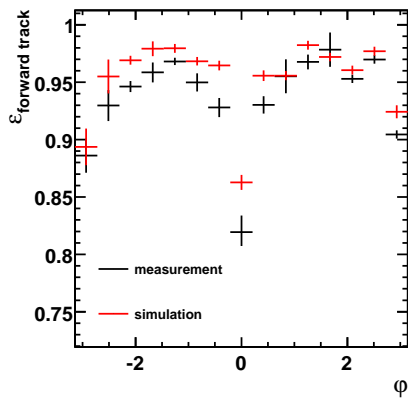
(a) Efficiency for both charges.



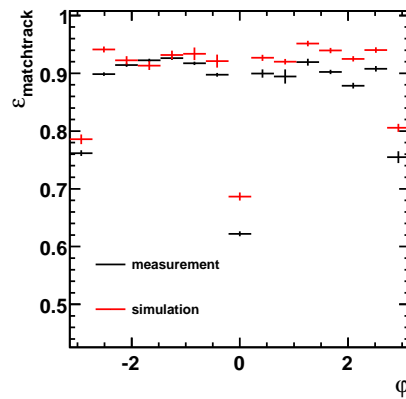
(b) Efficiency for negative charged pions.



(c) Efficiency for positive charged pions.



(d) Efficiency for forward tracking.



(e) Efficiency for track matching.

Figure 7.12: Tracking efficiencies of longtracks as a function of the azimuthal angle φ . The low efficiencies for $\varphi = \pm\pi$ and $\varphi = 0$ are an effect of the detector geometry.

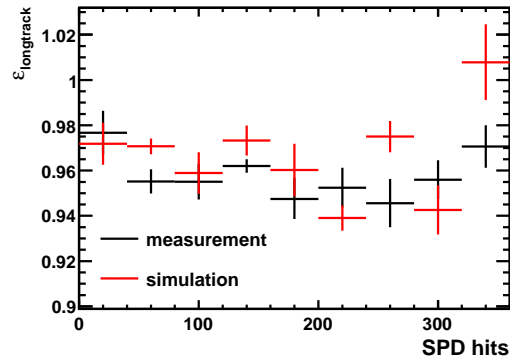


Figure 7.13: Tracking efficiencies of longtracks as a function of the SPD multiplicity.

may pass the beam pipe in the T stations and leave the beam pipe before reaching the calorimeters.

Recent improvements of the track reconstruction in the T stations take a possible transition of the beam pipe into account and increased the efficiency in the inner region of the T stations. [Sch10]

Moreover one might fear that the tracking algorithms show significant performance loss for high multiplicity. In figure 7.13 the tracking efficiency as a function of the number of hits in the SPD is shown². The results are in agreement with a constant efficiency.

The probability to reconstruct a charged particle trajectory in the T stations can be a function of the detector module which is traversed. If a certain module is wanted, particles going through that module have a lower chance to be reconstructed. From hit efficiency measurements, individual module performances are known and considered in the simulation, therefore no significant deviation is expected.

The results in figure 7.14 show that the distance of particles from the beam axis increases with increased distance from the interaction point – no Velo-Calo probe passes the outer three modules in station 1 while only one module at the outer ends of station 3 is not passed. Given that each probe passes all stations, statistical fluctuations can be distinguished from real effects.

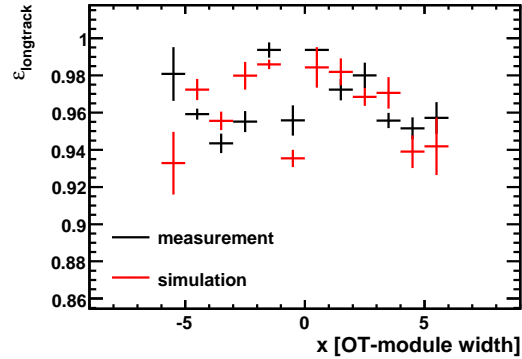
As illustrated in figure 7.15 a want module can be seen in the adjacent stations. As no such effect can be seen, no region in the T stations except the aforementioned beam pipe traversal is identified to cause problems to the track reconstruction.

Further observed effects

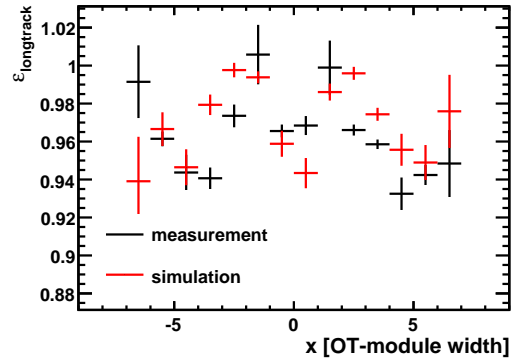
Figure 7.16 reveals that the K_S mass (497.61 MeV) is not correctly reconstructed for large pseudo rapidities of the Velo-Calo probe. As in the standard reconstruction no such effect has been observed, it is assumed that this is an effect of the momentum estimation in the Velo-Calo reconstruction. As however, the method does not rely on a precise momentum estimation no correction for that effect is needed.

²The number of hits in the SPD is a found to be an appropriate measure for multiplicity effects in T station track reconstruction. [Mei10]

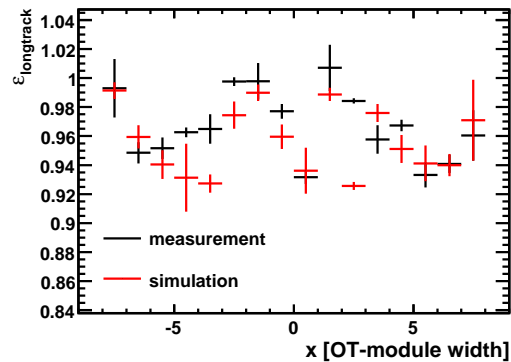
7. MEASUREMENT OF THE TRACKING EFFICIENCY IN THE T STATIONS WITH $K_S \rightarrow \pi^+\pi^-$



(a) Station 1



(b) Station 2



(c) Station 3

Figure 7.14: Tracking efficiencies of longtracks as a function of the x position of the T station traverse. As length scale the width of an OT module has been chosen – each data point therefore represents an OT module while the four innermost data points also include tracks passing through the IT.

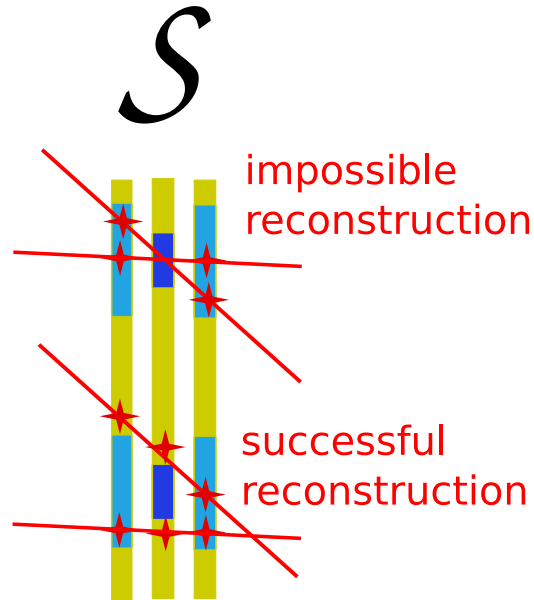
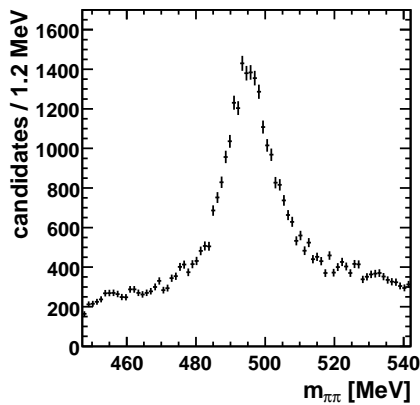
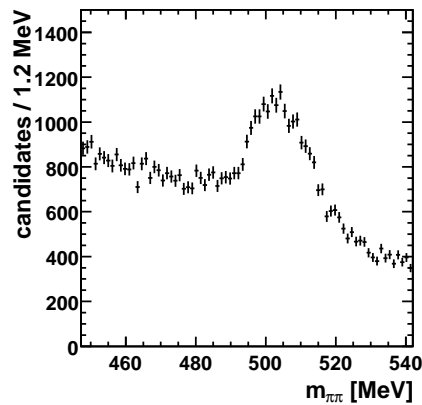


Figure 7.15: A want module has an effect on the measured efficiency if an adjacent station is investigated. That no hit is found in the middle station makes the reconstruction of some particles traversing the light blue modules impossible. Still probes passing the light blue modules can be reconstructed if they do not pass the want module.



(a) $2.56 < \eta < 2.78$



(b) $4.54 < \eta < 4.76$

Figure 7.16: Invariant mass spectrum for different η ranges of the probe track. A different slope of the background spectrum as well as a shifted K_S mass can be seen.

Summary

The track weighted average efficiencies are the following.

$$\begin{aligned}\varepsilon_{\text{simulation}} &= 96.2 \pm 0.4 \% \\ \varepsilon_{\text{measurement}} &= 95.5 \pm 0.3 \%\end{aligned}$$

The difference between data and the simulation, $0.7 \pm 0.5 \%$, is treated as the T station contribution to the systematic uncertainty of the tracking efficiencies. The VELO contribution has been determined by [Wan10b] also at the K_S resonance and is $1.6 \pm 0.5 \%$.

Particles which cannot be detected in the T stations due to a traversal of the beam pipe in the T stations can be reconstructed as Velo-Calo probes. Therefore the measured efficiency is smaller for particles which pass the beam pipe than for other particles.

For the track matching algorithm, the difference between simulation and measurement is larger than for forward tracking. For collisions at $\sqrt{s} = 900$ GeV in 2009 this was an effect of a different effective hit efficiency. A modification of the simulations, similar to those at $\sqrt{s} = 900$ GeV is investigated and results are expected soon [Sch].

In the low momentum range the efficiencies are lower than in average. This effect is due to the property of track reconstruction algorithms to favour the reconstruction of high momentum ghosts over low momentum tracks.

In the high p_T range the simulated results are not reliable while the measurement still provides results. The reason is that the integrated luminosity analysed is larger than the luminosity corresponding to the simulation. A larger simulated data sample however is not available and has not been created because the high p_T region is supposed to be investigated with the Velo-Muon method.

Confirmation with T Tracks and Downstream Tracks

For the confirmation of Velo-Calo probes with T tracks or Downstream tracks problems can arise if the occupancy in the T stations around a Velo-Calo track is not simulated correctly. If the probe traverses a high occupied region in the T stations it is likely to use the track from a different particle for the confirmation.

Figure 7.17 shows the number of reconstructed K_S decays as a function of the T station hits in a 10 cm search window around the Velo-Calo probe. As the probability to find a T track or downstream track in that search window is highly correlated to the number of hits, the distributions for data and simulation have to be the same to obtain reliable results. The distribution for simulated events is adjusted reweighting the events according to the number of T station hits around the Velo-Calo probe such that the distributions are the same.

Figure 7.18 shows the weights which are given to events of different occupancy around a Velo-Calo probe. After applying these weights the efficiency for downstream track reconstruction and T track reconstruction can be measured, which is shown in figure 7.19.

As for longtracks, the measured efficiencies are slightly lower than in the simulation, but no problem can be assigned to either algorithm in any phase space region.

7.4 Background from Wrong Confirmations

In section 5.4, the possibility to confirm a Velo-Calo ghost with a correct reconstructed longtrack has been discussed. In the tag and probe method however no problem

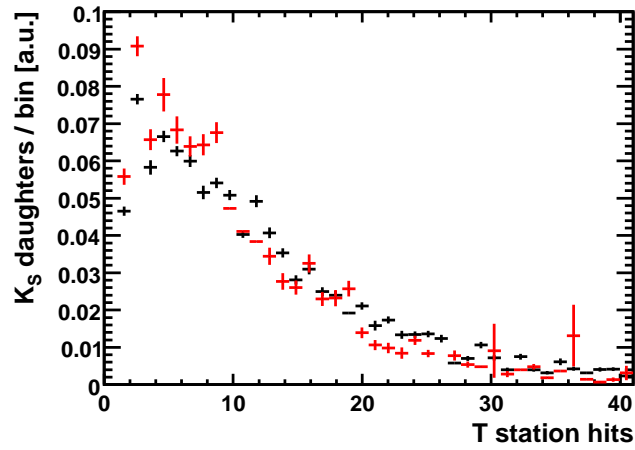


Figure 7.17: Normalised number of Velo-Calo reconstructed K_S daughters for different numbers of hits in the T stations around the extrapolated Velo-Calo track.

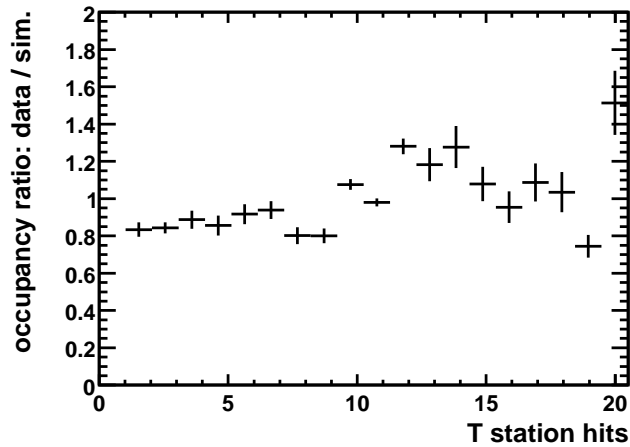
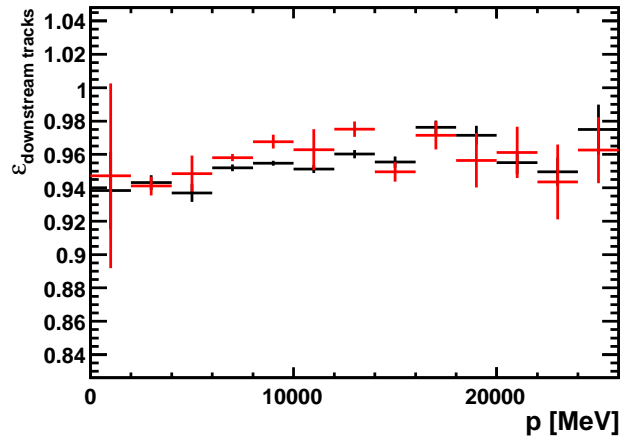
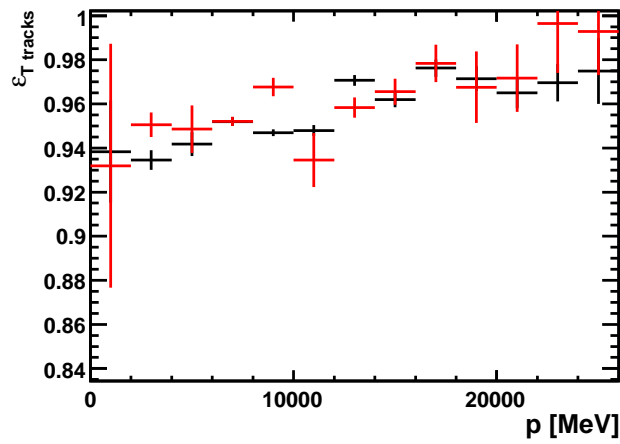


Figure 7.18: Weights given to simulated events to correct for different occupancy distributions in data and simulation. Due to small statistics for the determination of the weights, only events with less than 15 hits in the T station search window are considered for both simulation and data.

7. MEASUREMENT OF THE TRACKING EFFICIENCY IN THE T STATIONS WITH $K_S \rightarrow \pi^+\pi^-$

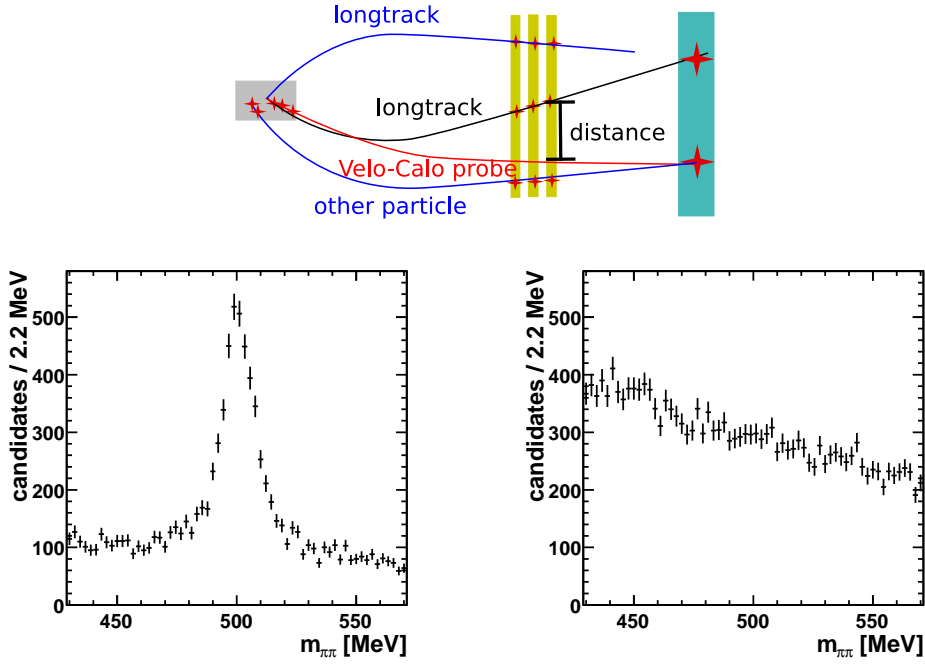


(a) Downstream tracks



(b) T tracks

Figure 7.19: Tracking efficiencies for standard tracks without hits in the VELO.



(a) Confirming track and confirmed probe go through the same module of the outer tracker.

(b) Confirming track and confirmed probe neither go through the same nor through adjacent modules of the outer tracker.

Figure 7.20: A wrong reconstructed Velo-Calo track (red) being confirmed by a correct reconstructed longtrack (black). For different distances between the confirmed probe and the confirming track, the invariant $\pi^+\pi^-$ mass spectrum is shown. Confirmed Velo-Calo ghosts contribute to the background but not to the signal part.

arises from these wrong confirmations because their contribution to the invariant mass spectrum is without any structure which would deteriorate the determination of N_{K_S} . This claim is verified by investigating for confirmed Velo-Calo tracks the distance between the confirmed probe and the confirming track in the T stations. In figure 7.20, the invariant $\pi^+\pi^-$ mass spectra of a longtrack and a confirmed Velo-Calo probe for different distances between confirmed probe and confirming track in the T stations are shown. The contribution of wrong matched Velo-Calo probes to the total invariant mass spectrum has no peak at the K_S mass. The result of the tag and probe method is therefore not truncated.

Table 7.3: Signal fraction, signal significance, and relative signal uncertainty for the different background reduction schemes. The according invariant mass spectra are shown in figure 7.21.

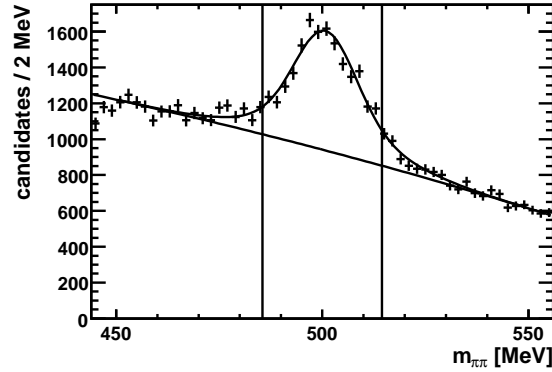
scheme	sig. fraction	rel. sig. uncertainty
1	0.296	0.0374
2	0.401	0.0926
3	0.568	0.0460
4	0.401	0.0926
5	0.568	0.0460

7.5 Effect of the Background Reduction in Velo-Calo Matching

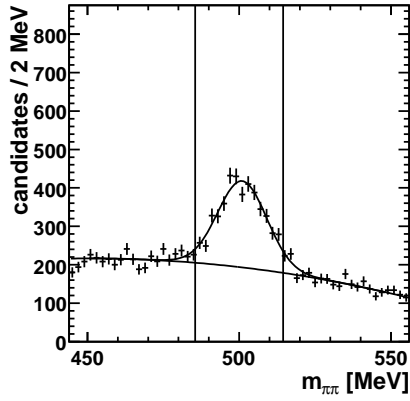
The invariant mass spectra for the different background reduction configurations in chapter 5 are shown in figure 7.21.

Within the signal window of $\pm 2\sigma$ the signal fraction $N_{K_S}/N_{\pi\pi}$ and the relative signal uncertainty $\sigma(N_{K_S})/N_{K_S}$ are analysed for all five background reduction schemes, the results are listed in table 7.3.

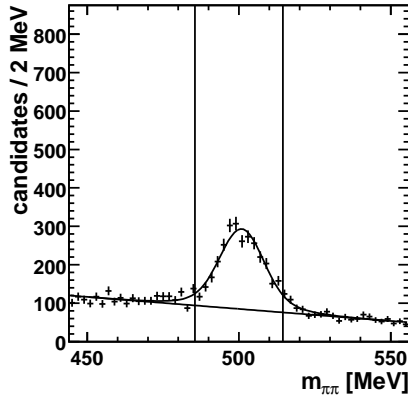
The small signal uncertainty would favour scheme 1 over the others, but given that the signal fraction for method 3 is much larger at a comparable signal uncertainty scheme 3 is chosen. This decision is purely for practical purpose because the CPU consumption scales with the number of candidates. At the same total CPU consumption method 3 will therefore yield a better measurement.



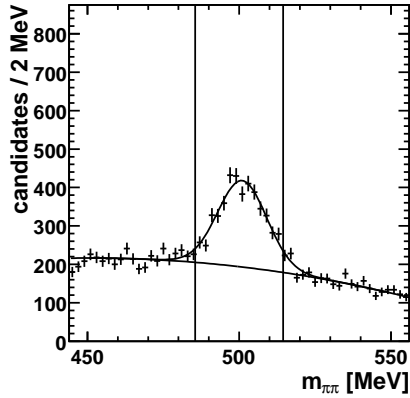
(a) Optimisation 1: No Optimisation



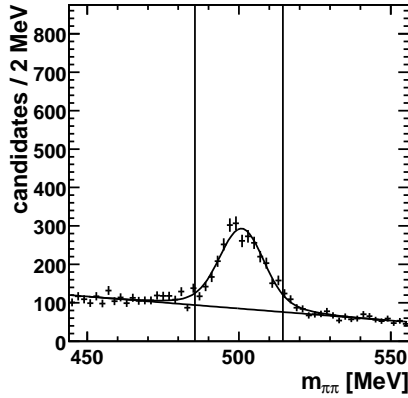
(b) Optimisation 2: The best calorimeter cluster for each Velo track.



(c) Optimisation 3: The best Velo track for each calorimeter cluster.



(d) Optimisation 4: The best calorimeter cluster for each Velo track and each cluster used only once.



(e) Optimisation 5: The best Velo track for each calorimeter cluster and each track used only once.

Figure 7.21: Comparison of the results of the different configurations of the background reduction in Velo-Calor matching. The indicated mass window is set to the 2σ window (500 ± 14.5 MeV). In the first histogram the range of the y axis is twice the range of the y axes of the other histograms. Detailed figures are given in table 7.3

Measurement of the Trigger Efficiency of the Muon Track Segment Reconstruction with $J/\psi \rightarrow \mu^+\mu^-$

Und inwieweit hat algebraische Geometrie jetzt was damit zu tun?

David Rohr

To decide which muon track segment reconstruction to use as a seed for Velo-Muon probes the original algorithms as well as the improved HLT algorithm were tested. In figure 8.1 the applied method is illustrated. In full reconstructed $J/\psi \rightarrow \mu^+\mu^-$ decays, for each muon is tested if the muon can also be reconstructed as a muon track segment. Thereby two muons per decay are tested as in the tag and probe method. The difference is, that in the tag and probe method each decay is reconstructed twice, i.e. as a probe-tag and as a tag-probe combination. Here both reconstructions are identical.

In contrast to the T station efficiency measurements in this work, this muon station efficiency measurement is biased given that the muon PID uses the same subdetector which is used for muon track segment reconstruction. The LHCb muon group applies a similar method to measure the muon PID performance [Jon10]. They do not require one of the decay products to be identified as a muon and thereby measure the muon PID efficiency unbiased.

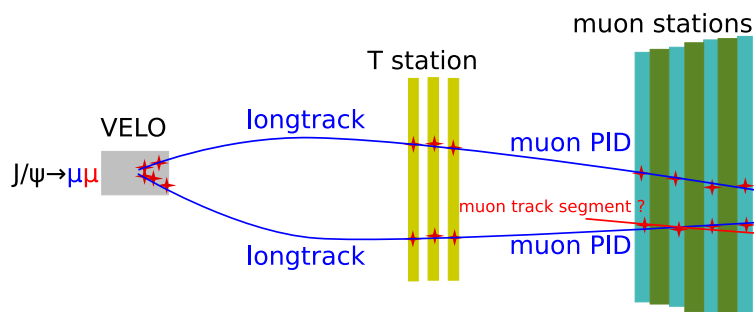


Figure 8.1: A $J/\psi \rightarrow \mu^+\mu^-$ used for the decay to be reconstructed for the efficiency measurement.

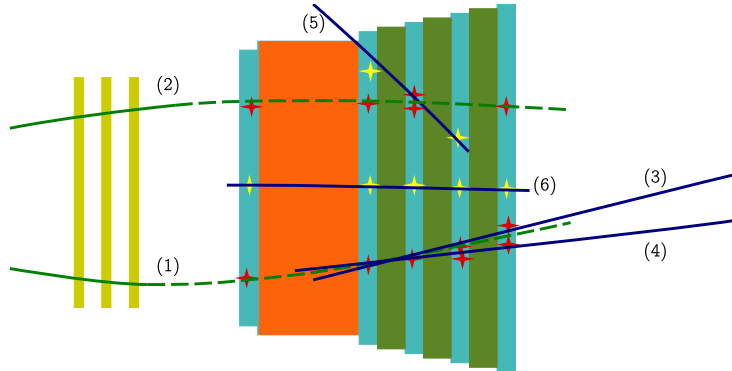


Figure 8.2: Comparison of muon tracks with the hits used to identify J/ψ decay muons (red). Hits not used for the identification are indicated yellow. Four muon track segments are found: (3) and (4) are built from hits which are used in the identification of J/ψ daughter (1). (5) from a cosmic particle going steep through the detector which is not of interest. (6) reconstructs a muon from the interaction but not from the J/ψ decay and is not of interest either. Only one of the two muons of interest (1) and (2) is found as a muon track segment.

8.1 Definition of the Trigger Efficiency

The quantity to optimise is not the efficiency to reconstruct muon track segments for any muon but for muons from the decay $J/\psi \rightarrow \mu^+\mu^-$. On the one hand that is the decay which will be used in the tag and probe method using Velo-Muon probes and on the other hand this is also a decay to be reconstructed in several trigger lines in the LHCb experiment.

The muon track segment reconstruction for the trigger has to be optimised to reconstruct muons from $J/\psi \rightarrow \mu^+\mu^-$ which are also identified in the standard reconstruction – there is no interest for the trigger to reconstruct muon track segments for muons which will not be identified as muons in the standard reconstruction. The *trigger efficiency*¹ in this chapter is defined as

$$\varepsilon_{\text{trigger}} = \frac{\#\text{identified muons which are reconstructed as a muon track segment}}{\#\text{identified muons}}.$$

Not maximising the absolute efficiency but the trigger efficiency imposes a bias because thereby muons which are not identified in the particle identification are not considered. The latter could still be used in the present tracking efficiency study. The bias is acceptable for trigger interests but also for the reconstruction of Velo-Muon probes because these will probe a subdetector which is independent from the muon stations.

To measure the trigger efficiency, $J/\psi \rightarrow \mu^+\mu^-$ decays have been reconstructed and the hits used to identify the tracks of muons (see section 2.5 and 3.2) are compared to those used for muon track segments. A muon is defined to be reconstructed by the muon track segment reconstruction if 90 % of the hits a muon track segment is built

¹This is *not* the efficiency to trigger an event. A positive HLT1 decision requires more than the reconstruction of a muon track segment.

from, have been used to identify the muon². In figure 8.2 that is the case for muon (1) and the track segments (3) and (4). The illustration furthermore shows:

- Both tracks of muons (1) and (2) were extrapolated to the muon stations to identify them. The hits in red are compatible to the extrapolation and thus *used to identify the muons*.
- Every hit used to reconstruct the track segments (3) and (4) has been used to *identify* muon (1). Muon (1) is therefore considered to be found as a muon track segment.
- Muon track segments (5) and (6) were built from hits which were not all used to identify a J/ψ daughter.
- There is no muon track segment which was built from the hits which identified muon (2). It is therefore not considered to be reconstructed as a muon track segment.

8.2 Event Selection

The events analysed in this chapter are taken from the di-muon stream applying the standard selection for $J/\psi \rightarrow \mu\mu$ at LHCb.

There is a bias if the muon track reconstruction efficiency is determined on events which were only triggered because a `HltMuonRec` successfully reconstructed a muon track segment – if only events with a positive `Hlt1SingleMuon` decision are analysed, `HltMuonRec` will be 100 % efficient. There are the following possible combinations³:

Both muons triggered HLT1: Both TISTOS muons can be used for the trigger efficiency measurement.

One muon triggered HLT1: Only the TIS muon can be used for the trigger efficiency measurement as the usage of the trigger-muon would bias the result.

None of the muons triggered HLT1: In principle both could be used without biasing the measurement but the event is likely to be a background event. The event is not considered in the measurement of the trigger efficiency.

The decision of HLT2 is not considered because there a complete event reconstruction is done and therefore the decision is independent from the muon track segment reconstruction⁴.

8.3 Trigger Efficiency Determination

Within the sample of tracks of muons, there will be ghosts or muons not originating from a J/ψ decay. The number of considered⁵ J/ψ daughters and as muon track segment reconstructed J/ψ daughters are therefore determined from invariant mass spectra.

²The percentage of common hits is a convenient choice. Not to depend on the number of hits per track, the percentage is chosen such that every of the track hits has to be used in the identification. The quoted efficiency will depend on this choice. The efficiencies for a different percentage is given in appendix B.1.

³TIS and TISTOS are defined on page 19.

⁴In the full reconstruction the muon stations are used as a PID device with the same settings as in the standard reconstruction.

⁵A muon is considered according to the trigger decision explained in the preceding section.

8. MEASUREMENT OF THE TRIGGER EFFICIENCY OF THE MUON TRACK SEGMENT RECONSTRUCTION WITH $J/\psi \rightarrow \mu^+\mu^-$

Table 8.1: Efficiencies to reconstruct a J/ψ daughter as a muon track segment for different algorithms and different settings. Considering the original algorithms the efficiency can be increased by 2 % by changing the seed station from M5 to M4 if M1 is not used.

algorithm	seed station	skip station	efficiency	tracks per J/ψ event
single algorithms				
HltMuonRec	M5		$88.6 \pm 1.8 \%$	2.16
MuonCombRec	M5		$80.3 \pm 1.7 \%$	2.21
MuonCombRec	M5	M1	$88.6 \pm 1.8 \%$	2.32
MuonCombRec	M4		$81.2 \pm 1.7 \%$	2.83
MuonCombRec	M5	M4	$79.3 \pm 1.7 \%$	2.36
MuonCombRec	M5	M3	$75.5 \pm 1.6 \%$	2.22
MuonCombRec	M5	M2	$70.9 \pm 1.5 \%$	2.20
MuonCombRec	M4	M1	$90.8 \pm 1.9 \%$	3.05
combination				
MuonCombRec	M5	one of M1-M5	$85.7 \pm 1.7 \%$	—
modified algorithms				
improved Hlt	M5	one of M2-M5	$93.5 \pm 1.9 \%$	3.50

There are five cases and the numbers of J/ψ decays for each case are abbreviated with a to e :

- a** **One** muon is considered which **is not** reconstructed as a muon track segment.
- b** **One** muon is considered which **is** reconstructed as a muon track segment.
- c** **Two** muons are considered but **no** muon is reconstructed as a muon track segment.
- d** **Two** muons are considered and **one** muon is reconstructed as a muon track segment.
- e** **Two** muons are considered and **both** muons are reconstructed as a muon track segment.

The efficiency then is

$$\varepsilon = \frac{b + d + 2e}{a + b + 2(c + d + e)}.$$

By testing the different algorithms not only the information whether a muon has been found by a certain algorithm can be analysed but also combined criteria, i.e. whether at least one of some different algorithms has found a muon.

Table 8.1 summarises the muon track segment finding efficiency for the different algorithms and configurations obtained from data.

The findings are that the efficiency is always below 82 % if a hit in M1 is required but above 88 % if M1 is not used. This means that MuonCombRec tends to pick up wrong hits in M1.

Furthermore not using hits in M2 or M3 decreases the efficiency⁶ while more tracks are found if no hits are required in either M4 or M5. This is a result of the tuning of

⁶As the muon identification already requires hits in both stations, no improvement can be measured here. Still the worsening is not expected.

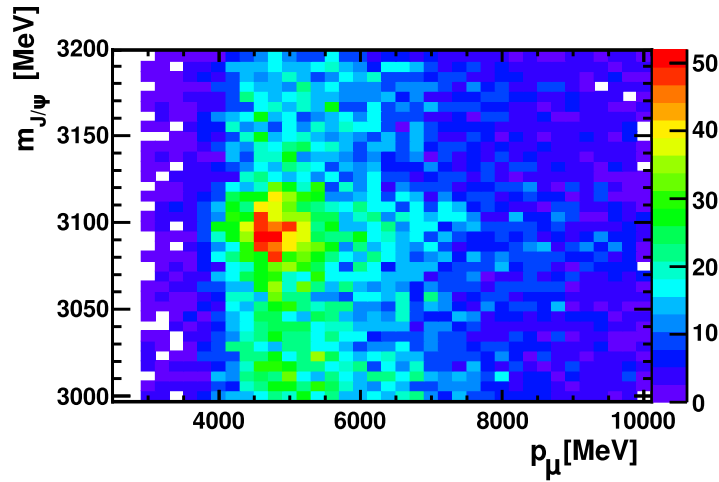


Figure 8.3: Momentum and reconstructed J/ψ mass for muons which are reconstructed as muon track segment by the improved HLT algorithm but *not* by the original algorithm. The J/ψ signal is visible in the momentum range from 4 GeV to 6 GeV. Thus, the improvement mainly improves the reconstruction of muons in that momentum range.

the search windows. Towards the end of the search, a good resolution is assumed and the search windows are small not to reconstruct ghosts. The assumed resolution is not maintained if M2 or M3 are skipped. Thus for skipped stations M2 or M3 the search windows are inappropriately small. In M4 or M5 on the other hand low momentum tracks can not have a hit because the particles are absorbed or scattered such that their hits are not within the search windows.

The muon track segment reconstruction can be improved by not requiring a certain hit pattern but a flexible criterion of a minimal number of stations to be hit. The requirement of three hits in M2-M5 is implemented in the improved HLT algorithm as explained in section 6.1. The improved algorithm performs best of all the tested algorithms.

The improved efficiency as a function of the muon momentum is demonstrated in figure 8.3:

For J/ψ daughters which are reconstructed by the improved HLT algorithm but not by the original HLT algorithm, the invariant mass of the reconstructed J/ψ decay and the muon momentum are shown. Several background tracks are reconstructed, i.e. ghosts or muons which are not J/ψ daughters but there is also a J/ψ signature visible, especially in the momentum range from 4 GeV to 6 GeV.

Measurement of the Tracking Efficiency in the T Stations with $J/\psi \rightarrow \mu^+ \mu^-$

Und deswegen gibt es vier Zerfallsketten. . . . Jetzt habe ich mich wahrscheinlich lächerlich gemacht, aber Lernforscher sagen ja, dass man das am besten behält.

Thomas Walke

Similar to the previous efficiency measurement, using K_S decays, J/ψ decays are reconstructed in this chapter using a longtrack and a Velo-Muon probe to measure the tracking efficiency as to be seen in figure 9.1.

The current stripping of LHCb does not provide an appropriate stripping stream for that study. The current status, the results from the most appropriate stream, and a dedicated stripping line are explained in this chapter.

9.1 Current Stripping Status

Each event in the “di-muon” stripping stream has passed a preselection for J/ψ decays. That preselection requires the decay products of the J/ψ candidate to be reconstructed as longtracks. The result of any tracking efficiency measurement using J/ψ decays from the di-muon stream will therefore measure 100 %.

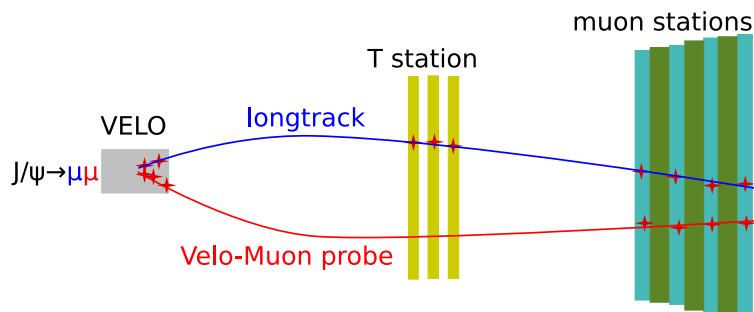


Figure 9.1: A $J/\psi \rightarrow \mu^+ \mu^-$ decay to be reconstructed for the efficiency measurement.

Table 9.1: Cuts to select J/ψ decays. Velo-Muon probes are by construction tracks from muons.

variable	StdLooseJPsi	modified selection
p_T (longtrack)	> 500 MeV	> 800 MeV
p_T (Velo-Muon probe)	> 500 MeV	—
p_T (J/ψ)	> 1 GeV	> 1 GeV
χ^2/ndof (longtrack)	< 5	< 5
χ^2/ndof (Velo-Muon probe)	< 5	< 10
χ^2/ndof (vertex)	< 10	< 5
distance of closest approach	—	< 1.5 mm
PID (longtrack)	pos. muon PID	pos. muon PID

The events for the preceding K_S study were taken from the “minimum bias” stream. The event selection in the minimum bias stream imposes the least possible bias – every event with two charged tracks, which do not even need to come from a common vertex, are selected. As the minimum bias stream was established for studies which need only small data samples corresponding to small luminosities, the stripping lines in that stream are prescaled. Due to this prescaling the minimum bias stripping comprises an integrated luminosity of $\sim 14 \text{ nb}^{-1}$ which is insufficient for the tag and probe tracking efficiency study using J/ψ decays – the measurement is dominated by statistical uncertainty.

9.2 Selection of J/ψ Events

The selection of J/ψ decays is on the one hand more difficult than the K_S selection because the powerful flight distance cut is not applicable as the J/ψ decays at its production point, on the other hand there are far less muons than pions produced in a proton-proton collision, therefore the selection of the right muons as a combinatorial task is easier.

Given that the spatial resolution of Velo-Muon probes is comparable to longtracks and that the momentum resolution is better than 1 %, the standard selection of J/ψ decays at LHCb can be used as a starting point for the Velo-Muon probe based reconstruction of J/ψ decays.

The cuts applied are those from the standard selection `StdLooseJPsi` (as far as applicable) with a few modifications shown in table 9.1. The modifications aim to increase the phase space of the Velo-Muon reconstructed decay product without increasing the background.

As for K_S the DOCA cut is introduced to reduce the CPU consumption, especially for the stripping line which will later be explained.

9.3 First Results

Using the largest minimum bias data set available a first impression of the results can be obtained. The invariant mass spectrum of a Velo-Muon probe combined with a longtrack is shown in figure 9.2 as well as for confirmed Velo-Muon probes. The

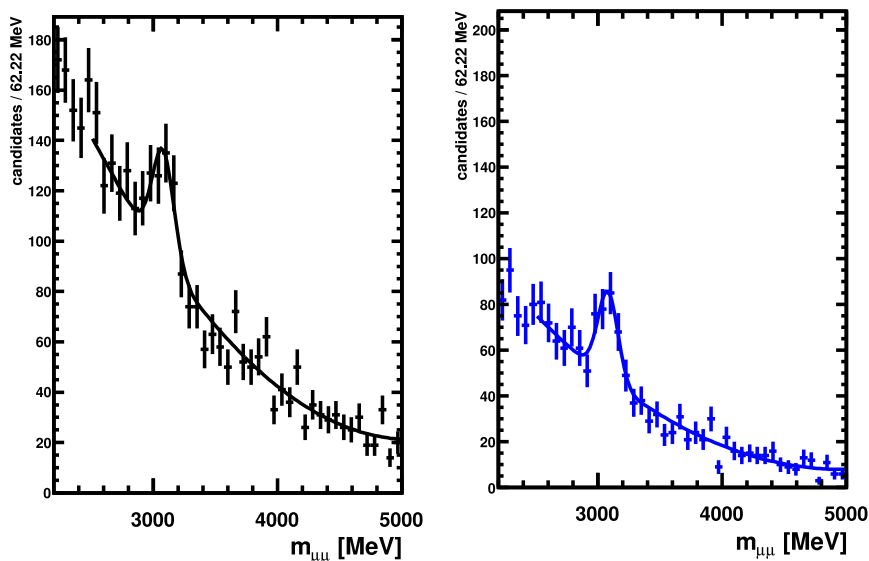


Figure 9.2: The di-muon invariant mass spectrum of a Velo-Muon probe and a longtrack using the largest minimum bias data sample. 150 J/ψ decays were reconstructed of which 125 are in the subset of confirmed Velo-Muon probes. For better background estimation the shown mass window is much broader than in figure 9.3. Due to the broader mass window the background looks much steeper.

corresponding efficiency is 83 ± 14 %. Small statistics makes this result rather a proof of principle than a measurement but ensures that the method is applicable.

9.4 Developed Stripping Line

For the tracking efficiency measurements involving J/ψ decays, a stripping line has been established. As the stripping is run after the standard reconstruction, the specifications of stripping lines are designed for decisions which can be made without further reconstruction. The fit procedure of all Velo tracks and the reconstruction of muon tracks and afterwards Velo-Muon probes already need more time than is allowed. Moreover, stripping lines for physics analyses deal with longtracks which have a lower ghost rate than Velo-Muon probes, the background contribution to the selected events is therefore expected to be higher and simultaneously the retention rate is higher than allowed.

Additionally, the stripping lines for physics analyses have been optimised on previous stripping versions – analysing less data without prescaling. For the tracking efficiency stripping line no such old data set is available to tune the selection and the data sets provided by the stripping group are too small to perform such an optimisation – these are provided only to measure the retention rate and CPU consumption.

The major criterion for the development of the tracking efficiency stripping lines therefore was to meet the computing restrictions while the chosen cuts must be loose

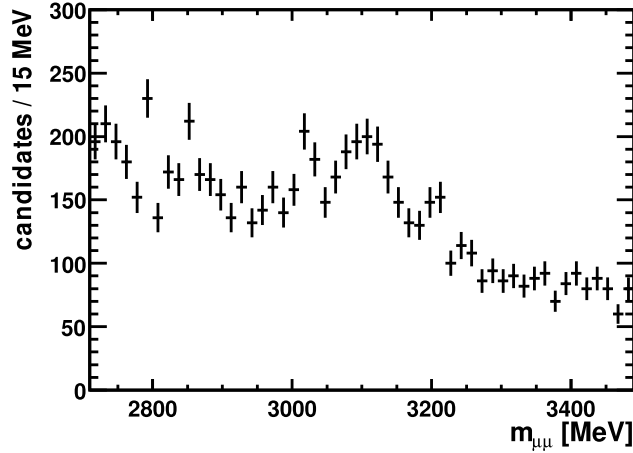


Figure 9.3: Candidates selected by the stripping line developed for the tracking efficiency study.

enough that any further improvement of the selection will lead to harder cuts which then can be evaluated on the stripped data sample.

As explained in chapter 6, requiring a HLT1 single muon decision is a reasonable criterion for the tracking efficiency measurement. This requirement already reduces the number of events to be analysed by a factor 200 without CPU consumption.

For the fit of the Velo tracks, a simplified description of the detector is used which has been developed for the HLT2. As the Velo track segments will be fitted again, using also measurements in the muon stations once they are matched to muon tracks, the resolution of Velo-Muon probes is independent of the detector description in that first Velo track fit.

Figure 9.3 shows the invariant mass spectrum using the developed stripping line obtained from an event sample which has been provided to test stripping lines. It contains $\sim 703 J/\psi$ among 6829 background candidates.

9.5 Phase Space Coverage

In table 9.2 the efficiency of the Velo-Muon probe reconstruction of J/ψ decay products is given for simulated events. The corresponding phase space coverage is illustrated in figure 9.4. Remarkable is the different momentum scale with respect to Velo-Calo probes.

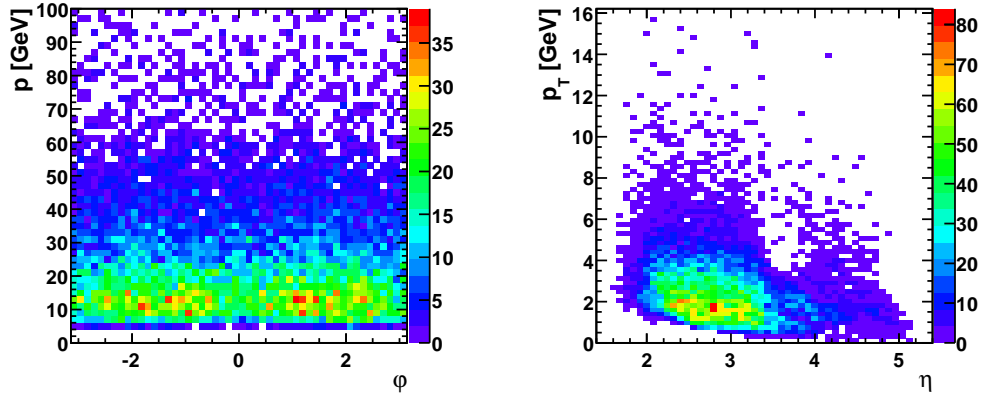
At $\eta \approx 3.6$ the number of reconstructed muons is smaller than for larger or smaller pseudo rapidities. While the low momentum range is still covered, for $p_T > 3$ GeV the η distribution of correct matched Velo-Muon probes has a distinct dip as shown in figure 9.4(c). Given that the matching efficiency of Velo tracks to muon track segments is not lower in this region than in the other regions, this is interpreted as a lower efficiency to reconstruct muon track segments in region 1.

The efficiency to reconstruct muons from $B_s^0 \rightarrow J/\psi X$ has been investigated because in the development of the stripping line the usage of *displaced*¹ J/ψ has been proposed.

¹I.e. J/ψ which are not produced in the primary vertex.

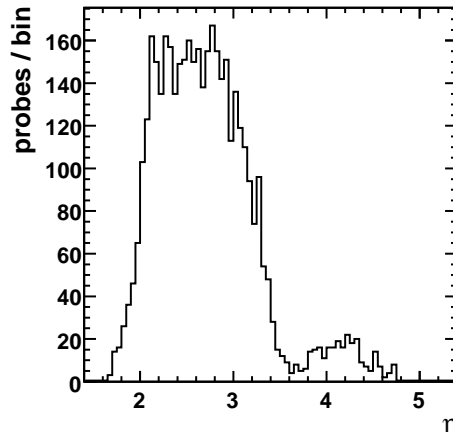
Table 9.2: Performance of the Velo-Muon probe matching in simulated events. The first figures indicate the total efficiencies (efficiency to reconstruct a J/ψ daughter in the detector acceptance) while the second one is the matching efficiency, i.e. the efficiency to reconstruct Velo-Muon reconstructible J/ψ daughters. The efficiencies are lower than the average expected from table 6.2 which is no contradiction as here only J/ψ decay products are considered.

event type	Velo-Muon efficiency	Velo-Muon <i>match</i> efficiency
$J/\psi \rightarrow \mu^+\mu^-$ at $\sqrt{s} = 10$ TeV	$59.5 \pm 0.2\%$	$75.6 \pm 0.2\%$
$B_s^0 \rightarrow J/\psi\phi \rightarrow$ $\mu^+\mu^-K^+K^-$ at $\sqrt{s} = 10$ TeV	$59.8 \pm 0.2\%$	$73.8 \pm 0.2\%$
$J/\psi \rightarrow \mu^+\mu^-$ at $\sqrt{s} = 7$ TeV	$58.17 \pm 0.05\%$	$74.00 \pm 0.05\%$
$B_s^0 \rightarrow J/\psi\phi \rightarrow$ $\mu^+\mu^-K^+K^-$ at $\sqrt{s} = 7$ TeV	$58.79 \pm 0.05\%$	$72.13 \pm 0.05\%$



(a) Coverage in momentum and azimuthal angle in the VELO.

(b) Coverage in transverse momentum and pseudorapidity.



(c) Pseudo-rapidity distribution for Velo-Muon probes with large transverse momenta. The region with less probes coincides with region 1 of the muon stations.

Figure 9.4: The phase space covered by correct reconstructed Velo-Muon probes from simulated J/ψ decays at $\sqrt{s} = 7$ TeV – the energy at which LHC is operated in 2010. For transverse momenta larger than 3 GeV not the whole η range is covered.

Error Discussion

Du, ich kann morgen nicht. Ich muss alle xkcd nochmal lesen.

Sebastian Jeltsch

The common way to estimate the error of an efficiency is to quote the standard deviation of a binomial distribution $\sigma_\varepsilon = \sqrt{\varepsilon(1-\varepsilon)/N}$. As explained by [Cas10], this is a common mistake in efficiency determination. Moreover, even if that formula was correct, it would not be applicable to efficiencies determined with the tag and probe method.

The correct version of the above formula is explained in the first section of this chapter. It has been used for all efficiencies which were determined in simulations. A formula which is applicable to efficiencies determined with the tag and probe method is given in the second section. The latter formula has been used throughout chapter 7.

Throughout this chapter it is assumed that k out of N particles have been found in the subdetector of which the efficiency is measured.

10.1 Error Estimation for Certain Processes

Probabilities of a binomial process are given by the binomial distribution.

$$B(k|\varepsilon, N) = \binom{N}{k} \varepsilon^k (1-\varepsilon)^{N-k}$$

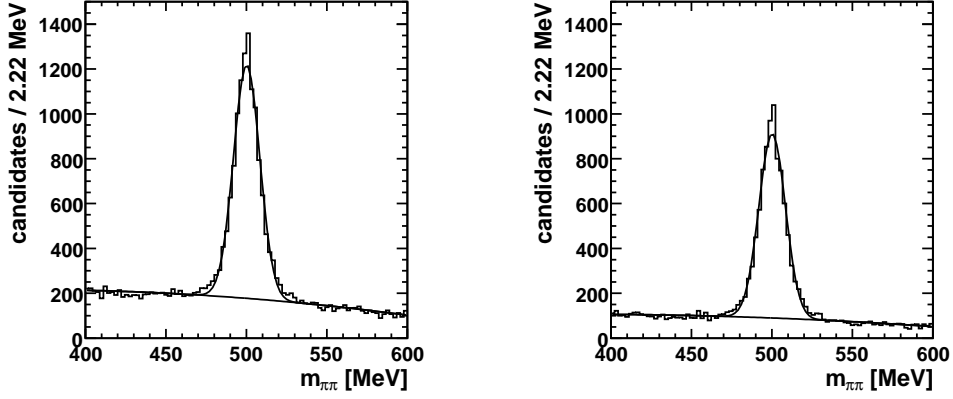
For fixed ε the variance of k/N is known to be $\varepsilon(1-\varepsilon)/N$ which parametrises the spread of k/N around the expectation value ε .

If however k and N is known for a sample and ε is estimated, the variance of ε for fixed N and k is of interest. Applying Bayes theorem and considering Jeffreys' prior (as recommended by [Cas10]) the likelihood function for ε is given by a Beta distribution.

$$B(\varepsilon|k, N) = \frac{N!}{(k-1/2)!(N-k-1/2)!} \varepsilon^{k-1/2} (1-\varepsilon)^{N-k-1/2}$$

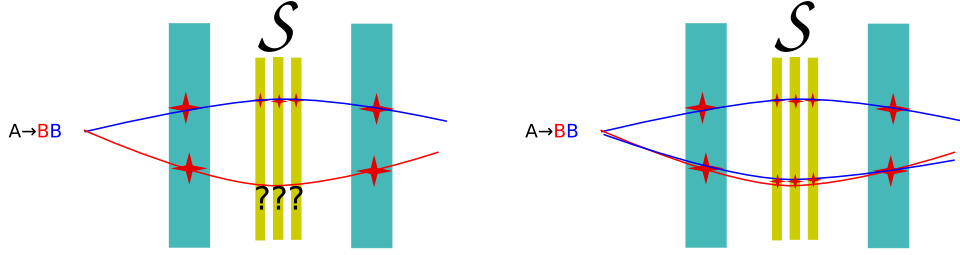
The variance of ε is than

$$\sigma_\varepsilon^2 = \frac{(k+1/2)(N-k+1/2)}{(N+1)^2(N+2)} \quad (10.1)$$



(a) Invariant masses of a signature and a full reconstructed track.

(b) The subset of (a) which is also reconstructible with two full reconstructed tracks.



(c) Example of a simulated decay in (a).

(d) Example of a simulated decay in (b).

Figure 10.1: Invariant mass histograms of a toy simulation which are used to investigate fit routines used in the tag and probe method.

10.2 Error Estimation in the Tag and Probe Method

The above formula is only applicable if N and k are certain numbers. In the tag and probe method however the numerator and denominator of the efficiency are determined fitting a model to an invariant mass histogram and are therefore uncertain numbers, both with an error estimate from the fit routine. That the error of the measured efficiency is underestimated if formula 10.1 is used, is proven in appendix C.

For the efficiency estimator $\varepsilon = k/N$ Gaussian error propagation leads to the following error estimate

$$\sigma_\varepsilon^2 = \frac{1}{N^2}\sigma_k^2 + \frac{k^2}{N^4}\sigma_N^2 - 2\frac{k}{N^3}\sigma_N\sigma_k \text{Corr}(k, N) \quad (10.2)$$

It is expected that the estimates for N and k are correlated. The correlation has been investigated in a toy simulation. According to the fit model from chapter 7, there have been 700 invariant mass histograms with 12 500 entries simulated and fitted – one of them shown in figure 10.1(a). Each of the 12 500 entries represents a two body decay reconstructed with a probe and a full reconstructed track. At random – the probability is given by the simulated efficiency of the subdetector – the probes have been confirmed as illustrated in figure 10.1(b).

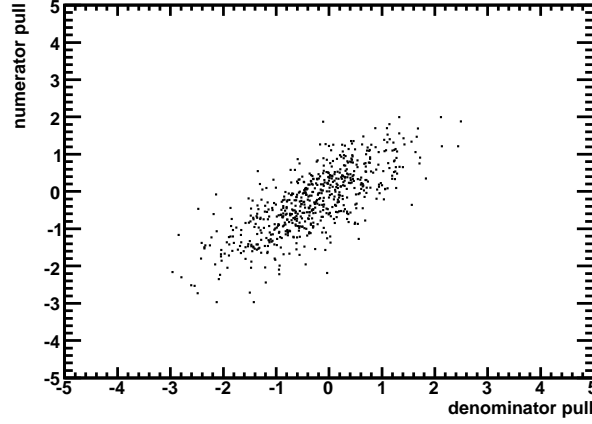


Figure 10.2: Distribution of $\text{pull}(k)$ (numerator pull) and $\text{pull}(N)$ (denominator pull) in 700 toy experiments with 10,000 simulated K_S decays among 12,500 reconstructed decays per experiment. The correlation is 0.76.

The discrepancy between the number of simulated signals and the fit result is quantified with the pull:

$$\text{pull}(N) = \frac{N_{\text{fit}} - N_{\text{true}}}{\Delta N}$$

The above correlation is equal to the correlation of the pulls

$$\text{Corr}(k, N) = \text{Corr}(\text{pull}(k), \text{pull}(N))$$

which is illustrated in figure 10.2. The correlation is 0.76 and therefore cannot be neglected.

This correlation however cannot be determined in the efficiency *measurement*. A possible remedy would be the usage of the correlation from the toy experiments for the error estimation which would require performing several toy experiments for each data point¹.

A different way, without the usage of simulations has been chosen to estimate the uncertainty of the measured efficiencies. The idea is to decorrelate the two variables N and k by splitting up the set of all N decays into those k with a confirmed probe and $(N - k)$ decays with an unconfirmed probe. The variables k and $(N - k)$ are therefore expected to be uncorrelated.

Error propagation using those uncorrelated variables yields

$$\sigma_\varepsilon^2 = \left(\frac{1}{N} - \frac{k}{N^2} \right)^2 \sigma_k^2 + \left(\frac{k}{N^2} \right)^2 \sigma_{(N-k)}^2$$

where $\sigma_{(N-k)}^2$ is still unknown. Assuming $\sigma_N^2 = \sigma_k^2 + \sigma_{(N-k)}^2$, the following formula can be derived.

$$\sigma_\varepsilon^2 = (1 - 2\varepsilon) \left(\frac{\sigma_k}{N} \right)^2 + \varepsilon^2 \left(\frac{\sigma_N}{N} \right)^2 \quad (10.3)$$

¹There are 714 data points in chapter 7.

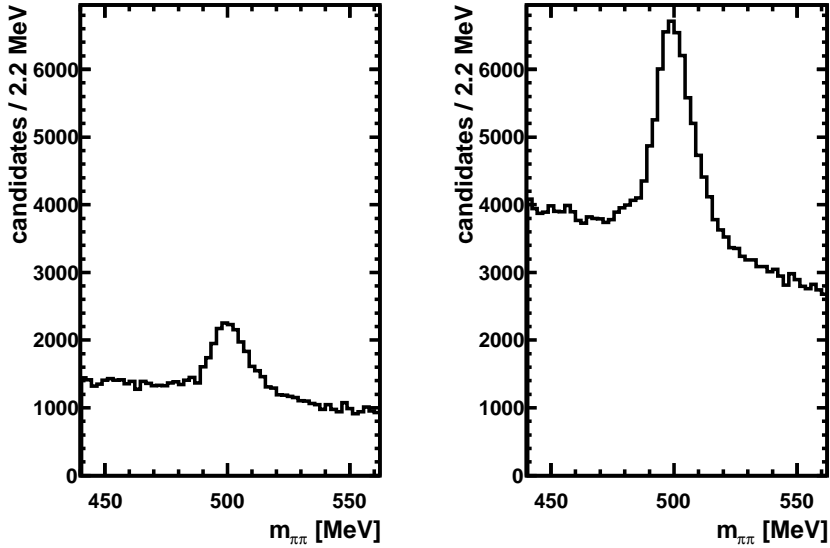


Figure 10.3: The mass histogram on the left is obtained requiring a signal in both, the SPD and in the HCAL, in front of and behind the calorimeter cluster used for building Velo-Calo tracks. Releasing this cut yields the histogram on the right.

In contrast to the derivation of formula 10.1, a possible difference $\varepsilon - k/N \neq 0$ is not considered. In a toy simulation the error estimate 10.3 has been tested. The results of that simulation are given in appendix C.

10.3 Consequences for Velo-Calo Probes

It is common to maximise the signal to background ratio N/B when cuts for a particle selection are developed. The above result for the error of the efficiency measurement reveals however, that minimising the relative signal uncertainty σ_N/N is more important than maximising N/B .

In section 5.3 it has been proposed to use only those calorimeter clusters for Velo-Calo probes which have a signal in the SPD and in the HCAL in front of the cluster or behind it respectively. The influence of that cut on the K_S yield is shown in figure 10.3.

Applying the cut, the relative signal uncertainty is $\sigma_N/N = 400/11\,000 = 0.036$. Without the requirement it is $\sigma_N/N = 720/30\,000 = 0.024$. For the tracking efficiency study the cut worsens the measurement.

Conclusion and Outlook

Warum haben sie eigentlich
BaBar – ein Präzisionsexperiment
– auf den San Andreas Graben
gebaut?

Sebastian Wandernoth

For elaborate physics studies the detector performance and the performance of the reconstruction have to be known. With the first data the tracking efficiency of the LHCb detector has been investigated and compared to the simulations.

In this work, two reconstruction algorithms for T station probes have been presented. The tag and probe method is used to measure the tracking efficiency with both of them.

In the first implementation K_S decay products are reconstructed from clusters in the calorimeters and track segments in the VELO. In average the tracking efficiency is 0.7 % lower than in the simulation while the dependency on all investigated quantities is in agreement with the simulation. The result of the measurement is that 95.5 ± 0.5 % of all Velo-Calo reconstructed K_S decay products are found by the standard track reconstruction in the T stations.

These K_S daughters allow tracking efficiency measurements up to transverse momenta of 800 MeV which covers most of the phase space of particles produced at LHCb. The transverse momentum range still needs to be extended towards higher momenta to cover the full field of interest for physics analyses. The tracking efficiency for high energetic particles will be measured with the reconstruction of J/ψ decay products from Velo tracks and muon track segments.

The latter method needs a larger integrated luminosity which is not available unbiased. It has been integrated into the stripping framework to acquire an unbiased data sample of Velo-Muon reconstructible J/ψ decays in the next reprocessing. A first analysis of a small data set showed that the method is applicable¹.

Developing the dedicated algorithms, also the performance of different tracking algorithms in the muon stations, which are not part of the standard track reconstruction at LHCb, has been investigated. Furthermore the track reconstruction in the muon stations used in the trigger has been improved by five percent. Thereby the momentum range of muons which can be reconstructed as Velo-Muon probes has been extended towards low momenta.

¹[Ste08] showed results for a simulated signal sample, the contribution from events without a reconstructible J/ψ decay has not been tested.

Acknowledgements

Ich möchte der gesamten HE Gruppe des Physikalischen Instituts für die Unterstützung und zahlreichen Ratschläge während der Arbeit an diesem Projekt danken. Insbesondere Ulrich Uwer, der es mir ermöglicht hat, dieses interessante Thema zu bearbeiten.

Die Diskussionen und Zusammenarbeit mit Sebastian Wandernoth und Christian Linn haben wohl die meisten Probleme im Rahmen der Arbeit gelöst. Außerdem möchte ich Georg Krockner danken, dessen technische Unterstützung die Implementierung der Stripping Line erst möglich gemacht hat.

Besonders danken möchte ich Stephanie Hansmann-Menzemer und Manuel Schiller, auf deren Kenntnis der Spurrekonstruktion und der Software bei LHCb ich mich jederzeit verlassen konnte.

Maßgeblich für die angenehme Atmosphäre bei der Arbeit sind wohl Marco Meißner, Alexander Bien, Sascha Stahl, Anna Weber, und Christoph Tremmel verantwortlich, mit denen ich mir das Büro geteilt habe.

Außerhalb der HE Gruppe gebührt Hans-Christian Schultz-Coulon besonderer Dank, der sich freundlicherweise bereit erklärt hat, die Rolle des Zweitgutachters zu übernehmen. Johannes Albrechts Hilfe beim Einstieg in das Projekt war enorm und hat unlösbar scheinende Unklarheiten beseitigt. In der Korrespondenz mit Diego Casadei konnten die komplizierten Aspekte der Fehlerbetrachtung geklärt werden.

Großer Dank gebührt meinen Freunden, die mich während des Studiums begleitet haben, insbesondere Sebastian Jeltsch und Moritz Klein mit denen ich mich auf die Diplomprüfungen vorbereitet habe.

Jan de Cuveland, Jasper Franke und Arno Trautmann haben weit mehr zu dieser Arbeit beigetragen als ihre Zitate, die den Physiker Alltag etwas ernüchternd aber dennoch ehrlich darstellen. Neben Oliver Thomas hatte ihr Wissen über Textsatz Einfluss auf jede einzelne Seite.

Derivations

A.1 Muon Track Fit

As stated in 6.3, the track segments reconstructed in the muon stations are fitted with a straight line

$$\begin{pmatrix} x(z) \\ y(z) \end{pmatrix} = \begin{pmatrix} b + t_x z \\ t_y z \end{pmatrix}$$

which minimises the χ^2 of the distance of the hits from the track.

$$\chi^2 = \sum_{\text{hits}} \frac{(x(z) - x_{\text{hit}})^2}{\sigma_{x,\text{hit}}^2} + \sum_{\text{hits}} \frac{(y(z) - y_{\text{hit}})^2}{\sigma_{y,\text{hit}}^2}$$

The scale factors to correct for material interaction are omitted here for simplicity – the $\sigma_{y,\text{hit}}$ denominators are to be understood including the scale factors.

For the optimal parameters t_y , b , and t_x the derivatives $\partial\chi^2/\partial t_y$, $\partial\chi^2/\partial b$, and $\partial\chi^2/\partial t_x$ vanish.

$$\begin{aligned} \frac{\partial\chi^2}{\partial t_y} &= 2 \sum_{\text{hits}} \frac{(t_y z - y_{\text{hit}})z}{\sigma_{y,\text{hit}}^2} \\ \frac{\partial\chi^2}{\partial b} &= 2 \sum_{\text{hits}} \frac{t_x z + b - x_{\text{hit}}}{\sigma_{x,\text{hit}}^2} \\ \frac{\partial\chi^2}{\partial t_x} &= 2 \sum_{\text{hits}} \frac{(t_x z + b - x_{\text{hit}})z}{\sigma_{x,\text{hit}}^2} \end{aligned}$$

The equations are linear in the parameters and therefore straight forward to solve.

The slope in the $y - z$ plane is:

$$\begin{aligned} \frac{\partial\chi^2}{\partial t_y} &= 0 \\ \Rightarrow 0 &= t_y \sum_{\text{hits}} \frac{z^2}{\sigma_{y,\text{hit}}^2} - \sum_{\text{hits}} \frac{y_{\text{hit}} z}{\sigma_{y,\text{hit}}^2} \\ \Rightarrow t_y &= \left(\sum_{\text{hits}} \frac{y_{\text{hit}} z}{\sigma_{y,\text{hit}}^2} \right) / \left(\sum_{\text{hits}} \frac{z^2}{\sigma_{y,\text{hit}}^2} \right) \end{aligned}$$

While in the $x - z$ plane one gets a system of two linear equations

$$\frac{\partial\chi^2}{\partial b} = 0$$

$$\begin{aligned} \frac{\partial \chi^2}{\partial t_x} &= 0 \\ \Rightarrow 0 &= b \sum_{\text{hits}} \frac{1}{\sigma_{x,\text{hit}}^2} + t_x \sum_{\text{hits}} \frac{z}{\sigma_{x,\text{hit}}^2} - \sum_{\text{hits}} \frac{x}{\sigma_{x,\text{hit}}^2} \\ \text{and } 0 &= b \sum_{\text{hits}} \frac{z}{\sigma_{x,\text{hit}}^2} + t_x \sum_{\text{hits}} \frac{z^2}{\sigma_{x,\text{hit}}^2} - \sum_{\text{hits}} \frac{xz}{\sigma_{x,\text{hit}}^2} \end{aligned}$$

which is solved by

$$\begin{aligned} b &= \left(\sum_{\text{hits}} \frac{x}{\sigma_{x,\text{hit}}^2} \sum_{\text{hits}} \frac{z^2}{\sigma_{x,\text{hit}}^2} - \sum_{\text{hits}} \frac{xz}{\sigma_{x,\text{hit}}^2} \sum_{\text{hits}} \frac{z}{\sigma_{x,\text{hit}}^2} \right) \\ &\quad / \left(\sum_{\text{hits}} \frac{1}{\sigma_{x,\text{hit}}^2} \sum_{\text{hits}} \frac{z^2}{\sigma_{x,\text{hit}}^2} - \left(\sum_{\text{hits}} \frac{z}{\sigma_{x,\text{hit}}^2} \right)^2 \right) \\ t_x &= \left(\sum_{\text{hits}} \frac{1}{\sigma_{x,\text{hit}}^2} \sum_{\text{hits}} \frac{x^2}{\sigma_{x,\text{hit}}^2} - \sum_{\text{hits}} \frac{x}{\sigma_{x,\text{hit}}^2} \sum_{\text{hits}} \frac{z}{\sigma_{x,\text{hit}}^2} \right) \\ &\quad / \left(\sum_{\text{hits}} \frac{1}{\sigma_{x,\text{hit}}^2} \sum_{\text{hits}} \frac{z^2}{\sigma_{x,\text{hit}}^2} - \left(\sum_{\text{hits}} \frac{z}{\sigma_{x,\text{hit}}^2} \right)^2 \right) \end{aligned}$$

A.2 Optimising the z Value of Velo-Muon Matching in y

In the Velo-Muon tracking, Velo tracks and muon tracks are combined if their extrapolations meet in between the two subdetectors. As neither extrapolation is perfect and the track is not perfectly linear the extrapolations are not required to meet but to be not too distant from each other. For correct combined Velo tracks and muon tracks, the calculated distance should be in agreement with 0. The most significant distance determination is therefore assumed to be done at the z position of the least error estimate. The following calculation shall demonstrate how the accuracy of the determination of a track's slope in a subdetector influences the error on the distance between the extrapolations.

For simplicity the coordinates in the calculation are with respect to the last Velo state, i.e. the last Velo state is at $(0, 0)$. The local track parameters for the Velo track are indicated by the index V, those for the muon track by the index M. z is position where the distance is calculated.

$$\begin{aligned} d &= t_{yV}z - (y_M - t_{yM}(z_M - z)) \\ \Rightarrow \Delta d &= \sqrt{(\Delta t_{yV})^2 z^2 + (\Delta y_M)^2 + (\Delta t_{yM})^2 (z_M - z)^2} \\ \frac{\partial \Delta d^2}{\partial z} &= 2(\Delta t_{yV})^2 z - 2(\Delta t_{yM})^2 (z_M - z) \\ &\stackrel{!}{=} 0 \\ \Delta t_{yM}^2 z_M &= (\Delta t_{yV}^2 + \Delta t_{yM}^2) z \\ z &= \frac{\Delta t_{yM}^2}{\Delta t_{yV}^2 + \Delta t_{yM}^2} z_M \end{aligned}$$

The distance determination is best where the derivative vanishes. To illustrate the implications of this formula one should notice that the optimal z position for a perfect VELO ($\Delta t_{yV} = 0$) is at the muon station measurement and the optimal z position for a perfect muon track is at the VELO. Each time the error arising from both extrapolations is minimised by using the perfect detector instead.

It is worth noticing that this calculation does not investigate the distance between incorrect combined Velo tracks and muon tracks. It is neither assured that the most significant distance calculation automatically makes the distance between incorrect matches smaller than the distance between correct matches.

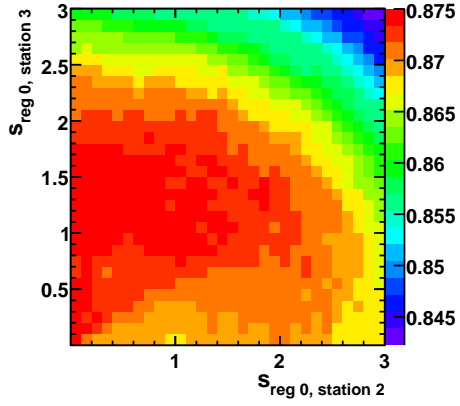
Tables and Figures

B.1 Muon Track Reconstruction Efficiencies

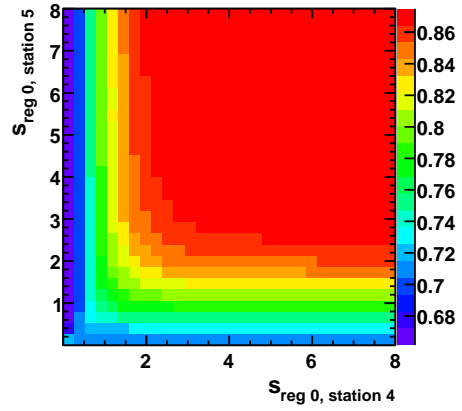
In section 8.3 the efficiencies of different muon track reconstruction algorithms are given. These depend on the definition when a track is supposed to be found. In table 8.1 figures for 90 % common hits of a muon track with a muon identification hit pattern are given. Table B.1 contains the efficiencies of the same algorithms on same data sample but for 60 % common hits.

Table B.1: Efficiencies to reconstruct a J/ψ daughter for different muon track reconstructions. 60 % of the hits used for track finding need to be used for the muon's particle identification.

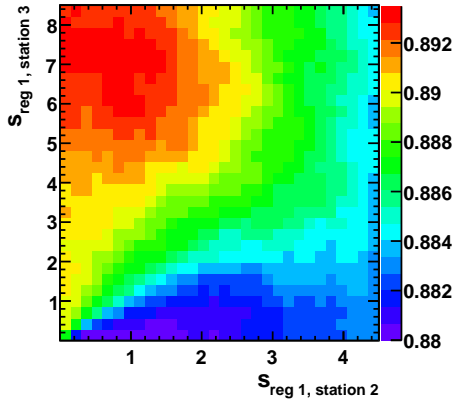
algorithm	seed station	skip station	efficiency	tracks per J/ψ event
single algorithms				
HltMuonRec	M5		89.8 ± 1.9 %	2.16
MuonCombRec	M5		87.7 ± 1.9 %	2.21
MuonCombRec	M5	M1	91.1 ± 1.9 %	2.32
MuonCombRec	M4		88.5 ± 1.9 %	2.83
MuonCombRec	M5	M4	86.4 ± 1.8 %	2.36
MuonCombRec	M5	M3	83.5 ± 1.8 %	2.22
MuonCombRec	M5	M2	82.2 ± 1.8 %	2.20
MuonCombRec	M4	M1	92.9 ± 2.0 %	3.05
combination				
MuonCombRec	M5	one of M1-M5	94.5 ± 2.0 %	—
modified algorithms				
improved Hlt	M5	one of M2-M5	97.9 ± 2.0 %	3.50
MuonCombRec	M5	M1 & M4	90.4 ± 1.9 %	2.51
MuonCombRec	M5	M1 & M3	88.0 ± 1.9 %	2.41
MuonCombRec comb.	M5	M1 & one of M3-M5	94.3 ± 2.0 %	—



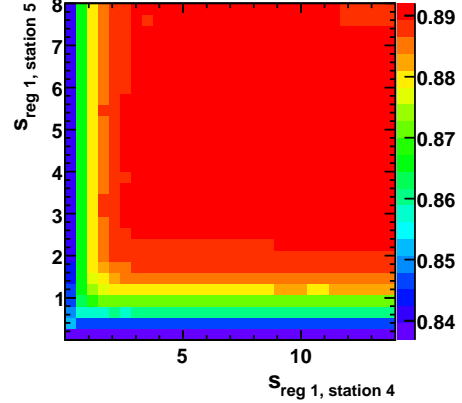
(a) Region 0 in stations M2 and M3.



(b) Region 0 in stations M4 and M5.



(c) Region 1 in stations M2 and M3.



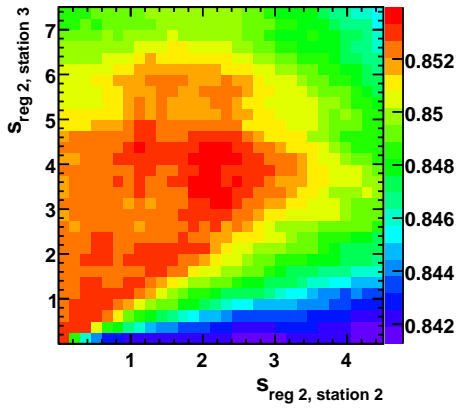
(d) Region 1 in stations M4 and M5.

Figure B.1: Velo-Muon matching efficiency as a function of the scaling factors modifying the fit of the muon track segment.

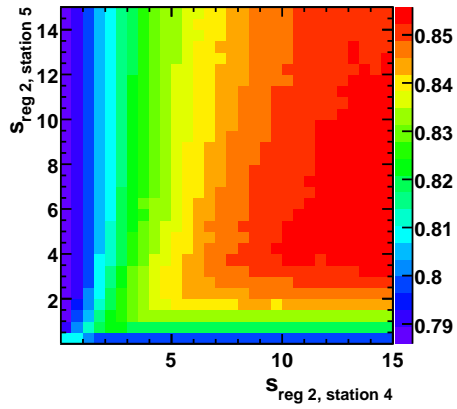
B.2 Configuration of the Velo-Muon matching algorithm

Figures B.1 and B.2 show how the matching efficiency depends on the weights scaling the sizes of muon stations' detector cells.

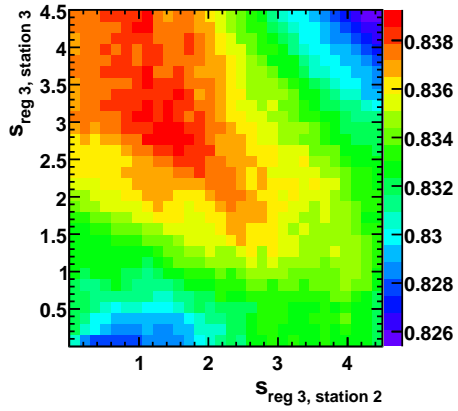
In chapter 6 the efficiency and purity of Velo-Muon matching in dependence on the maximum matching distance d is shown for region 0. The dependency for the remaining three parameters is shown in figure B.3. It is worth noticing that although the matching distance is given in millimetre it is not any distance in three dimensional space between the track segments.



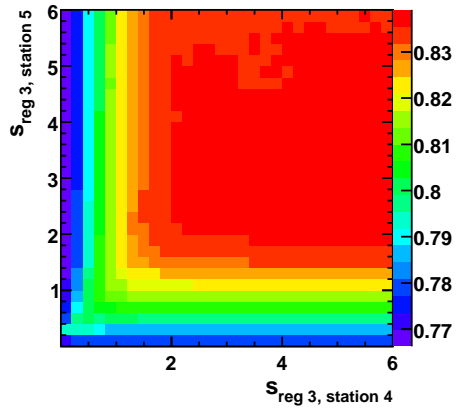
(a) Region 2 in stations M2 and M3.



(b) Region 2 in stations M4 and M5.

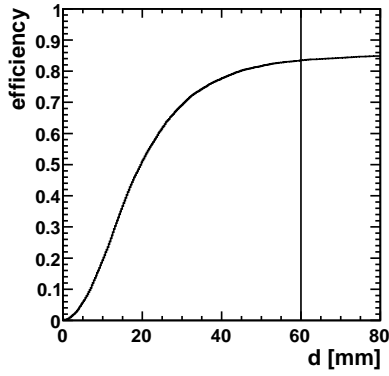


(c) Region 3 in stations M2 and M3.

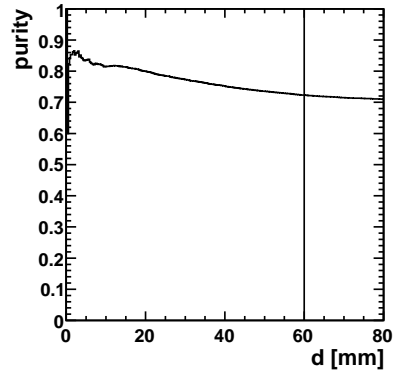


(d) Region 3 in stations M4 and M5.

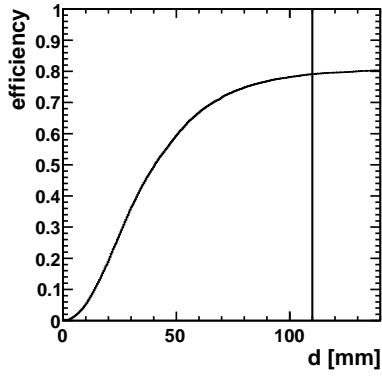
Figure B.2: Velo-Muon matching efficiency as a function of the scaling factors modifying the fit of the muon track segment.



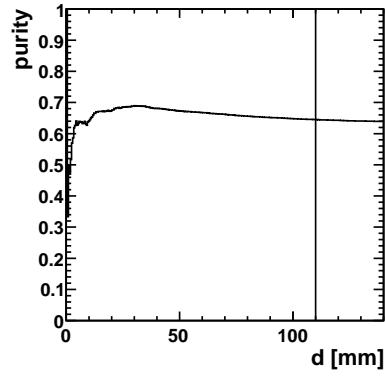
(a) Velo-Muon matching efficiency for muons in region 1.



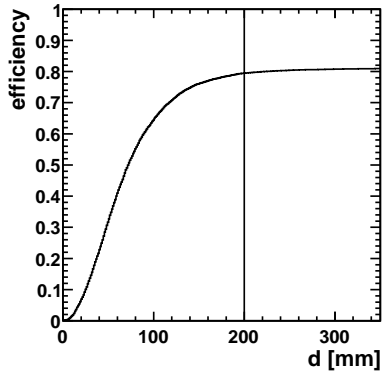
(b) Velo-Muon matching purity for muons in region 1.



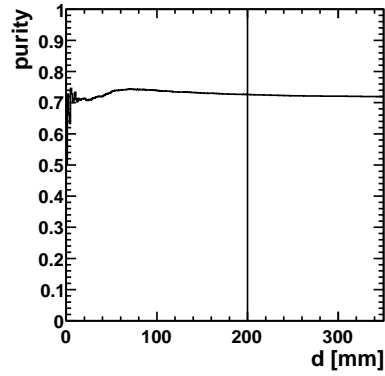
(c) Velo-Muon matching efficiency for muons in region 2.



(d) Velo-Muon matching purity for muons in region 2.



(e) Velo-Muon matching efficiency for muons in region 3.



(f) Velo-Muon matching purity for muons in region 3.

Figure B.3: Dependency of the Velo-Muon matching performance on the maximum matching distance. Different x axes are used in the different regions.

B.3 K_S Selection

To select the K_S decays among all reconstructed decays, a number of cuts is applied. Their effect is illustrated in figures B.5 and B.6 for simulated events. All ten figures have been created using simulated events.

In chapter 7 the effect of the direction angle cut on data is not shown. In figure B.4 the result of an automatised fit routine is shown which suggests to cut at much larger values. The fits at different $\cos(\text{DIRA})$ values have been checked and tuned by hand without improvement – the peaking background shape causes the estimated number of K_S decays for tight cuts to be larger than for the moderate cut at 0.99995.

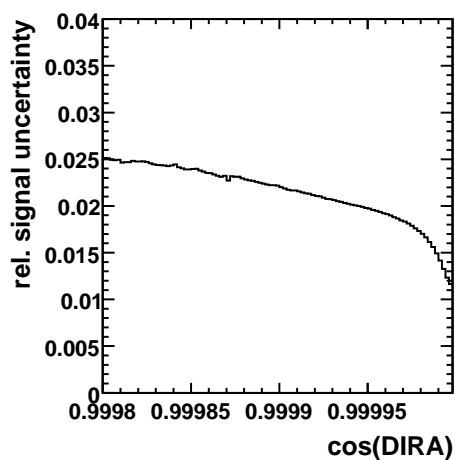
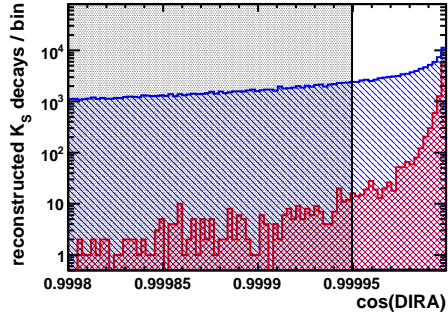
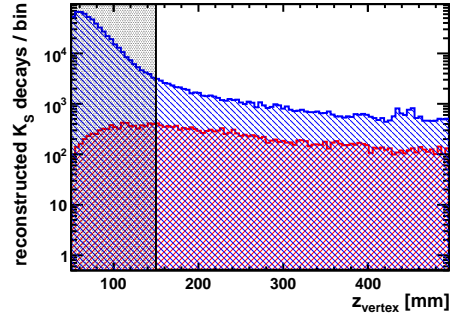


Figure B.4: Automatically generated dependency of the relative signal uncertainty on the direction angle cut.

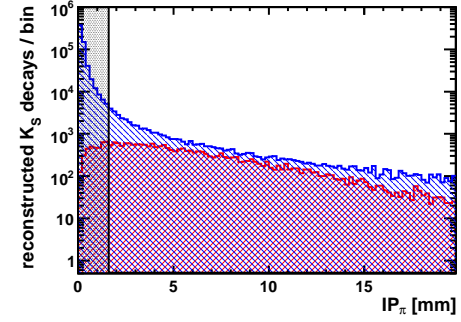
It is worth noticing, that the cuts are correlated to each other as can be seen from the cut on the DOCA – after all other cuts are applied, it hardly changes rejects any of the candidates whereas on the initial distribution a large number of background events is rejected.



(a) Distribution without other cuts.



(b) Distribution without other cuts.



(c) Distribution without other cuts.

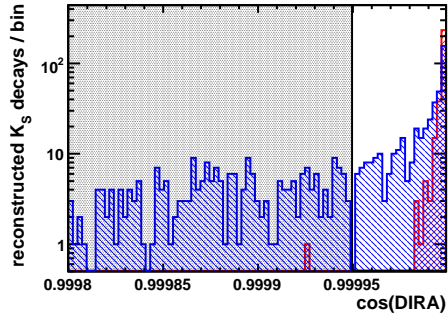
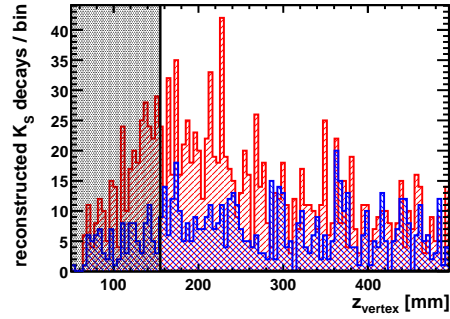
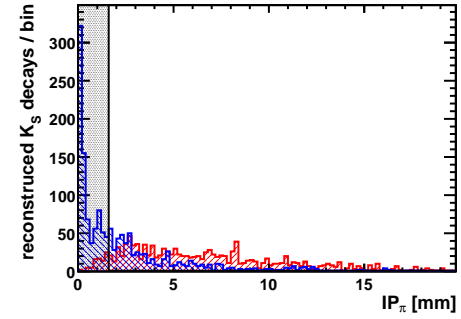
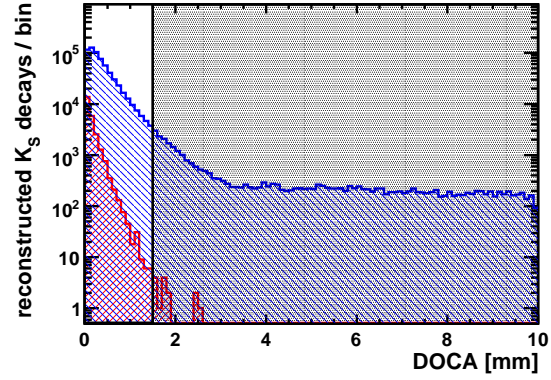
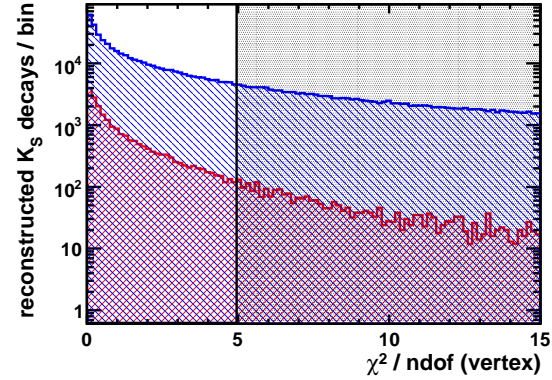
(d) $N - 1$ distribution.(e) $N - 1$ distribution.(f) $N - 1$ distribution.

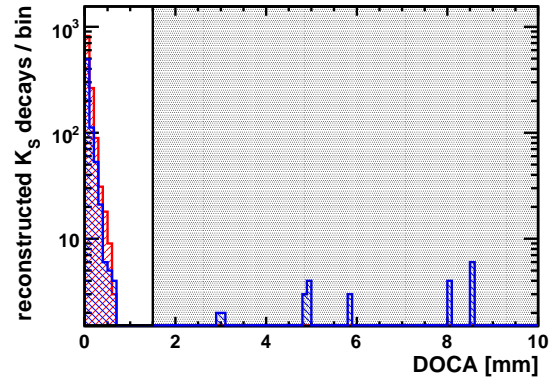
Figure B.5: Distribution of correct reconstructed K_S decays (red) and other reconstructed decays (blue) as a function of different cut parameters without other cuts applied (top row) and with all other cuts applied (bottom row).



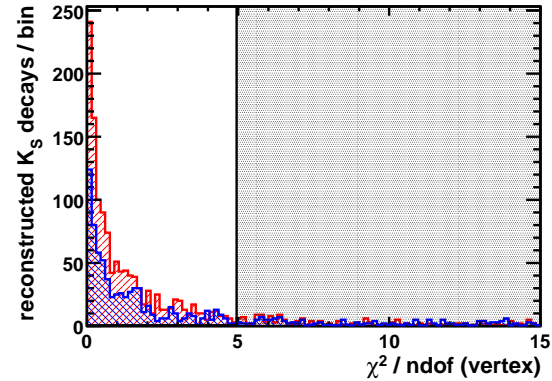
(a) Distribution without other cuts.



(b) Distribution without other cuts.



(c) $N - 1$ distribution.



(d) $N - 1$ distribution.

Figure B.6: Distribution of correct reconstructed K_S decays (red) and other reconstructed decays (blue) as a function of different cut parameters without other cuts applied (top row) and with all other cuts applied (bottom row).

Toy Simulation to Validate the Efficiency Estimation and the According Error Estimate

C.1 Description of the Toy Study

The present toy study shall validate the efficiency estimation with fits and the error estimate in equation 10.3 which are used in the tag and probe method. The invariant mass spectrum of a two pion system is simulated consisting of a signal part for the decay of K_S

$$p_s(x) = Y \cdot \left(\frac{1 - f_b}{\sigma\sqrt{2\pi}} \cdot e^{-\frac{1}{2} \frac{(x-M)^2}{\sigma^2}} + \frac{f_b}{w\sigma\sqrt{2\pi}} \cdot e^{-\frac{1}{2} \frac{(x-M)^2}{w^2\sigma^2}} \right)$$

and a background part

$$p_b(x) = \left(\frac{Y}{S} - Y \right) \cdot (a + bx + cx^2).$$

These probability distribution functions are the same which are fitted in chapter 7.

The parameters are listed in table C.1¹. Both, signal events and background events, are randomly assigned to belong to the spectrum of confirmed decays as well. The probabilities are ε (which is the efficiency to be determined) and β respectively. The number of confirmed signal events Υ will therefore be a random number with expectation value $\langle \Upsilon \rangle = \varepsilon \cdot Y$.

The fit routine which determines the number of all K_S daughters N and confirmed K_S daughters k is then applied to the generated spectra.

The estimated efficiency and the estimated error are abbreviated with $\hat{\varepsilon}$ and $\widehat{\Delta\varepsilon}$ respectively. The estimation pull $\frac{\hat{\varepsilon} - \varepsilon}{\widehat{\Delta\varepsilon}}$ is calculated for each toy experiment. Ideally the estimation pull is Gaussian distributed with a mean of 0 and a RMS of 1.

To illustrate that the chosen way to calculate the error is more appropriate than the other ways explained in chapter 10, the following error estimates are used in every toy experiment and the resulting pulls are compared.

$$\widehat{\Delta\varepsilon}_{\text{binomial}} = \sqrt{\frac{(k + 1/2)(N - k + 1/2)}{(N + 1)^2(N + 2)}} \quad (10.1)$$

$$\widehat{\Delta\varepsilon}_{\text{toy}} = \sqrt{\frac{1}{N^2}\sigma_k^2 + \frac{k^2}{N^4}\sigma_N^2 - 2\frac{k}{N^3}\sigma_N\sigma_k \text{Corr}(k, N)} \quad (10.2)$$

$$\widehat{\Delta\varepsilon}_{\text{decorr}} = \sqrt{(1 - 2\varepsilon) \left(\frac{\sigma_k}{N} \right)^2 + \varepsilon^2 \left(\frac{\sigma_N}{N} \right)^2} \quad (10.3)$$

¹The K_S mass is shifted with respect to the PDG value due to calibration effects

Table C.1: Parameters of the toy simulation. If a range is listed the value in use is given separately, otherwise the value from this table is taken.

parameter	description	typical value	obtained from
signal part			
Y	number of simulated K_S	0...500,000	arbitrary chosen to focus on errors arising from fit statistics or from binomial statistics
M	K_S mass	500 MeV	measured data
σ	width of the narrow Gaussian	6.28 MeV	measured data
w	width factor = width of the broader Gaussian in units of σ	2	measured data
f_b	broad fraction = fraction of simulated K_S in the broader Gaussian distribution	0.4	measured data
background part			
S	signal fraction (within 400-600 MeV)	0...1	measured data or chosen to switch off the background contribution
a, b, c	coefficients of a second order polynomial background	-0.00168 MeV ⁻¹ 8.75×10^{-5} MeV ⁻² -1.23×10^{-7} MeV ⁻³	measured data
confirmation probabilities			
ε	efficiency	0...0.99	arbitrary chosen
β	probability to confirm a background event	0.4...0.9	arbitrary chosen

C.2 Results of the Toy Study

From tables C.2(a) to C.2(c) it can be seen that the estimation pull for the error estimate using the decorrelated ansatz is in average closest to 0. If the uncertainty from the fit is not considered, i.e. $\widehat{\Delta\varepsilon}_{\text{binomial}}$ is used, the error is highly underestimated as can be seen from table C.2(b).

In the case of $\widehat{\Delta\varepsilon}_{\text{toy}}$ the factor $\text{Corr}(k, N)$ has to be determined in an individual toy study and fixed to that result. This procedure is costly on the one hand and provides estimates which are less accurate than the decorrelated approach which can be seen comparing table C.2(a) and C.2(c).

From table C.2(a) several statements about $\widehat{\Delta\varepsilon}_{\text{decorr}}$ can be made. The background level, which changes from line 1 to 2, has an influence on the bias of the estimate. The efficiency estimate is however more reliable in the case of a smaller signal to background ratio. The setting in line 3 was chosen to test the stability of the routine in the case of the absence of the signal, which the method passed. The settings in 4 and 5 differ in the background level for full reconstructed decays. The decorrelated approach is the only method which maintains the performance for that change.

The signal fraction in lines 6 and 7 is the smallest occurring among the measurements

Table C.2: Mean and RMS of the pull distribution for different error estimates and different simulation parameters. Each time 1400 toy experiments were performed. Failures of a method are indicated with “—”.

(a) $\widehat{\Delta\varepsilon}_{\text{decorr}}$ from equation 10.3

	ε	β	S	Y	mean of estimation pull	RMS of estimation pull
1	0.85	0.6	0.2	30,000	0.092 ± 0.033	1.143 ± 0.024
2	0.85	0.6	1	30,000	-0.253 ± 0.053	1.196 ± 0.035
3	0.85	0.6	0.001	1	0.821 ± 0.0065	1.024 ± 0.046
4	0.85	0.4	0.2	30,000	-0.040 ± 0.040	1.283 ± 0.028
5	0.85	0.9	0.2	30,000	-0.190 ± 0.046	1.194 ± 0.033
6	0.85	0.6	0.087	10,000	-0.226 ± 0.058	1.473 ± 0.041
7	0.85	0.6	0.087	500,000	-0.088 ± 0.034	0.920 ± 0.024

(b) $\widehat{\Delta\varepsilon}_{\text{binomial}}$ from equation 10.1

	ε	β	S	Y	mean of estimation pull	RMS of estimation pull
1	0.85	0.6	0.2	30,000	-0.691 ± 0.062	2.324 ± 0.044
2	0.85	0.6	1	30,000	—	—
3	0.85	0.6	0.001	1	-2.474 ± 0.161	1.443 ± 0.114
4	0.85	0.4	0.2	30,000	0.324 ± 0.071	2.655 ± 0.050
5	0.85	0.9	0.2	30,000	-1.463 ± 0.045	1.684 ± 0.032
6	0.85	0.6	0.087	10,000	-3.114 ± 0.102	3.738 ± 0.072
7	0.85	0.6	0.087	500,000	< 11	> 3

(c) $\widehat{\Delta\varepsilon}_{\text{toy}}$ from equation 10.2

	ε	β	S	Y	mean of estimation pull	RMS of estimation pull
1	0.85	0.6	0.2	30,000	-0.289 ± 0.025	0.930 ± 0.018
2	0.85	0.6	1	30,000	—	—
3	0.85	0.6	0.001	1	1.144 ± 0.019	0.563 ± 0.014
4	0.85	0.4	0.2	30,000	0.111 ± 0.029	1.082 ± 0.020
5	0.85	0.9	0.2	30,000	-0.556 ± 0.017	0.644 ± 0.012
6	0.85	0.6	0.087	10,000	-1.013 ± 0.032	1.193 ± 0.023
7	0.85	0.6	0.087	500,000	-3.991 ± 0.054	2.004 ± 0.038

C. TOY SIMULATION TO VALIDATE THE EFFICIENCY ESTIMATION
AND THE ACCORDING ERROR ESTIMATE

in chapter 7 and chosen to test if the method provides reliable results in that region of the phase space. The RMS of the pull in line 6 is 50 % too large while it is acceptable for increased statistics in line 7.

Data Sets

Throughout this thesis measurements made on several data sets are shown. For reproducibility their names in the LHCb book-keeping are given here.

The efficiency measurement at $\sqrt{s} = 900$ GeV has been performed with Brunel v36r2. The efficiency measurements at $\sqrt{s} = 7$ TeV have been performed with DaVinci v25r8, to measure the efficiency of the individual algorithms they have been rerun in DaVinci. For the plots and findings in chapters 5 and 6 Brunel v37r7 has been used.

D.1 Simulated Data

At centre of mass energies of 900 GeV the data sample

2009-Beam450GeV-VeloClosed15mm-MagDown-Fix1-GeoDec2009a
2009-Sim06Reco04-withTruth

was used. The modifications mentioned in chapter 7 were also applied to this data set.

At centre of mass energies of 7 TeV different data samples were used. For the efficiency measurement in chapter 7 the following has been used.

2010-Beam350GeV-VeloClosed-MagDown-Nu1
2010-Sim03Reco03-withTruth
minbias

For events containing the decay $J/\psi \rightarrow \mu\mu$:

2010-Beam350GeV-VeloClosed-MagDown-Nu1
2010-Sim03Reco03-withTruth
incl_Jpsi,mm=DecProdCut

For events containing the decay $B_s^0 \rightarrow J/\psi\phi \rightarrow \mu\mu KK$:

MC09-Beam5TeV-VeloClosed-MagDown-Nu1
MC09-Sim03Reco02-withTruth
Bs_Jpsiphi,mm=LargeCPV,DecProdCut

D. DATA SETS

At centre of mass energies of 10 TeV the data sets for minimum bias, i.e. K_S studies, were:

```
MC09-Beam5TeV-VeloClosed-MagDown-Nu1
MC09-Sim03Reco02-withTruth
minbias
```

For events containing the decay $J/\psi \rightarrow \mu\mu$:

```
MC09-Beam5TeV-VeloClosed-MagDown-Nu1
MC09-Sim03Reco02-withTruth
incl.Jpsi,mm=DecProdCut
```

For events containing the decay $B_s^0 \rightarrow J/\psi\phi \rightarrow \mu\mu KK$:

```
MC09-Beam5TeV-VeloClosed-MagDown-Nu1
MC09-Sim03Reco02-withTruth
Bs_Jpsiphi,mm=NoCPV,DecProdCut
```

D.2 Data

At centre of mass energies of 900 GeV the following runs were reprocessed with Brunel v36r2:

run number	# physics events	TCK
63686	24391	0x1209
63687	15642	0x1209
63688	2169	0x1209
63690	20855	0x1209
63691	2074	0x1209
63713	14295	0x1209
63801	94112	0x1309
63807	75285	0x1309
63809	23465	0x1309
63813	71429	0x1309
63814	4629	0x1309
63815	11668	0x1309
63949	64179	0x1309

At centre of mass energies of 7 TeV for T station efficiency measurements, events were taken from:

Collisions10-Beam350GeV-VeloClosed-MagDown
Reco05-Stripping09-Merged
MINBIAS

Collisions10-Beam350GeV-VeloClosed-MagUp
Reco05-Stripping09-Merged
MINBIAS

For the study of the muon track segment reconstruction, J/ψ decays from

Collisions10-Beam350GeV-VeloClosed-MagDown
Reco05-Stripping09-Merged
DIMUON

were analysed.

The sample for the development of the J/ψ stripping line has been provided by the stripping group of LHCb and was a subset of the data from the reprocessing “Reco05-Stripping08”.

Bibliography

- [A⁺10a] V.M. Abazov et al. Search for the rare decay $B_s^0 \rightarrow \mu^+ \mu^-$. 2010, arXiv:hep-ex/1006.3469v2.
- [A⁺10b] N. Agafonova et al. Observation of a first ν_τ candidate in the OPERA experiment in the CNGS beam. 2010, arXiv:1006.1623v1.
- [Ait03] I.J.R. Aitchison. *From relativistic quantum mechanics to QED*. Gauge theories in particle physics. Institute of Physics Publishing, Bristol, 3. ed. edition, 2003.
- [Alb10] J. Albrecht. Multiple Interactions and $B_s^0 \rightarrow \mu\mu$. At *41st Analysis and Software Week*, 14 September 2010, <http://indico.cern.ch/conferenceDisplay.py?confId=73580>.
- [BBM03] T. Bellunato, R. Bonifacio, and C. Matteuzzi. *Development of Ring Imaging Cherenkov Detectors for LHCb*. PhD thesis, Milan, Università degli Studi di Milano, Milan, 2003, oai:cds.cern.ch:1181096. Presented on 17 Jan 2003.
- [C⁺05] J. Charles et al. CP violation and the CKM matrix: Assessing the impact of the asymmetric B factories. *Eur. Phys. J.*, C41:1–131, 2005, hep-ph/0406184. updated results and plots available at: <http://ckmfitter.in2p3.fr>.
- [Cal07] O. Callot. News from Pat packages. At *Tracking and Alignment Workshop*, 22 February 2007, <http://indico.cern.ch/materialDisplay.py?contribId=13&sessionId=1&materialId=slides&confId=12233>.
- [Cas10] D. Casadei. How to measure efficiency. 2010, arXiv:0908.0130v4.
- [CER10] CERN. public web page, June 2010, <http://public.web.cern.ch/public/en/Research/AccelComplex-en.html>.
- [CHM07] O. Callot and S. Hansmann-Menzemer. The Forward Tracking: Algorithm and Performance Studies. LHCb Note LHCb-2007-015. CERN-LHCb-2007-015, Geneva, May 2007.
- [CKW07] O. Callot, M. Kucharczyk, and M. Witek. VELO-TT track reconstruction. LHCb Note LHCb-2007-010. CERN-LHCb-2007-010, Geneva, Apr 2007.
- [Cli06] J.M. Cline. Baryogenesis. 2006, arXiv:hep-ph/0609145v3.

- [Col08] The LHCb Collaboration. The LHCb Detector at the LHC. *Journal of Instrumentation*, 3(08):S08005, 2008, doi:10.1088/1748-0221/3/08/S08005.
- [Col09] The LHCb Collaboration. Roadmap for selected key measurements of LHCb. 2009, arXiv:0912.4179v2.
- [Col10a] The LHCb Collaboration. public web page, June 2010, <http://lhcb-public.web.cern.ch/lhcb-public/en/Detector/Detector-en.html>.
- [Col10b] The LHCb Collaboration. public web page, August 2010, <http://lhcb-public.web.cern.ch/lhcb-public/>.
- [CS08] O. Callot and M. Schiller. PatSeeding: A Standalone Track Reconstruction Algorithm. LHCb Note LHCb-2008-042. CERN-LHCb-2008-042, Geneva, Aug 2008.
- [dC10a] M. de Cian. Tracking efficiency with Z. At *Physics Performance Meeting*, 1 November 2010, <http://indico.cern.ch/contributionDisplay.py?contribId=1&confId=99594>.
- [dC10b] M. de Cian. Revision of Adding TT Hits to Long Tracks. LHCb Note LHCb-INT-2010-020. CERN-LHCb-INT-2010-020, Geneva, Apr 2010.
- [dC10c] M. de Cian. Tracking efficiencies with MuonTT tracks? At *Tracking and Alignment Meeting*, 29 July 2010.
- [dC10d] M. de Cian. Tracking Efficiency with J/ψ . At *Tracking and Alignment Workshop*, 4 June 2010, <http://indico.cern.ch/materialDisplay.py?contribId=13&resId=0&materialId=slides&confId=93325>.
- [Frü87] R. Frühwirth. Application of Kalman filtering to track and vertex fitting. *Nuclear Instruments and Methods in Physics Research Section A: Accelerators, Spectrometers, Detectors and Associated Equipment*, 262(2-3):444–450, 1987.
- [Frü00] R. Frühwirth. *Data analysis techniques for high-energy physics*. Number 11 in Cambridge monographs on particle physics, nuclear physics, and cosmology ; 11 ; Cambridge monographs on particle physics, nuclear physics, and cosmology. Cambridge University Press, Cambridge [u.a.], 2. ed. edition, 2000. Includes bibliographical references and index.
- [HM08] S. Hansmann-Menzemer. Studies of PatForward Efficiency. At *Tracking and Alignment Workshop*, 28 February 2008, <http://indico.cern.ch/conferenceDisplay.py?confId=26985>.
- [HM10] S. Hansmann-Menzemer. Tuning of PatForward. At *Multiple Interaction Workshop*, 3 August 2010.
- [HMHK⁺10] S. Hansmann-Menzemer, K. Holubyev, G. Krocker, C. Linn, M. Schiller, P. Seyfert, S. Stahl, and S. Wandernoth. Measurement of the yield K_S reconstructed with downstream tracks in 2009 data. LHCb Note LHCb-INT-2010-013. CERN-LHCb-INT-2010-013, Geneva, June 2010.

-
- [HVdB03] R.H. Hierck and J.F.J. Van den Brand. *Optimisation of the LHCb detector*. PhD thesis, Amsterdam Univ., Geneva, 2003. Presented on 21 Oct 2003.
- [Jon10] C. Jones. Particle ID. At *LHCb Week, Validation of Trigger and Physics Performance*, 30 June 2010, <http://indico.cern.ch/materialDisplay.py?contribId=2&materialId=slides&confId=82181>.
- [KdC10] G. Krocker and M. de Cian. stripping lines for the track efficiency measurements. At *Trigger & Stripping Meeting*, 20 September 2010, <http://indico.cern.ch/materialDisplay.py?contribId=1&materialId=slides&confId=82224>.
- [KM73] M. Kobayashi and T. Maskawa. CP Violation in the Renormalizable Theory of Weak Interaction. *Prog. Theor. Phys.*, 49:652–657, 1973.
- [Mei10] M. Meißner. Ghost rate estimation. At *Tracking and Alignment Meeting*, 14 October 2010, <http://indico.cern.ch/contributionDisplay.py?contribId=1&confId=110440>.
- [Nak10] K. Nakamura. Review of particle physics. *J. Phys.*, G37:075021, 2010.
- [Nek06] NekojaNekoja. HoughSpace2D. Wikimedia Commons, 2006, <http://commons.wikimedia.org/w/index.php?title=File:HoughSpace2D.PNG&oldid=27365664>. published under GNU Free Documentation License.
- [Pat04] M. Paterno. Calculating efficiencies and their uncertainties. 2004.
- [Rea08] K. Read. The ALICE Experiment. October 2008. SESAPS 2008, Raleigh, USA.
- [RH07] E. Rodrigues and J.A. Hernando. Tracking Event Model. LHCb Note LHCb-2007-007, September 2007.
- [Sch] M. Schiller. private communication.
- [Sch10] M. Schiller. Update on PatSeeding. At *Tracking and Alignment Meeting*, 14 October 2010, <http://indico.cern.ch/contributionDisplay.py?contribId=0&confId=110440>.
- [Sey10a] P. Seyfert. Measurement of Tracking Efficiencies Using Velo-Calo K_S Legs. At *Tracking and Alignment Workshop*, 4 June 2010, <http://indico.cern.ch/materialDisplay.py?contribId=10&resId=0&materialId=slides&confId=93325>.
- [Sey10b] P. Seyfert. Update on Measured Tracking Efficiencies Using Velo-Calo K_S legs. At *Tracking and Alignment Meeting*, 9 June 2010, <http://indico.cern.ch/materialDisplay.py?contribId=2&resId=1&materialId=slides&confId=100498>.
- [Sta08] J. Stachel. *Kern- und Teilchenphysik*. Lecture Notes. 2008.
- [Sta09] J. Stachel. *Physics of Particle Detectors*. Lecture Notes. 2009.

- [Sta10] S. Stahl. Reconstruction of displaced tracks and measurement of K_S production rate in proton-proton collisions at $\sqrt{s} = 900 \text{ GeV}$ at the LHCb experiment. Diploma thesis, Heidelberg University, 2010.
- [Ste08] J. Stefaniak. Zeitkalibrierung des äußeren Spurkammersystems des LHCb-Detektors und Messung der Effizienz der Spurrekonstruktion. Diploma thesis, Heidelberg University, 2008.
- [Sto10] B. Storaci. Measuring Tracking Efficiencies in Data. At *Tracking and Alignment Workshop*, 4 June 2010, <http://indico.cern.ch/materialDisplay.py?contribId=9&resId=0&materialId=slides&confId=93325>.
- [Urqu10] P. Urquijo. Tracking Efficiency Systematics with $D^0 \rightarrow K\pi\pi\pi/D^0 \rightarrow K\pi$. At *Tracking and Alignment Workshop*, 4 June 2010, <http://indico.cern.ch/materialDisplay.py?contribId=16&resId=0&materialId=slides&confId=93325>.
- [Wan10a] S. Wandernoth. Tracking Efficiencies. At *Tracking and Alignment Workshop*, 4 June 2010, <http://indico.cern.ch/materialDisplay.py?contribId=12&resId=0&materialId=slides&confId=93325>.
- [Wan10b] S. Wandernoth. Tracking efficiencies in VeLo. At *Tracking and Alignment Meeting*, 9 July 2010, <http://indico.cern.ch/conferenceDisplay.py?confId=100498>.
- [Wik10] Wikipedia. Standard Model of Elementary Particles, 2010, [http://en.wikipedia.org/w/index.php?title=Standard Model&oldid=377115928](http://en.wikipedia.org/w/index.php?title=Standard%20Model&oldid=377115928). [Online; accessed 9-August-2010].
- [Zwa06] N. Zwahlen. HLT Hadronic L0 Confirmation. LHCb Note LHCb-2006-040. CERN-LHCb-2006-040, Geneva, July 2006.

Index

- calorimeter cluster, 17
- clone, 22
- clone killer, 22
 - muon track segment, 44
- confirmation, 27, 40
 - background, 76
 - Velo-Calo probes, 40
- CP* violation, 4

- DIRA, *see* direction angle
- direction angle, 56
- downstream track, 24

- efficiency
 - muon track segments, 82
 - tracking, 22

- fit
 - χ^2 , 99
 - Kalman filter, 22
- forward tracking, 24

- hit efficiency, 22
- HLT, 18

- identification, 16
 - muon identification, 17
- IT, 14

- Kalman filter, 22

- L0, 18
- LHCb
 - layout, 11
 - physics program, 10
 - subdetectors, 12–15
- longtrack, 24

- muon identification, 17

- OT, 15

- probe, 27
 - confirmed, 27
 - Velo-Calo probe, 31
 - Velo-Muon probe, 43
- pseudo rapidity, 12

- stereo angle, 14

- TIS, 19
- TOS, 19
- track, 11
 - downstream track, 24
 - longtrack, 24
 - muon track segment, 43
 - T track, 23
 - upstream track, 25
 - Velo track, 23
- track finding, 21
- track finding efficiency, 22
- track fitting, 21
- track matching, 24
- trigger efficiency, 80
- TT, 13
- t_x, t_y , 12

- upstream track, 25

- VELO, 12
- Velo track, 23
- Velo-Muon reconstructible, 52

Erklärung

Ich versichere, dass ich diese Arbeit selbständig verfaßt und keine anderen als die angegebenen Quellen und Hilfsmittel benutzt habe.

Heidelberg, den 12. November 2011
